





**Petrogenesis of the mafic part of the Étoile Suite, Quebec, and its vanadium mineralization**

**Pétrogenèse de la partie mafique de la Suite d'Étoile, Québec, et sa minéralisation en vanadium**

**par Randolph Paul Maier**

**Mémoire présenté à l'Université du Québec à Chicoutimi en vue de l'obtention du grade de**

**Maître ès sciences appliquées en Sciences de la Terre**

Québec, Canada

© Randolph Paul Maier, 2022

## Abstract

The Étoile Suite comprises predominantly mafic, as well as minor felsic, intrusives emplaced over an area of ~100 square kilometres, some 130 km to the north west of Quebec City, Canada. The mafic part of the intrusion hosts V-rich mineralization (the Lac Fabien prospect) associated with a 1000 m-thick oxide-rich horizon. In this study, the petrology and geochemistry of the mafic part of the suite is evaluated with the aim of better understanding its petrogenesis and its V mineralization.

The mafic part of the suite has a surface exposure of roughly 33 square kilometres and a stratigraphic thickness of ~4.5 kilometres. It consists predominantly of variably layered medium-grained oxide-bearing (olivine) gabbro cumulates, and minor troctolites. The rock-forming minerals (plagioclase, olivine, clinopyroxene, magnetite and ilmenite) display cumulus or intercumulus habit in the stratigraphic succession. The cumulus mineralogy of the Fe-Ti oxides (magnetite and ilmenite) allows the intrusion to be subdivided into three stratigraphic zones: two zones with intercumulus Fe-Ti oxides (Zone A and Zone C) and one zone with cumulus Fe-Ti oxides (Zone B). The compositions of the main rock-forming minerals are  $F_{\text{Olivine}} = 31-68$ ,  $An_{\text{Plagioclase}} = 35-57$  and  $Mg\#_{\text{clinopyroxene}} = 62-77$ . The layering dips at ~55 degrees towards the north west and the minerals show progressively more evolved compositions in the same direction, suggesting that the intrusion is not overturned.

The rock-forming minerals also show considerable variation in abundance with stratigraphic height, with magnetite and ilmenite being especially abundant in the lower portion of Zone B (12-49 %), which represents the Fe-Ti(V)-mineralized part of the intrusion. The Fe-Ti(V) mineralization is characterised by disseminated and semi-massive titanomagnetite (with up to 1.85 wt. %  $V_2O_5$  in magnetite) that most likely formed as a result of late cotectic crystallisation of oxides (i.e., from a relatively evolved basaltic magma in equilibrium with andesine-type plagioclase). The magnetite to ilmenite ratio in the mineralized horizon is ~2:1. Elsewhere it is on the order of 1:1. Oxygen fugacity ( $fO_2$ ) and temperature conditions marking the end of oxy-exsolution in magnetite (calculated using QUILF) suggest that the magma crystallised under  $fO_2$  conditions corresponding roughly to FMQ +1 (1.0 log units above the FMQ buffer). This value is close to the  $fO_2$  range in which the most V-rich magnetites typically crystallise (i.e., FMQ +0.25 to FMQ -0.25).

Compositional variation trends of anorthite in plagioclase, forsterite in olivine, and Mg# in clinopyroxene with stratigraphic height suggest that the magma underwent progressive fractional crystallisation, interrupted by three compositional reversals that are interpreted to reflect late-stage magma replenishments. The bulk of the intrusion shows little evidence for crustal contamination, as suggested by the absence of orthopyroxene. However, at the top of the body there is an orthopyroxene-bearing noritic layer interpreted to represent either (1) a late-stage magma replenishment that underwent more contamination; or (2) an early intrusive phase that underwent more contamination.

The age of the Étoile Suite has been determined at  $1148.3 \pm 9.6$  Ma, broadly coeval with the Lac Saint-Jean Anorthosite Suite and other troctolitic-gabbroic layered intrusions in the Grenville Province. This indicates that anorthosite massifs and layered intrusions can be consanguineous. Layered intrusions in anorthosite-bearing terranes can either be troctolitic or noritic. Whether intrusions are noritic or troctolitic is dependent on contamination, as noritic intrusions record higher degrees of contamination than troctolitic intrusions. Crust that has experienced prior melt extraction – and can therefore no longer readily contaminate throughgoing magmas – is therefore considered to be a key contributor to the formation of troctolitic intrusions. Lack of contamination in troctolitic intrusions means they are not as susceptible to contamination-induced increases in oxygen fugacity, and, as a result, will crystallise at close to FMQ. In contrast, noritic intrusions, having undergone more contamination, will crystallise at higher  $fO_2$  (assuming the contaminant is oxidising). Experimental studies have shown that, above FMQ, the appearance temperature of magnetite increases, and the partition coefficient of V into magnetite decreases. This may account for differences in (a) the timing of magnetite crystallisation; and (b) the V content of magnetite in troctolitic and noritic intrusions.

## Résumé

La Suite d'Étoile comprend principalement des intrusions mafiques, ainsi que des intrusions felsiques mineures, mises en place sur une superficie d'environ 100 kilomètres carrés, et est située à environ 130 km au nord-ouest de la ville de Québec, Canada. La partie mafique de l'intrusion est l'hôte d'une minéralisation riche en V (l'indice Lac Fabien) associée à un horizon riche en oxydes de 1000 m d'épaisseur. Dans cette étude, la pétrologie et la géochimie de la partie mafique de la suite sont évaluées afin de mieux comprendre sa pétrogénèse et sa minéralisation en V.

La partie mafique de la suite est exposée en surface sur environ 33 kilomètres carrés et a une épaisseur stratigraphique d'environ 4,5 kilomètres. L'intrusion est variablement litée et se compose principalement de cumulats de gabbro à oxydes+olivine à grain moyen et de quelques troctolites. Le plagioclase, olivine, clinopyroxène, magnétite et ilménite présentent un habitus cumulus ou intercumulus dans la succession stratigraphique. Les proportions variables des oxydes de Fe-Ti (magnétite et ilménite) permettent de subdiviser l'intrusion en trois zones stratigraphiques : deux zones à oxydes Fe-Ti intercumulus (Zone A et Zone C) et une zone à oxydes Fe-Ti cumulus (Zone B). Les compositions des principaux minéraux sont  $Fo_{Olivine} = 31-68$ ,  $An_{Plagioclase} = 35-57$  et  $Mg\#_{clinopyroxene} = 62-77$ . La stratification plonge à ~55 degrés vers le nord-ouest et les minéraux montrent des compositions progressivement plus évoluées dans la même direction, suggérant que l'intrusion n'est pas renversée.

Les minéraux principaux présentent également une variation considérable de l'abondance avec la hauteur stratigraphique, la magnétite et l'ilménite étant particulièrement abondantes dans la partie inférieure de la Zone B (12-49 %), qui représente la partie minéralisée en Fe-Ti-(V) de l'intrusion. La minéralisation Fe-Ti-(V) est caractérisée par une titanomagnétite disséminée et semi-massive (jusqu'à 1,85 % en poids de  $V_2O_5$  dans la magnétite) qui s'est très probablement formée par cristallisation cotectique tardive des oxydes ; c'est-à-dire à partir d'un magma basaltique en équilibre avec le plagioclase de type andésine. Le rapport magnétite/ilménite dans l'horizon minéralisé est d'environ 2:1. Ailleurs, il est de l'ordre de 1:1. La fugacité de l'oxygène ( $fO_2$ ) et les conditions de température marquant la fin de l'oxy-exsolution dans la magnétite (calculées à l'aide de QUILF) suggèrent que le magma a cristallisé dans des conditions de  $fO_2$  correspondant approximativement à FMQ +1 (1,0 unités log au-dessus du tampon FMQ). Cette valeur est proche de la plage de  $fO_2$  dans laquelle cristallisent généralement les magnétites les plus riches en V (c'est-à-dire FMQ +0,25 à FMQ -0,25).

Les tendances de variation avec le niveau stratigraphique de la composition de l'anorthite dans le plagioclase, de la forstérite dans l'olivine et du Mg# dans le clinopyroxène suggèrent que le magma a subi une cristallisation fractionnée progressive, interrompue par trois inversions de composition qui sont interprétées comme reflétant des ajouts de magma primitif. La majeure partie de l'intrusion montre peu d'évidence de contamination crustale, comme le suggère l'absence d'orthopyroxène. Cependant, au sommet du corps, il y a une couche noritique porteuse d'orthopyroxène interprétée comme représentant soit (1) un ajout de magma primitif qui aurait subi plus de contamination ; ou (2) une phase intrusive précoce ayant subi plus de contamination.

L'âge de la Suite Étoile a été déterminé à  $1148,3 \pm 9,6$  Ma, largement contemporain de la Suite d'Anorthosite du Lac Saint-Jean et d'autres intrusions troctolitiques-gabbroïques stratifiées dans la Province de Grenville. Cela indique que les massifs d'anorthosite et les intrusions stratifiées peuvent être consanguins. Les intrusions stratifiées dans les terranes porteurs d'anorthosite peuvent être soit troctolitiques ou noritiques ; dépendant du niveau de contamination, puisque les intrusions noritiques enregistrent des degrés de contamination plus élevés que les intrusions troctolitiques. Une croûte ayant subi une extraction de liquide généré par la fusion partielle au préalable ne pourrait pas contaminer les magmas intrusifs et ces magmas peu contaminés formeraient les intrusions troctolitiques. L'absence de contamination dans les intrusions troctolitiques signifie qu'elles ne sont pas aussi sensibles aux augmentations de la fugacité de l'oxygène induites par la contamination et, par conséquent, cristalliseront à proximité de FMQ. En revanche, les intrusions noritiques, ayant subi plus de contamination, cristalliseront à une  $fO_2$  plus élevée (en presumant que le contaminant est

oxydé). Des études expérimentales ont montré qu'au dessus de FMQ, la température d'apparition de la magnétite augmente, et le coefficient de partage de V dans la magnétite diminue. Cela peut expliquer les différences dans (a) le point d'apparition de la magnétite lors du fractionnement ; et (b) la teneur en V de la magnétite dans les intrusions troctolitiques et noritiques.

## Table of Contents

Abstract .....	ii
Résumé .....	iii
Table of Contents .....	v
List of Tables .....	vii
List of Figures .....	viii
List of Abbreviations .....	x
Acknowledgements .....	xi
Chapter 1 .....	1
Introduction .....	1
Chapter 2 .....	4
Geological setting of the Étoile Suite .....	4
2.1 Regional geology .....	4
2.2 Geology of the Étoile Suite and Lac Fabien mineralized zone .....	9
Chapter 3 .....	12
Sampling and methodology .....	12
3.1 Sampling .....	12
3.2 Determination of the stratigraphic position of the analysed samples .....	12
3.3 Point counting .....	15
3.4 Element maps .....	16
3.5 Whole-rock analyses .....	16
3.6 Electron microprobe analyses .....	17
3.6.1 Silicates .....	17
3.6.2 Fe-Ti oxides .....	17
3.6.3 Apatite .....	18
3.7 Laser ablation inductively coupled plasma mass spectrometry (LA-ICP-MS) .....	18
3.7.1 Data quality for silicate analyses .....	20
3.7.2 Data quality for Fe-Ti oxide analyses .....	20
3.7.3 Data quality for apatite analyses .....	20
3.8 Oxygeothermometry .....	21
Chapter 4 .....	23
Results .....	23
4.1 General petrography .....	23
4.1.1 Stratigraphic variation in modal mineralogy .....	26
4.2 Petrography of the silicate minerals .....	29
4.2.1 Description of the main rock-forming minerals .....	29
4.2.2 Description of the Fe-Ti oxides .....	35
4.2.3 Description of the accessory minerals .....	40
4.3 Element maps of selected samples .....	42
4.3.1 Oxide-rich wehrlite .....	43
4.3.2 Oxide-bearing gabbro .....	45
4.4 Whole-rock concentrations of the major elements .....	48
4.5 Whole-rock concentrations of trace elements .....	52
4.6 Mineral compositions .....	59
4.6.1 Plagioclase .....	59
4.6.2 Olivine .....	61
4.6.3 Clinopyroxene .....	64
4.6.4 Orthopyroxene .....	68
4.6.5 Magnetite .....	68
4.6.6 Ilmenite .....	72

Chapter 5.....	74
Discussion.....	74
5.1 Crystallisation and emplacement history.....	74
5.1.1 Fractional crystallisation history.....	74
5.1.2 Contamination.....	75
5.1.3 Emplacement.....	76
5.2 Origin of the Fe-Ti-(V) oxide mineralization.....	77
5.2.1 Triggers of oxide saturation.....	78
5.3 Oxygeothermometry.....	80
5.4 Effect of oxygen fugacity on the V prospectivity of layered intrusions and anorthosite massifs.....	83
5.5 Origin of the sulphides.....	85
5.6 Association with AMCG magmatism.....	86
5.6.1 Introduction.....	86
5.6.2 Comparison to the Lac Saint-Jean Anorthositic Suite.....	88
5.6.3 Comparison to the Kiglapait Intrusion.....	89
5.6.4 Comparison to the Voisey's Bay Intrusion.....	92
5.7 Model for the formation of troctolitic intrusions in anorthosite-bearing terranes.....	95
Chapter 6.....	98
Summary and conclusions.....	98
Chapter 7.....	100
Recommendations for further work.....	100
7.1 Characterisation of the country rocks in order to constrain the nature of potential contamination.....	100
7.2 Determination of the PGE contents of the cumulates.....	100
List of References.....	102
Appendices.....	116

## List of Tables

Table 3.1: Analytical details for LA-ICP-MS analyses.....	18
Table 5.1: Temperature and $fO_2$ of selected samples calculated using QUILF by Andersen et al. (1993).....	82

## List of Figures

Figure 1.1: Location of the Étoile Suite within eastern Canada .....	3
Figure 2.1: Geological subdivisions of the Grenville Province .....	5
Figure 2.2: Simplified geological map of the Portneuf-Mauricie domain and adjacent geological units .....	6
Figure 2.3: Geological map of the 'south-central' Grenville Province displaying the plutons associated with the four episodes of AMCG magmatism .....	8
Figure 2.4: Local geology of the area around the Étoile Suite .....	10
Figure 2.5: Map showing vertical gradient of residual magnetic field for the mafic part of the Étoile Suite .....	11
Figure 3.1: Map showing the orientation of magmatic layering in the mafic part of the Étoile Suite	13
Figure 3.2: Magmatic layering (plotted as poles to planes) and the corresponding mean vector (235/53 NW) plotted as a great circle .....	14
Figure 3.3: Map showing localities of the 40 samples used in this study .....	15
Figure 4.1: Field photographs of selected outcrops from the mafic part of the Étoile Suite .....	24
Figure 4.2: Field photographs of two pegmatoidal gabbros and a fine-grained mafic enclave found in the mafic part of the Étoile Suite .....	25
Figure 4.3: Samples from the mafic part of the Étoile Suite plotted in the plagioclase-clinopyroxene-olivine ternary diagram of Streckeisen (1976) .....	26
Figure 4.4: Cumulus assemblages vs. stratigraphic height for the mafic part of the Étoile Suite intrusion.....	28
Figure 4.5: Photomicrographs displaying selected features of plagioclase .....	30
Figure 4.6: XPL photomicrographs displaying selected features of olivine .....	33
Figure 4.7: XPL photomicrographs showing key features of clinopyroxene .....	34
Figure 4.8: XPL photomicrographs showing key features of the oxides .....	36
Figure 4.9: Reflected light photomicrographs displaying the key textural characteristics of the oxides .....	38
Figure 4.10: Back-scattered electron images, highlighting the three types of hercynite exsolution textures .....	39
Figure 4.11: XPL photomicrographs highlighting key features of amphibole, biotite and apatite .....	41
Figure 4.12: Photomicrographs of sulphides .....	42
Figure 4.13: SEM map of the oxide-rich wehrlite .....	44
Figure 4.14: Detailed SEM map revealing exsolutions of ulvöspinel (pink) and hercynite (green) in magnetite (red) within oxide-rich wehrlite .....	45
Figure 4.15: SEM map of the oxide-bearing gabbro .....	47
Figure 4.16: Close-up of a fine-grained portion of sample RM13 .....	47
Figure 4.17: High-resolution element map of a magnetite grain in RM13 .....	48
Figure 4.18: Bivariate diagrams displaying whole-rock data for the mafic part of the Étoile Suite ...	51
Figure 4.19: High-silica samples (A) and low-silica samples (B) plotted in the clinopyroxene-plagioclase-olivine ternary diagram of Streckeisen (1976).....	51
Figure 4.20: Whole-rock concentrations of MgO (A), Al <sub>2</sub> O <sub>3</sub> (B), FeO <sub>(total)</sub> (C), TiO <sub>2</sub> (D), V <sub>2</sub> O <sub>3</sub> (E) plotted as a function of stratigraphic height .....	52
Figure 4.21: Whole-rock concentrations of SiO <sub>2</sub> vs. Cr (A), Ni (B), Co (C), Cu (D), Sr (E), Zr (F), La (G), Th (H).....	54
Figure 4.22: Whole-rock concentrations of Cr (A), Ni (B), Co (C), Cu (D), Sr (E), Zr (F), La (G), Th (H) as a function of stratigraphic height in the intrusion .....	55
Figure 4.23: Multi-element variation diagrams showing signatures for high-silica samples (A) and low-silica samples (B) from the mafic part of Étoile Suite.....	56
Figure 4.24: Multi-element variation diagrams showing rare earth element (REE) signatures for high-silica samples (A) and low-silica samples (B).....	58
Figure 4.25: Albite-Anorthite-Orthoclase ternary diagram showing the composition of plagioclase in the intrusion.....	59

Figure 4.26: Histogram showing difference in An content of core and rim analyses of plagioclase .	60
Figure 4.27: Plagioclase An content (mol %) plotted against stratigraphic height.....	61
Figure 4.28: Histogram showing the difference in Fo between core and rim in olivine .....	62
Figure 4.29: Binary variation diagram showing Fo content of olivine vs. NiO in olivine .....	63
Figure 4.30: Stratigraphic variation of olivine according to: (A) Forsterite content (mol %) and (B) NiO (wt. %).....	64
Figure 4.31: Histogram showing the difference in Mg# between core and rim in clinopyroxene.....	65
Figure 4.32: Stratigraphic variation of clinopyroxene according to: (A) Mg# and (B) Cr <sub>2</sub> O <sub>3</sub> .....	66
Figure 4.33: Binary variation plots of Mg# of clinopyroxene versus a selection of elements in clinopyroxene .....	67
Figure 4.34: Multi-element variation diagram displaying average compositions of clinopyroxene in selected samples, as determined by LA-ICP-MS .....	68
Figure 4.35: Stratigraphic variation of Cr <sub>2</sub> O <sub>3</sub> (A), NiO (B), TiO <sub>2</sub> (C), and V <sub>2</sub> O <sub>3</sub> (D) contents of magnetite (Mt) vs. height, as determined by electron microprobe.....	69
Figure 4.36: TiO <sub>2</sub> content of magnetite versus the proportion of Fe-Ti oxides in the sample.....	70
Figure 4.37: Multi-element variation diagrams for magnetite from Zone A (A) and Zone B (B) of the Étoile Suite .....	71
Figure 4.38: Concentration of selected elements in ilmenite plotted against stratigraphic height. (A) Cr <sub>2</sub> O <sub>3</sub> . (B) NiO. (C) V <sub>2</sub> O <sub>3</sub> .....	73
Figure 5.1: fO <sub>2</sub> and temperature conditions marking the end of the oxy-exsolution process for each sample.....	81
Figure 5.2: Experimentally determined phase equilibria for synthetic ferrobasalt. Reproduced after Toplis and Carroll (1995). Permission acquired from Journal of Petrology. ....	83
Figure 5.3: V vs. Mg/V diagrams by Dare et al. (2019) for discrimination of magnetite forming massive to semi-massive V mineralization from magnetite forming disseminated V mineralization .....	84
Figure 5.4: Whole-rock Cu/Zr ratio as a function of stratigraphic height in the mafic part of the Étoile Suite .....	86
Figure 5.5: Distribution of anorthosite massifs and major mafic intrusions as well as their Fe-Ti deposits in the Grenville Province.....	88
Figure 5.6: Regional geology of the area around the Kiglapait Intrusion and the Voisey's Bay deposit.....	90
Figure 5.7: Schematic cross section of the Kiglapait intrusion .....	91
Figure 5.8: Anorthite (An) content of plagioclase versus forsterite (Fo) content of olivine at Kiglapait (black diamonds), Voisey's Bay (orange circles), and the Étoile Suite.....	92
Figure 5.9: Nickel (Ni) in olivine versus forsterite (Fo) in olivine for troctolitic-gabbroic rocks from the Voisey's Bay Intrusion.....	94
Figure 5.10: Model for the formation of troctolitic (i.e., olivine rather than orthopyroxene bearing) intrusions in anorthosite-bearing terranes such as the Grenville Province and Nain Plutonic Suite .....	97
Figure 7.1: Variation of Cu/Pd at Sonju Lake.....	101

### List of Abbreviations

$fO_2$	Oxygen fugacity
AMCG	Anorthosite-mangerite-charnockite-granite
BSE	Backscattered electron
EMPA	Electron microprobe analysis
FMQ	Fayalite-magnetite-quartz
HREE	Heavy rare earth element
LabMaTer	Laboratoire des Matériaux Terrestres, Université du Québec à Chicoutimi
LA-ICP-MS	Laser ablation inductively coupled plasma mass spectrometry
LILE	Large-ion lithophile element
LIP	Large Igneous Province
LREE	Light rare earth element
LSJ	Lac Saint-Jean
LZ	Lower Zone
NAD83	North American Datum 1983
PCS	Percent solidified
PGE	Platinum-group element
PPL	Plane-polarized light
PSM	Portneuf-St.-Mauricie
QUILF	Quartz-ulvöspinel-ilmenite-fayalite
REE	Rare earth element
SEM	Scanning Electron Microscope
UQAC	Université du Québec à Chicoutimi
UZ	Upper Zone
XPL	Cross-polarized light

## **Acknowledgements**

This project was funded by the NSERC Discovery Grant (RGPIN/2015- 05924) of Professor Sarah Dare and supported by her Canada Research Chair in Geochemistry Applied to Ore Deposits.

I am forever grateful to my supervisor Sarah Dare for giving me the opportunity to work on this project and for always being there to answer my numerous questions. A sincere thanks also to Audrey Lavoie for LA-ICP-MS data acquisition and Mark Choquette for electron microprobe data acquisition. Thank you, Roger Ouellet, for accompanying me in the field and sharing your unmatched insight on the intrusion, particularly the vanadium-mineralized portion. Christian Tremblay, Benoit Lafrance, and Pedro Miloski also accompanied me in the field and helped me with sampling – I appreciate it very much. Thank you so much William Smith for generating the FESEM element maps and for always being available to discuss the results. Thank you, Donald Lindsley, for helping me operate the QUILF program. I very much appreciate Eduardo Mansur and Lina Lin for helping me settle in Chicoutimi. And lastly, I would like to thank my friends in Finland, the UK and Angola, as well as my family in Cardiff – you have been a constant source of support.

## Chapter 1

### Introduction

Magmatic Fe-Ti-V deposits are the most important source of global titanium and vanadium supplies (Kelley et al. 2017; Woodruff et al. 2017). To a first order, magmatic Fe-Ti-V deposits can be divided into two types, namely those hosted in mafic-ultramafic layered intrusions and those hosted in Proterozoic massif-type anorthosites (see database by Parks et al. 2017). Examples of the former include the Main Magnetite Layer of the Bushveld Complex, South Africa (e.g., Wager and Brown 1968; Klemm et al. 1985) and the Fe-Ti oxide ores of the Panzhihua Intrusion, China (e.g., Pang et al. 2008); Examples of the latter include Buttercup, Canada (Corriveau et al. 2007) and La Blache, Canada (Corriveau et al. 2007; Buro 2011; Grant 2020). Fe-Ti-V deposits in layered intrusions appear to be more economic, based on the fact that a greater number of them are actively mined (see database by Parks et al. 2017).

Mafic-ultramafic layered intrusions are typically associated with Large Igneous Province (LIP) magmatism (Ernst et al. 2019), which, in turn, is associated with mantle plumes and intraplate tectonic settings (Bryan and Ernst 2008). The intrusions display a wide range of rock types, ranging from dunites, peridotites and pyroxenites, to gabbro-norites, anorthosites, diorites and granites. Mafic-ultramafic layered intrusions do not represent liquid compositions, but rather accumulations (i.e., cumulates) of mainly olivine, pyroxene and plagioclase (Wager and Brown 1968; Namur et al. 2015). The Fe-Ti-V deposits typically occur in the upper (i.e., mafic) portions of the intrusions, because ilmenite and magnetite (the primary host minerals of titanium and vanadium, respectively) emerge relatively late in the crystallisation sequence of ferrobasic magmas (Toplis and Carroll 1996). The formation of magnetite- and ilmenite-bearing ores in layered intrusions has traditionally been attributed to gravitational settling (Wager and Brown 1968), due in part to the stratiform and laterally-continuous nature of the deposits.

Proterozoic massif-type anorthosites are interpreted to form in convergent margin settings (Corrigan and Hanmer 1997; Ashwal and Bybee 2017). As their name suggests, the intrusions consist primarily (i.e., >90 %) of anorthosite, but their common occurrence with coeval mangerites, charnockites, and granites has led to the term 'AMCG complex.' The umbrella term 'anorthositic suite' is also sometimes used in order to account for all lithologies considered

consanguineous with anorthosite (Ashwal 1993). Anorthosite massifs form via the coalescence of plagioclase-rich mushes at the mid-crust level, after (1) ponding of basaltic magmas at the base of the crust, (2) crystallisation and sinking of mafic silicates, and (3) diapiric rise of buoyant plagioclase flotation cumulates (Emslie 1979; Emslie 1980; Ashwal 1993). Massif-type anorthosites therefore also represent cumulates rather than liquid compositions. Fe-Ti(V) oxide bodies in massif-type anorthosites typically form massive to semi-massive discordant lenses or pods (see review by Charlier et al. 2015). The cross-cutting relationship of these Fe-Ti(V) oxide ores is difficult to reconcile with gravitational settling of crystals, which has led some authors to believe that the ores were emplaced as Fe-oxide liquids (Philpotts 1967; Zhou et al. 2005) or via solid-state remobilisation (Duchesne 1999; Charlier et al. 2015).

It is not uncommon to find discrete coeval troctolitic-gabbroic layered intrusions within or in the vicinity of Proterozoic anorthositic suites (Scoates and Mitchell 2000). Most troctolitic intrusions consist of cumulates displaying varying degrees of igneous layering (Scoates and Mitchell 2000). Well-known examples of troctolitic-gabbroic intrusions associated with anorthositic suites include the Kiglapait Intrusion (Morse 1969) – hosting V-bearing oxide mineralisation – and the Voisey's Bay Intrusion (Naldrett 1996) – hosting Ni-Cu sulphide mineralisation – in the Nain Plutonic Suite, Labrador, Canada.

The present study aims to unravel the petrogenesis of the mafic part of the 'Étoile Suite,' a troctolitic-gabbroic layered intrusion in the central Grenville Province, Quebec, Canada (Figure 1.1). The intrusion hosts Fe-Ti-V mineralization (the Lac Fabien Fe-Ti-V prospect), which is currently under investigation by SOQUEM. The mafic part of the Étoile Suite, recently dated at  $1148.3 \pm 9.6$  Ma (Jean David, personal communication), is temporally and spatially associated with AMCG magmatism in south-central Quebec.

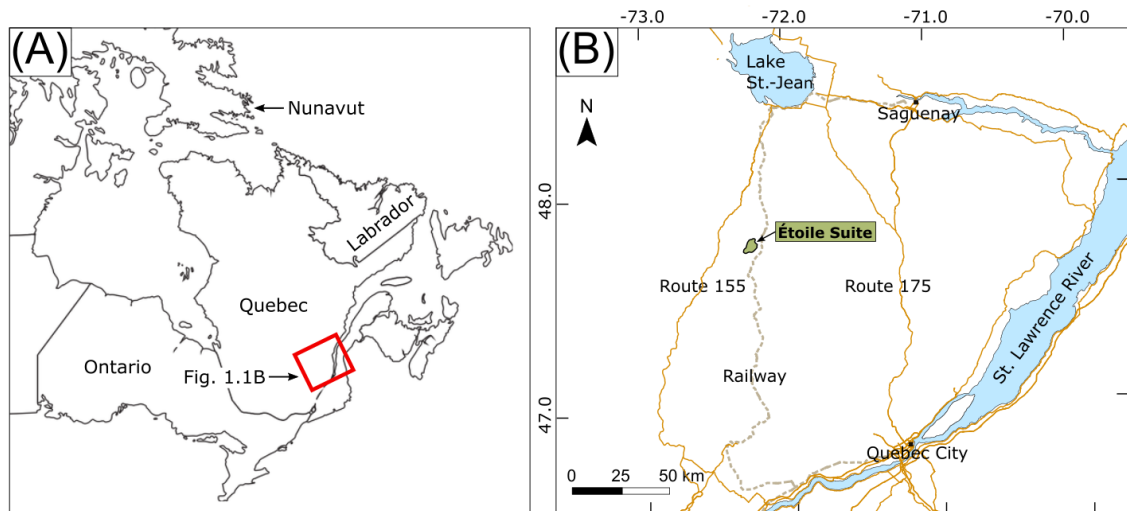


**Figure 1.1:** Location of the Étoile Suite within eastern Canada **(A)** and southern Quebec **(B)**.

A detailed study of the stratigraphic variation (petrographical and geochemical) of the mafic part of the Étoile Suite allows us to better understand the formation of V-bearing oxide mineralisation associated with AMCG magmatism. This study is based on 40 surface samples that were studied by employing transmitted and reflected light microscopy, scanning electron microscopy (SEM), whole-rock analysis, electron microprobe and laser ablation inductively coupled plasma mass spectrometry (LA-ICP-MS) analysis of minerals. These data are used to propose a petrogenetic model for the intrusion as well as some implications for exploration. The study shows that troctolitic-gabbroic layered intrusions in massif anorthosite-bearing terranes may also be prospective for Fe-Ti-V mineralisation in addition to LIP-type layered intrusions.

## Chapter 2

### Geological setting of the Étoile Suite

#### 2.1 Regional geology

The Étoile Suite is located within the south-central portion of the Grenville Province of eastern Canada (Figure 2.1). The Grenville Province represents the south-eastern margin of Proterozoic Laurentia and was the site of long-lived (>400 myr) Andean-style subduction from the Late Paleoproterozoic to the late Mesoproterozoic, resulting in the formation of calc-alkaline magmatic arcs (Rivers 1997). Subduction was interrupted by three periods of arc-accretionary orogenesis: the Labradorian (ca. 1680-1660 Ma, Gower and Krogh 2002), Pinwarian (ca. 1500-1450 Ma, Tucker and Gower 1990), and Elzevirian (ca. 1250-1190, Carr et al. 2000) orogenies (Rivers 1997). This terminated with a final period of Himalayan-style continent-continent collision, termed the Grenville Orogeny (ca. 1100-980, Rivers 2008), which marks the collision between Laurentia and Amazonia (Tohver et al. 2006).

The Grenville Province is characterised by two SE-dipping thrust faults that record NW-directed thrusting. The Allochthon Boundary Thrust (ABT) formed at ca. 1090, whereas the Grenville Front formed later, at ca. 1000 Ma (Rivers 2008) (Figure 2.1). The hangingwall of the Allochthon Boundary Thrust consists of several allochthonous belts, whereas the hangingwall of the Grenville Front consists of just one belt, termed the Parautochthonous Belt. The allochthonous belts were metamorphosed during the Ottawa orogenic phase (ca. 1090 to 1020 Ma, Rivers 2008). The Parautochthonous Belt was metamorphosed later during the Rigolet orogenic phase, at ca. 1000 to 980 Ma (Rivers 2008).

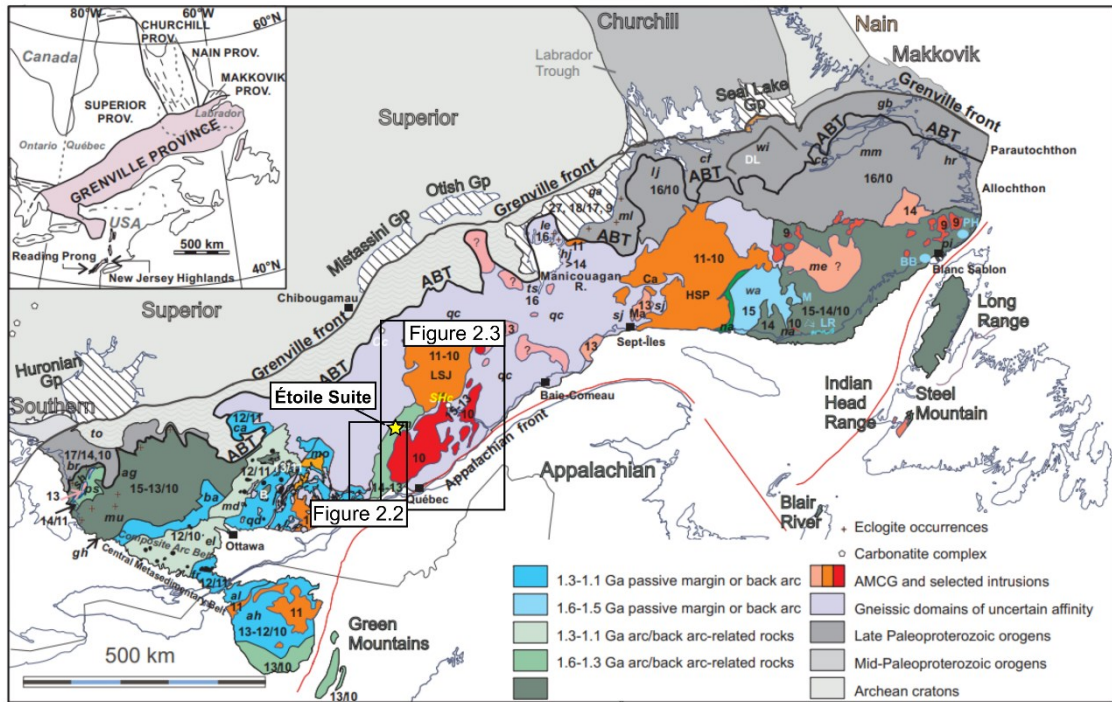


**Figure 2.1:** Geological subdivisions of the Grenville Province with deposition and intrusion age followed by metamorphic age in geons. Terranes (t.) and domains (d.): ag = Algonquin d.; ah = Adirondack Highlands; al = Adirondack Lowlands; ba = Bancroft t.; br = Britt d.; ca = Cabonga t.; cc = Cape Caribou River allochthon; cf = Churchill Falls t.; el = Elzevir t.; fr = Frontenac t.; ga = Gagnon t.; gb = Groswater Bay t.; gh = Go Home d.; hj = Hart Jaune t.; hr = Hawke River t.; le = Lelukuau t.; lj = Lake Joseph t.; M = Musquaro Lake extension of wa; md = marble-rich d.; me = Mécatina d.; ml = Molson Lake t.; mm = Mealy Mountains t.; mo = Morin t.; mu = Muskoka d.; na = Natashquan Domain; PH = Pitts Harbour Group; pi = Pinware t.; pm = Portneuf-Mauricie domain including the Montauban Group; ps = Parry Sound d.; qc = Quebecia; qd = quartzite-rich d.; sh = Shawanaga d.; to = Tomiko t.; ts = Tshenukutish t.; wa = Wakeham Group; wl = Wilson Lake t. Supracrustal units with hydrothermal alteration zones: B = Bondy Gneiss Complex; BB = Baie de Brador assemblage; DL = Disappointment Lake paragneiss; LR = La Romaine Supracrustal Belt. Potassic alkaline plutons of the Kensington-Skootamatta suite are the plutons in black in the Central Metasedimentary Belt. Cc = Crevier carbonatite; Shc = Saint-Honoré carbonatite. Anorthosite massifs: LSJ = Lac Saint-Jean; HSP = Havre Saint-Pierre. Modified after Corriveau et al. (2007). Permission: <https://gac.ca/about/who-we-are/>

Of specific interest amongst the allochthonous belts for this study, is the ‘allochthonous Medium to Low Pressure (aM-LP) Belt,’ which is subdivided into 17 terranes by Rivers (2008). One of them, termed the Portneuf-St.-Mauricie (PSM) domain (Figure 2.1), is a low-pressure terrane displaying low-pressure granulite to upper amphibolite facies metamorphism (Rivers 2008), and hosts the Étoile Suite (this study).

The oldest rocks in the Portneuf-St.-Mauricie domain are lithologies related to ~1.45-1.37 Ga pre-Grenvillian island arc magmatism (Nadeau and van Breemen 2001; Corrigan 1995) which formed the La Bostonnais Complex and Montauban Group (Figure 2.2). The key stages of island arc formation according to Sappin et al. (2009) are as follows:

- Northwest-directed intra-oceanic subduction at 1.45 Ga resulting in the formation of the Montauban island arc (quartzofeldspathic gneiss, minor quartzite, rare marble plus calc-silicate rocks, tholeiitic pillow metabasalt, lapilli metatuff).
- Formation of a back-arc basin behind the Montauban island arc (1.45 Ga-1.40 Ga).
- Emplacement of variably Ni-Cu ± PGE-mineralized calc-alkaline to tholeiitic plutons (mainly tonalite and diorite plus minor ultramafic to felsic rocks) of the La Bostonnais Complex into the Montauban arc, starting at 1.40 Ga.
- Accretion of the Montauban arc onto Laurentia as a result of subduction beneath Laurentia (1.39 Ga).
- End of emplacement of La Bostonnais Complex plutons at 1.37 Ga.

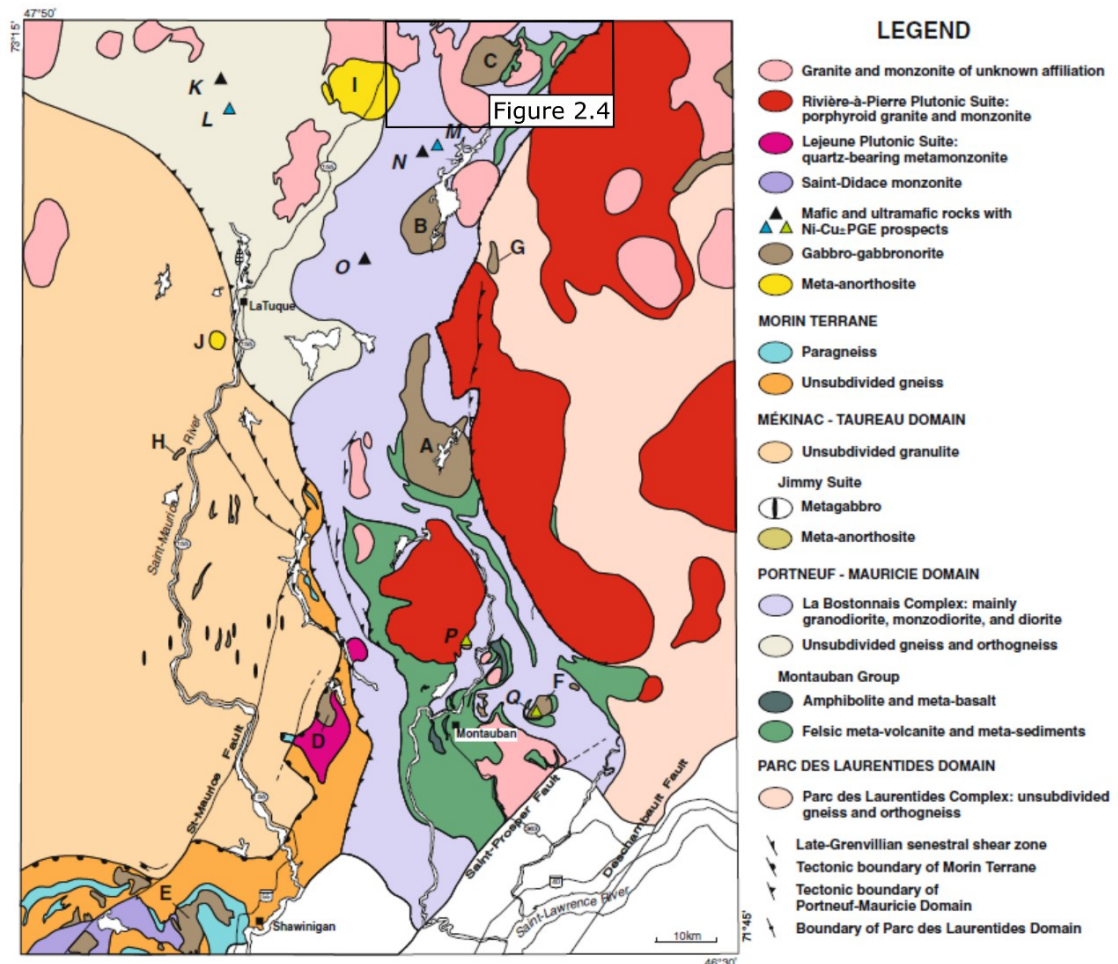


**Figure 2.2:** Simplified geological map of the Portneuf-Mauricie domain and adjacent geological units. Gabbro-gabbronorite and meta-anorthosite intrusions: A = Lapeyrère (1069 ± 2 Ma, Nadeau and van Breemen 2001), B = Édouard, C = Étoile (1148.3 ± 9.6 Ma, Jean David, personal communication), D = Lejeune, E = Shawinigan, F = Montauban, G = Sandford, H = Wessonneau, I = Langelier, and J = La Tuque. Mafic-ultramafic intrusions and associated Ni-Cu deposits: K =

Lac Matte, L = Lac Kennedy, M = Lac Édouard mine, N = Boivin, O = Rochette West ( $1386.1 \pm 1.2$  Ma, Sappin et al. 2009), P = Lac à la Vase (Rousseau prospect), and Q = Lac Nadeau ( $1396 \pm 6, -4$  Ma, Sappin et al. 2009). Black Ni-Cu prospects hosted by intrusions without particular internal structure; blue Ni-Cu prospects hosted by layered intrusions; green Ni-Cu prospects hosted by zoned intrusions. Modified by Sappin et al. (2011) after Nadeau and Brouillette 1994; 1995). Permission acquired from Mineralium Deposita.

The Portneuf-St.-Mauricie domain is located in the 'south-central' portion of the Grenville Province (Figure 2.3), which according to Hébert et al. (2005), records four episodes of anorthosite massif magmatism at: (1) 1327 Ma (De La Blache Mafic Plutonic Suite); (2) 1160-1135 Ma (Lac Saint-Jean Anorthositic Suite); (3) 1082-1045 (Pipmuacan Suite including the Parc des Laurentides AMCG Complex); and (4) 1020-1010 Ma (Valin Anorthositic Suite). The age of the mafic part of the Étoile Suite, using two samples from this study, is  $1147.3 \pm 4.4$  Ma and  $1148.3 \pm 9.6$  Ma (Jean David, personal communication), and is therefore cotemporaneous with episode two (1160-1135 Ma) of AMCG magmatism and is older than the nearby Lapeyrère mafic intrusion ( $1069 \pm 2$  Ma, Nadeau and van Breemen 2001).

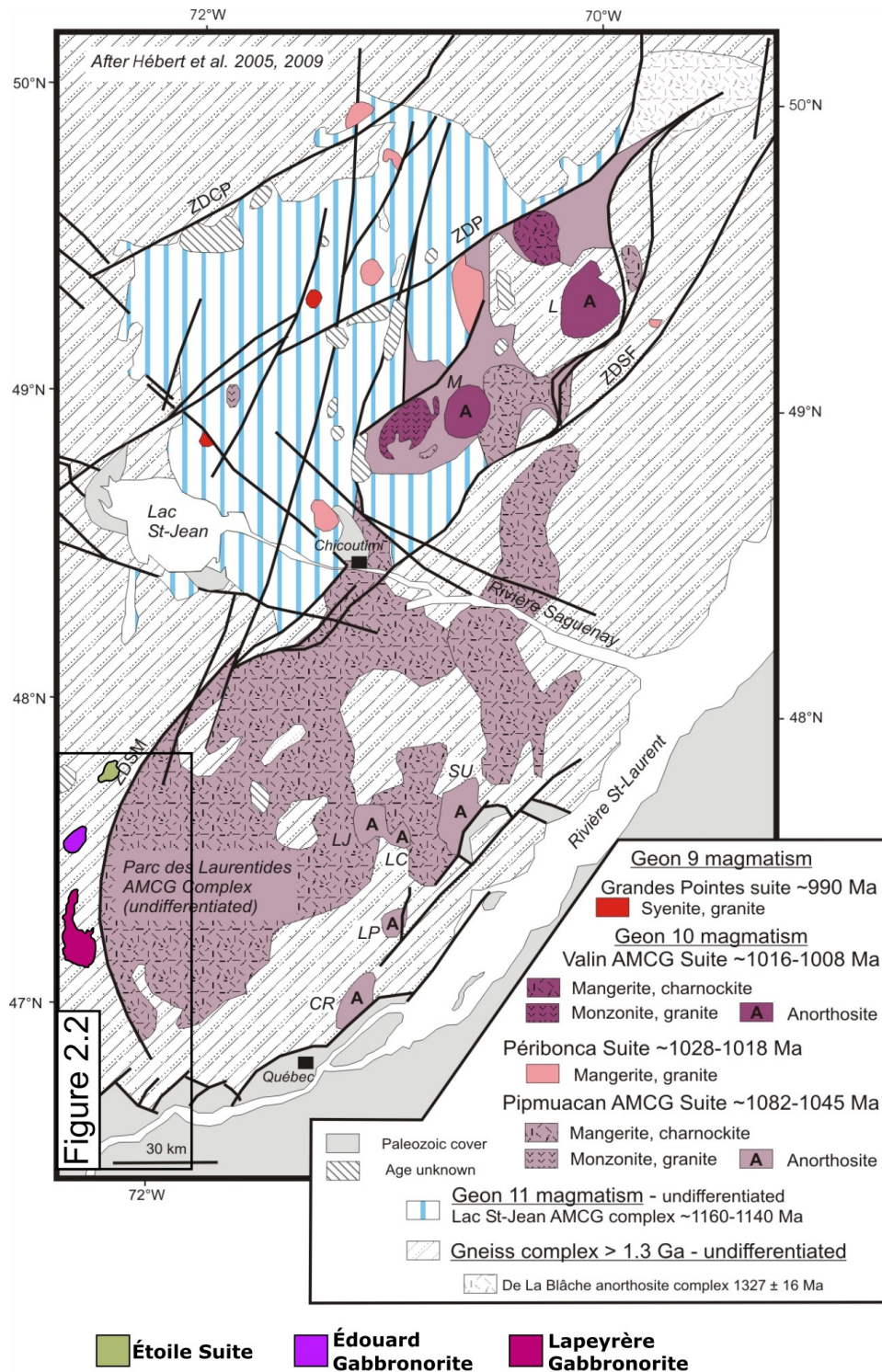


**Figure 2.3:** Geological map of the 'south-central' Grenville Province displaying the plutons associated with the four episodes of AMCG magmatism. Abbreviations: CR-Château Richer, L-Labrieville, LC-Lac Chaudière, LJ-Lac à Jack, LP-Lac Piché, M-Mattawa, SU-St. Urbain. ZDCP, ZDP, ZDSF, ZDSM represent Chute des Passes, Pipmuacan, St.-Fulgence, and St.-Mauricie deformation zones (ZD), respectively. Original figure by Rivers et al. 2012, modified after Hébert et al. 2005 and Hébert et al. 2009). Permission: <https://gac.ca/about/who-we-are/>

## 2.2 Geology of the Étoile Suite and Lac Fabien mineralized zone

The geology of the study area (Figure 2.4) can be summarised as being characterised by the emplacement of variably aged plutons into a basement consisting of the Montauban Group (1.45 Ga, Nadeau and van Breemen 1994) and the La Bostonnais Complex (1.41-1.37 Ga, Nadeau and van Breemen 1994; Corrigan 1995). The oldest pluton is the 33 km<sup>2</sup> Étoile Suite (1148.3 ± 9.6 Ma, Jean David, personal communication), emplaced during the second episode of Mesoproterozoic AMCG magmatism in the south-central Grenville Province. The second oldest is the large (~3500 km<sup>2</sup>) Rivière-à-Pierre Suite (1058 ± 2 Ma, Nadeau et al. 1992), which was emplaced during the third episode of Mesoproterozoic AMCG magmatism in the south-central Grenville Province (cf. Hébert et al. 2005; Figure 2.4). It is unknown when the other plutons (i.e., the Borgia Suite, Catherine Granite and Langelier Anorthosite) intruded into the area as they are undated.

The rocks of the Étoile Suite were first described by Perreault (1992) who recognized three lithological units forming the 'Suite de Lac Étoile': (1) Locally layered fine to medium grained gabbro, with lenses of magnetite and ilmenite; (2) Locally pegmatitic, coarse-grained leucocratic gabbro and black anorthosite; and (3) Coarse-grained anorthosite. Moukhsil and Côté (2018) adopted the name 'Suite d'Étoile,' or 'Étoile Suite' in English, in their revised geological map of the wider 'Borgia Lake' region. They divided the suite into a mafic-ultramafic unit (anorthosite, gabbro, troctolite, and pyroxenite) and a surrounding felsic unit (granite ± orthopyroxene, syenite, and mangerite) (Figure 2.4). The authors recognized a Fe-Ti-V occurrence in the mafic-ultramafic rocks in the vicinity of Lac Fabien (Figure 2.5). The present study deals with the mafic-ultramafic unit, hereafter called the 'mafic part of the Étoile Suite.'

The mineralization near Lac Fabien is characterised by magnetite- and ilmenite-rich wehrlites (Tremblay 2018) which are concentrated in a ~500 m-thick, 6000 m-long horizon that is well-delineated in aeromagnetic geophysical maps (Figure 2.5). A 2017-2018 surface sampling campaign by a group of prospectors from Saguenay (Groupe de Cinq) yielded whole-rock geochemical data on 50 samples, and concentrate data on four magnetite concentrates (Ouellet 2018). Most of the samples come from the mineralized zone near Lac Fabien (Figure 2.5). The whole-rock data show V<sub>2</sub>O<sub>5</sub> concentrations of 0.06-0.48 wt. %, and the concentrate data show

concentrations of 0.61-1.42 wt. % (Figure 2.5). As of May 2022, the Lac Fabien Vanadium Project was optioned by SOQUEM for further characterisation and exploration.

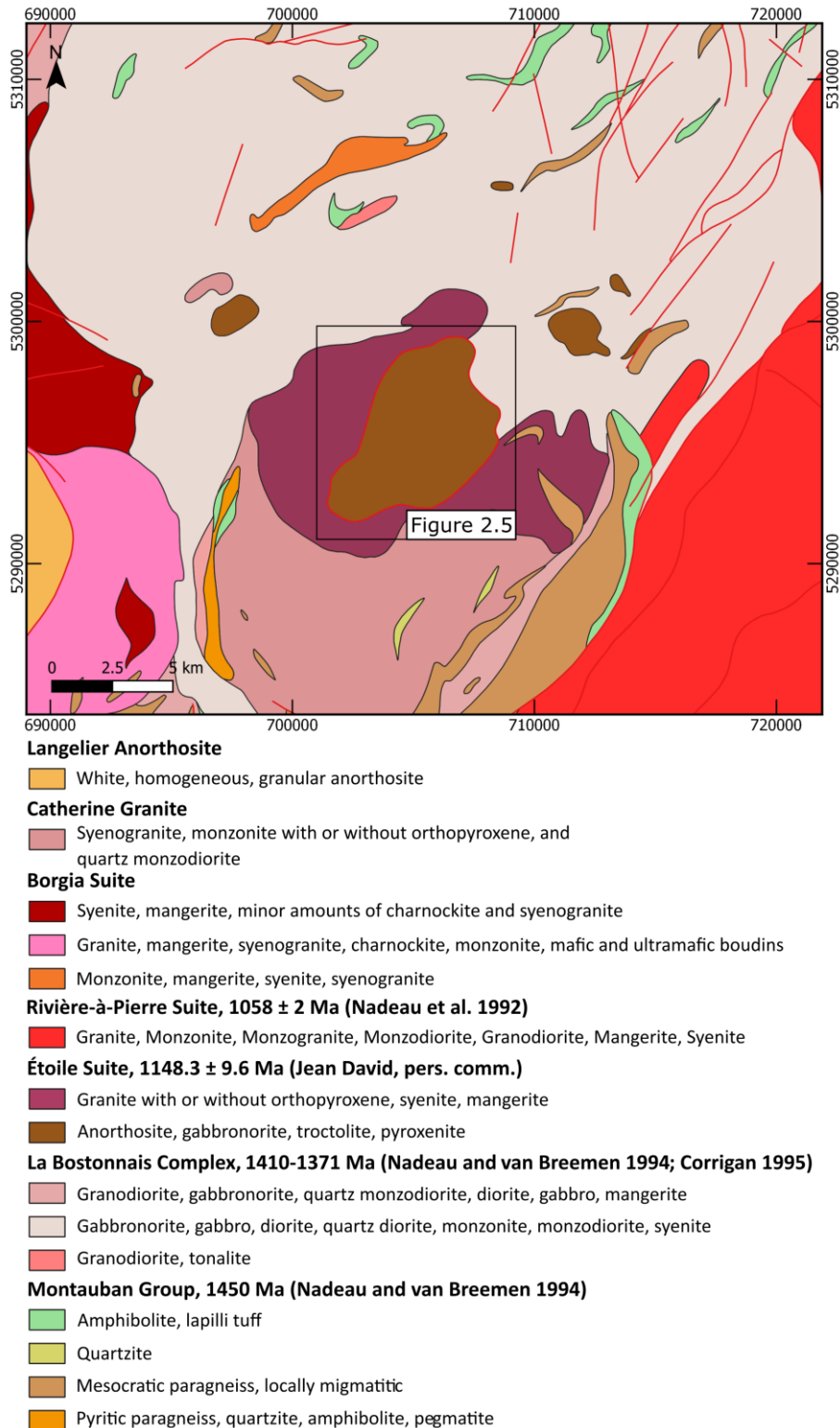


**Figure 2.4:** Local geology of the area around the Étoile Suite after Moukhsil and Côté (2018). Coordinate system: NAD83 – UTM Zone 18N.

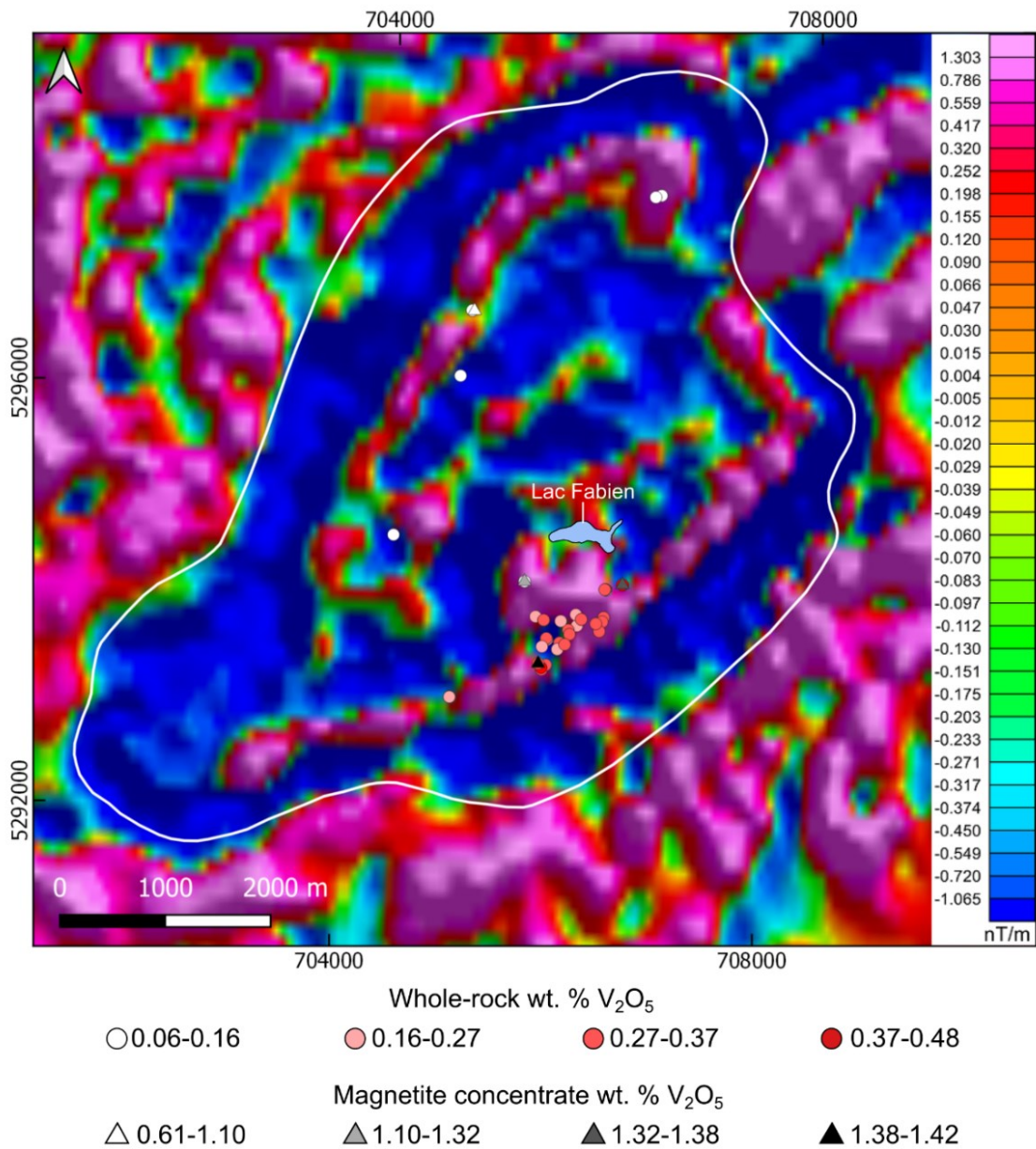


**Figure 2.5:** Map showing vertical gradient of residual magnetic field for the mafic part of the Étoile Suite. Source: système d'information géomineière du Québec (SIGEOM) by the Ministère de l'Énergie et des Ressources Naturelles (MERN). Available at [sigeom.mines.gouv.qc.ca](http://sigeom.mines.gouv.qc.ca). Whole-rock and concentrate data after Ouellet (2018). Boundary of intrusion after Moukhsil and Côté (2018). Coordinate system: NAD83 - UTM Zone 18N. Permission: [https://sigeom.mines.gouv.qc.ca/signet/classes/I3202\\_faq?l=A](https://sigeom.mines.gouv.qc.ca/signet/classes/I3202_faq?l=A)

## **Chapter 3**

### **Sampling and methodology**

#### **3.1 Sampling**

This study is based on 40 surface samples that were collected in Autumn 2019 and Summer 2020 (Figure 3.3; Appendix 1). This includes 12 samples from the prospector's collection (Ouellet 2018). The focus of the sampling strategy was to (a) make a stratigraphic column, and (b) attain pegmatoidal samples for the purpose of dating (following the method of Higgins and van Breemen 1996 for dating anorthosite massifs). Making a stratigraphic column requires good coverage of the entire intrusion, which was an issue at times as some areas of the intrusion were (a) difficult to access, and (b) lacking in exposure. There are a few roads and quarries in the area which aided the sampling process, but also introduced a sampling bias.

#### **3.2 Determination of the stratigraphic position of the analysed samples**

In order to provide stratigraphic context to the analysed surface samples, the following procedure was applied. First, the average strike ( $235^{\circ}$ ) and dip ( $53^{\circ}$ ) of the magmatic layering in the intrusion was determined in Stereonet 10 by Richard Allmendinger (Allmendinger et al. 2012; Cardozo and Allmendinger et al. 2013) (Figure 3.1; Figure 3.2).



**Figure 3.1:** Map showing the orientation of magmatic layering in the mafic part of the Étoile Suite ( $n = 10$ ). Outline of intrusion after Moukhsil and Côté (2018). Coordinate system: NAD83 - UTM Zone 18N.

A line with a strike of  $235^\circ$  was projected through the centre of the intrusion (the exact location of the line is inconsequential). The point on the intrusion's south-eastern margin that is farthest to the south-east of this line was interpreted to represent the base of the intrusion (the petrological and geochemical data in Chapter 4 informed the decision to designate the south-eastern margin as the base of the intrusion). A line with an azimuth of  $325^\circ$  was then projected from the base of the intrusion towards the north-west (Figure 3.3). The line's azimuth is  $90^\circ$  more than the strike of magmatic layering ( $235^\circ$ ), and represents the dip of the intrusion.

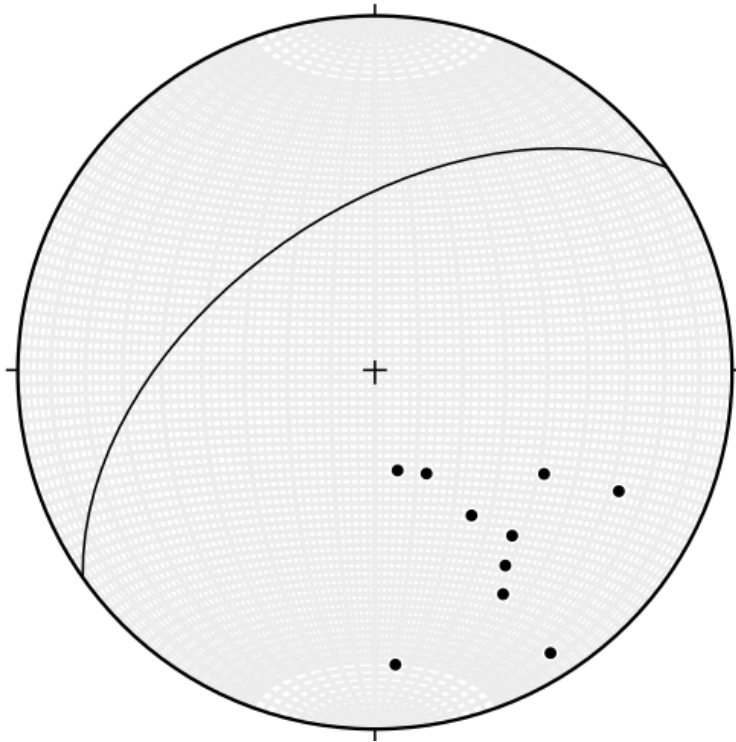


**Figure 3.2:** Magmatic layering (plotted as poles to planes) and the corresponding mean vector (235/53 NW) plotted as a great circle ( $n = 10$ ). Plotted in Stereonet 10 by Richard Allmendinger (Allmendinger et al. 2012; Cardozo and Allmendinger et al. 2013).

Lines parallel to the average strike of  $235^\circ$  were drawn through all sample positions (Figure 3.3). The intersect of these lines with the  $325^\circ$  'dip' line indicates the apparent stratigraphic height of each sample relative to the base of the intrusion. The apparent stratigraphic positions were converted to true height using the following equation:

$$\text{True height} = \text{apparent height} * \sin(\text{mean dip of magmatic layering}) \text{ (Equation 1)}$$

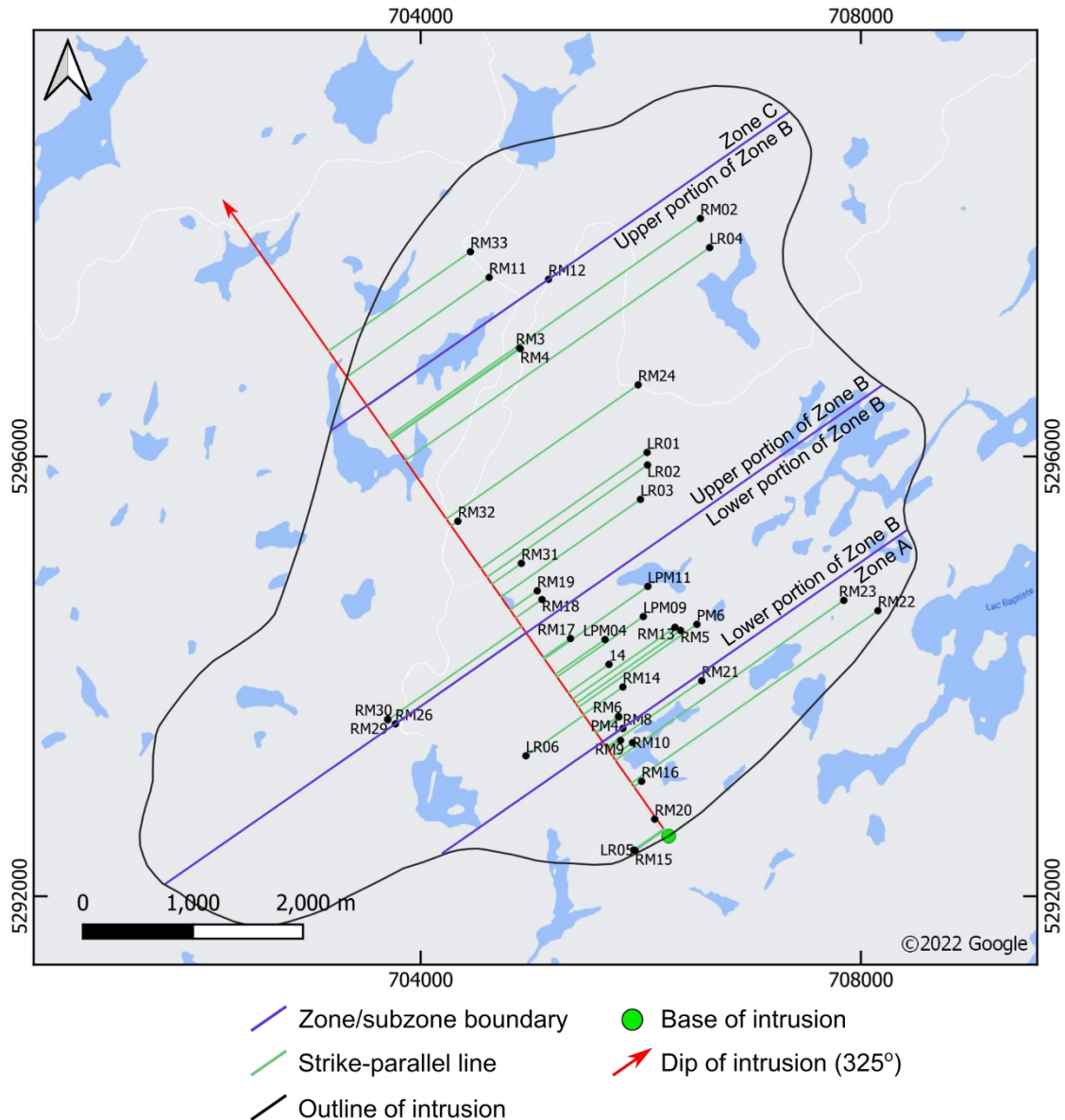


**Figure 3.3:** Map showing localities of the 40 samples used in this study. Green lines (235°) are strike-parallel lines projected from each sample to the 'dip' line (in red), which is at 90° to strike. Outline of intrusion after Moukhsil and Côté (2018). Coordinates for base of intrusion are x = 706253.35, y = 5292544.99. Coordinate system: NAD83 - UTM Zone 18N.

### 3.3 Point counting

Point counting was carried out on 40 polished thin sections. 300 points were counted for each sample using a grid of 1 mm x 2 mm. The phases that were counted were plagioclase, olivine, clinopyroxene, Fe-Ti oxides, amphibole, biotite, orthopyroxene, hercynite, serpentine and apatite. The percentage of each mineral in the sample is given by the formula:

$$\text{Vol. \% of mineral in sample} = 100 * \frac{\text{points counted of mineral}}{\text{total points counted}} \quad (\text{Equation 2})$$

Modal proportion results are presented in Appendix 1.

### **3.4 Element maps**

High-spatial resolution element maps were produced at Cardiff University (Wales, United Kingdom) using a Carl Zeiss Sigma HD Analytical Field Emission Gun Scanning Electron Microscope (FEGSEM) equipped with two Oxford Instruments 150 mm<sup>2</sup> energy dispersive spectrometers. All element maps were produced using an accelerating voltage of 20 kV, a 120 µm final aperture in high current mode, a nominal beam current of 8.5 nA and a working distance of 8.9 mm. Although the electron beam remained stable within 1 % relative over periods of hours, beam current drift was optimised using a pure cobalt standard between element maps. Magnification and resolution (i.e., pixel step size) were selected based on the analyte and analyses duration. For entire sections, a step size of 15-20 µm and a pixel dwell time of 10,000 µs was used, whereas for enhanced maps of oxide exsolution, a step size of 2-5 µm and a pixel dwell time of 20,000 µs was used. The acquired maps were processed and exported in AZtec 5.0 software. The final maps were produced in ImageJTM software by using a Kuwahara filter to reduce the number of unassigned pixels. Modal mineralogy was then computed in ImageJTM software.

### **3.5 Whole-rock analyses**

38 sample rock powders were made using an alumina mill at UQAC, and quartz sand was milled between each sample to minimise cross-sample contamination. Major element and trace element whole-rock analysis was carried out by analysing glass beads via laser ablation inductively coupled plasma spectrometry (LA-ICP-MS), following the protocol of Barnes et al. (2020) at LabMaTer, UQAC (Appendix 2). The glass beads were synthesised via fusion of sample rock powders and lithium borate (2 g). 0.2 g of rock powder was used for oxide-rich rocks (>20 vol. % oxides), and 0.5 g of rock powder was used for oxide-poor rocks (<20 vol. % oxides). An in-house reference material (MIX-KPT-610) was used for calibration and a mixture of silicate (KPT, KPT-GSE, LK-NIP, OKUM, and AN-G) and oxide-rich (BC-28, and Iron Ore) reference

materials were used to monitor data quality. Most analyses agree with working values, but Sc, Zn, Cs, Tm, Pb, and U are notable exceptions (Appendix 2).

### **3.6 Electron microprobe analyses**

Major and minor elements were obtained for silicates, Fe-Ti oxides and apatite using the CAMECA SX100 electron microprobe (EMPA) at Laval University, Québec. Their results are presented in Appendix 3.

#### **3.6.1 Silicates**

The silicate minerals analysed by EMPA include plagioclase (n = 197), olivine (n = 103), clinopyroxene (n = 186), orthopyroxene (n = 3), amphibole (n = 64) and biotite (n = 23). Typically, eight spot analyses were taken per mineral, per thin section. For each grain, a core and rim analysis was taken in order to ascertain the degree of chemical zonation in each grain. The element list for each silicate analysis was: Si, Ti, Al, Cr, Fe, Mn, Mg, Ca, Na, K (plus F and Cl for amphibole and biotite). The parameters used for the analyses were a beam diameter of 5 µm, a beam current of 20 nA, and a beam energy of 15 keV.

#### **3.6.2 Fe-Ti oxides**

The Fe-Ti oxide minerals analysed by EMPA in this project were magnetite (n = 113), ilmenite (n = 161), and hercynite (n = 62). Typically, four separate grains of each mineral were analysed per thin section. For ilmenite, both coarse grains and exsolutions were analysed. The element list for each analysis was: P, Nb, Si, Ti, Al, V, Cr, Mg, Ca, Mn, Fe, Co, Ni and Na. The parameters used for the analyses were a beam diameter of 10 µm, a current of 20 nA, and an energy of 15 keV. A larger beam size was chosen for the Fe-Ti oxides in order to incorporate the fine-grained exsolutions that are commonly found in magnetite.

### 3.6.3 Apatite

Apatite from the two pegmatoidal gabbros was analysed (n = 6). The element list for each silicate analysis was: P, Si, S, Ti, Al, Mg, Ca, Mn, Fe, Na, H, F, and Cl. The parameters used for the analyses were: a beam diameter of 10 µm, a current of 20 nA, and an energy of 15 kV.

### 3.7 Laser ablation inductively coupled plasma mass spectrometry (LA-ICP-MS)

*In situ* laser ablation inductively coupled plasma mass spectrometry (LA-ICP-MS) analyses were carried out on silicates (plagioclase n = 32; olivine n = 15; clinopyroxene n = 32), Fe-Ti oxides (magnetite n = 49; ilmenite n = 63; hercynite n = 20) and apatite (n = 6), on polished thin sections, at LabMaTer (UQAC) using a RESOLUTION ArF-193nm excimer laser ablation system (Australian Scientific Instruments), equipped with a double-volume 31 cell S-155 (Laurin Technics), coupled to an Agilent 7900 ICP-MS (Table 3.1). The analytical protocols are summarised in Table 3.1. The full LA-ICP-MS dataset (including calibration) is provided in Appendix 4.

**Table 3.1:** Analytical details for LA-ICP-MS analyses.

	<b>Fe-Ti oxides</b>	<b>Silicates</b>	<b>Apatite</b>
Number of samples	14	9	2
Number of analyses	83	72	6
Laser frequency	15 hz	15 hz	15 hz
Isotope list	<sup>24</sup> Mg, <sup>27</sup> Al, <sup>29</sup> Si, <sup>31</sup> P, <sup>34</sup> S, <sup>44</sup> Ca, <sup>45</sup> Sc, <sup>49</sup> Ti, <sup>51</sup> V, <sup>52</sup> Cr, <sup>53</sup> Cr, <sup>55</sup> Mn, <sup>57</sup> Fe, <sup>59</sup> Co, <sup>60</sup> Ni, <sup>63</sup> Cu, <sup>65</sup> Cu, <sup>66</sup> Zn, <sup>71</sup> Ga,	<sup>7</sup> Li, <sup>23</sup> Na, <sup>24</sup> Mg, <sup>27</sup> Al, <sup>29</sup> Si, <sup>31</sup> P, <sup>39</sup> K, <sup>44</sup> Ca, <sup>45</sup> Sc, <sup>49</sup> Ti, <sup>51</sup> V, <sup>52</sup> Cr, <sup>53</sup> Cr, <sup>55</sup> Mn, <sup>57</sup> Fe, <sup>59</sup> Co, <sup>60</sup> Ni, <sup>63</sup> Cu, <sup>66</sup> Zn, <sup>71</sup> Ga, <sup>74</sup> Ge, <sup>85</sup> Rb, <sup>88</sup> Sr, <sup>89</sup> Y, <sup>90</sup> Zr, <sup>93</sup> Nb, <sup>133</sup> Cs, <sup>137</sup> Ba, <sup>139</sup> La, <sup>140</sup> Ce, <sup>141</sup> Pr, <sup>146</sup> Nd, <sup>147</sup> Sm, <sup>153</sup> Eu, <sup>157</sup> Gd, <sup>159</sup> Tb,	<sup>7</sup> Li, <sup>23</sup> Na, <sup>24</sup> Mg, <sup>27</sup> Al, <sup>29</sup> Si, <sup>31</sup> P, <sup>39</sup> K, <sup>44</sup> Ca, <sup>45</sup> Sc, <sup>49</sup> Ti, <sup>51</sup> V, <sup>52</sup> Cr, <sup>53</sup> Cr, <sup>55</sup> Mn, <sup>57</sup> Fe, <sup>59</sup> Co, <sup>60</sup> Ni, <sup>63</sup> Cu, <sup>66</sup> Zn, <sup>71</sup> Ga, <sup>74</sup> Ge, <sup>85</sup> Rb, <sup>88</sup> Sr, <sup>89</sup> Y, <sup>90</sup> Zr, <sup>93</sup> Nb, <sup>133</sup> Cs, <sup>137</sup> Ba, <sup>139</sup> La, <sup>140</sup> Ce, <sup>141</sup> Pr, <sup>146</sup> Nd, <sup>147</sup> Sm, <sup>153</sup> Eu, <sup>157</sup> Gd, <sup>159</sup> Tb,

	<sup>74</sup> Ge, <sup>75</sup> As, <sup>89</sup> Y, <sup>92</sup> Zr, <sup>93</sup> Nb, <sup>95</sup> Mo, <sup>118</sup> Sn, <sup>139</sup> La, <sup>172</sup> Yb, <sup>178</sup> Hf, <sup>181</sup> Ta, <sup>182</sup> W, <sup>193</sup> Ir, <sup>208</sup> Pb	<sup>146</sup> Nd, <sup>147</sup> Sm, <sup>153</sup> Eu, <sup>157</sup> Gd, <sup>159</sup> Tb, <sup>161</sup> Dy, <sup>165</sup> Ho, <sup>166</sup> Er, <sup>169</sup> Tm, <sup>172</sup> Yb, <sup>175</sup> Lu, <sup>178</sup> Hf, <sup>181</sup> Ta, <sup>182</sup> W, <sup>208</sup> Pb, <sup>232</sup> Th, <sup>238</sup> U	<sup>161</sup> Dy, <sup>165</sup> Ho, <sup>166</sup> Er, <sup>169</sup> Tm, <sup>172</sup> Yb, <sup>175</sup> Lu, <sup>178</sup> Hf, <sup>181</sup> Ta, <sup>182</sup> W, <sup>208</sup> Pb, <sup>232</sup> Th, <sup>238</sup> U
Pulse energy	5 mJ/cm <sup>2</sup>	5 mJ/cm <sup>2</sup>	5 mJ/cm <sup>2</sup>
Stage speed	5-10 μm/s	5-10 μm/s	5-10 μm/s
Beam diameter	11, 15, 19, 25, 33, 55 μm	55 μm	55 μm
Line length	300-600 μm	300-600 μm	300-600 μm
Dwell times	10 ms (13 August 2020) 8 ms (18 August 2020)	5 ms	5 ms
Analysis Procedure	30 s of glass bank, 60 s of signal	30 s of glass bank, 60 s of signal	30 s of glass bank, 60 s of signal
Carrier gas flow	Helium (1/L/min)	Helium (1/L/min)	Helium (1/L/min)
Ar flow rate	0.7 L/min	0.7 L/min	0.7 L/min
Internal standard	<sup>57</sup> Fe (from electron microprobe)	<sup>29</sup> Si (from electron microprobe)	<sup>44</sup> Ca (from electron microprobe)
Reference material for calibration	GSE-1g	GSE-1g	NIST610
Reference materials (glasses) for data quality	GSD-1g, Gprob6	GSD-1g, Gprob6, NIST-610,	Gprob6, GSD-1g, NIST-612,

In-house monitor	BC-28 (magnetite)		
Data reduction	Iolite version 2.5 (Patton et al. 2011)		

### 3.7.1 Data quality for silicate analyses

All elements are accurate and precise to within 10 % according to the analyses of reference material GSD-1g, except for P, which is poorly calibrated by GSE-1g. Analyses of Gprob6 show that Li, P, K, V, Zn, Ge, and Pb are slightly problematic (showing between 10 and 20 % deviation from the working value). NIST-610 analyses are accurate to within 20 % for all elements except for Fe. Mg (15.9 % off working value), and P (-10.8 % off working value) are also problematic (Appendix 4).

### 3.7.2 Data quality for Fe-Ti oxide analyses

5  $\mu\text{m}$  analyses of GSD-1g and Gprob6 are accurate and precise to within 10-15 % for all elements except P, S, Sc, Ta and Ir in GSD-1g and P, Zr, and Ta in Gprob6, which are more than 20 % off their working values. Other problematic elements (with a 10-20 % deviation from working values) are Sc, V, Cr, Ga, Ge, and Sn. For 55  $\mu\text{m}$  analyses of BC-28 (natural magnetite standard), the majority of elements, with abundance greater than 40 ppm, are accurate to within 20 % (Appendix 4).

### 3.7.3 Data quality for apatite analyses

For Gprob6, all elements are accurate to within 20 % of their working values. All elements are accurate to within 20 % for GSD-1g, except for Ge. Only the elements P and Ge are >20 % off their working values in GSE-1g. In the NIST-612 data, Cl, K, and Fe are more than 20 % off.

### 3.8 Oxygeothermometry

Using the QUILF program by Andersen et al. (1993),  $\Delta \log fO_2$  (FMQ) and temperature values were obtained for a subset of 19 samples. The QUILF program uses the compositions olivine and pyroxene to help provide constraints on the temperature, pressure, oxygen fugacity, and activity of  $SiO_2$  at which Ti-magnetite, ilmenite, augite, pigeonite, orthopyroxene, olivine, and quartz (or subassemblages thereof) were last in equilibrium. The advantage of QUILF over traditional two-oxide thermometers (e.g., Andersen and Lindsley 1985) is that re-equilibration and alteration of the oxide phases does not affect the results attained for any of the parameters listed above because the QUILF assemblage is overdetermined (Andersen et al. 1993). Based on the advice of Donald Lindsley, the initial procedure was carried out as follows for the 19 Étoile Suite samples:

1. Electron microprobe weight percent analyses for magnetite, ilmenite, olivine and clinopyroxene were projected through the Edit→Weight Percent menu.
2. “1000?”, “-10?”, and “0.8?” were input into the temperature,  $fO_2$ , and silica activity fields, respectively. The question mark informs the program that the parameter is unknown, and therefore needs to be calculated.
3. A pressure of 5000 bars was specified, which is the pressure at which partial melting occurred in migmatites adjacent to a mafic-ultramafic intrusion (i.e., the 1.15 Ma Baie à Cadie Suite, Hébert et al. 2005; Hébert and van Breemen 2004) in the Lac Saint-Jean region of the south-central Grenville Province (Lin and Sawyer 2019). The instability of olivine – as evidenced by coronas bearing semblance to the orthopyroxene-amphibole coronas described by Woussen et al. (1981) (Figure 4.6F) – occurs roughly at more than or equal to 5 kbar according to the curve of Kushiro and Yoder (1966). 5 kbar therefore represents the minimum pressure reached in the Étoile Suite.

At this point, five question marks were placed after the values of certain mineral components in order to turn them into variables. First, question marks were added after NMg of spinel, XGk of ilmenite, and XEn of augite. This meant that the Mg content of olivine (XFo) was used to determine the Mg content of magnetite, ilmenite, and clinopyroxene. A question mark was then added after XLa in order to calculate the Ca content of olivine using the Ca content of Augite (XWo). At this point, there

are 4 unknowns (denoted by question marks) and 6 known mineral components. XHem of ilmenite was chosen as the 5<sup>th</sup> unknown in order to make the number of unknowns equal to the number of constraints. The results are presented in Table 5.1.

## Chapter 4

### Results

#### 4.1 General petrography

The mafic part of the Étoile Suite consists predominantly of plagioclase-, olivine-, and clinopyroxene-bearing gabbroic mesocumulates and adcumulates. The rocks are mostly medium grained and relatively unaltered and undeformed. Fe-Ti oxides, consisting mainly of magnetite and ilmenite, are common constituents, reaching maximum modal proportions of ~50 vol. % in the mineralized horizon. Fe-Ti oxides tend to be associated with the olivine- and clinopyroxene-enriched portions of samples. At the outcrop-scale, this occasionally results in decimetre-scale modal layering (defined by stratigraphic variations in the modal abundances of the cumulus minerals) (Figure 4.1A, B, C). Other types of layering that were observed include: (1) phase layering (defined by the appearance/disappearance of certain cumulus minerals at certain stratigraphic intervals, Figure 4.4); (2) cryptic layering (defined by systematic variations in the chemical composition of the cumulus minerals, see Chapter 4.6); and (3) rhythmic layering (defined by the repetition of the layering patterns, Figure 4.1D) (see Namur et al. 2015). In addition to olivine, plagioclase, clinopyroxene, and Fe-Ti oxides, the cumulates contain accessory hercynite, amphibole, biotite, apatite, and zircon. Cumulus orthopyroxene was found in only one sample. In addition to the cumulate rocks, the intrusion contains some lithologies with different granulometries, including:

- Two pegmatoidal to very coarse-grained samples, RM15 and RM29 – located at the southwestern margin, and centre of the intrusion, respectively. They are both relatively oxide-poor gabbros with 19-36 % plagioclase, 46-47 % clinopyroxene, 1-17 % olivine, 3-6 % Fe-Ti oxides, 0-7 % amphibole, 1-4 % biotite, and 3-9 % apatite. The two samples are interpreted to represent small (30 cm in diameter) pegmatitic pockets of evolved trapped liquid (containing zircon and apatite) rather than cumulates (based on Higgins and van Breemen 1996). Crystals reach up to 5 cm in size in the two samples (Figure 4.2).
- One sample (RM26F) that is a finer-grained mafic enclave (20 cm in size) that also displays a granular texture (Figure 4.2). It is located 1801 m above the base of the intrusion and

possibly represents an autolith of a chilled margin or an intraplutonic quench zone. The sample is a gabbro with 64 % plagioclase and 35 % clinopyroxene.

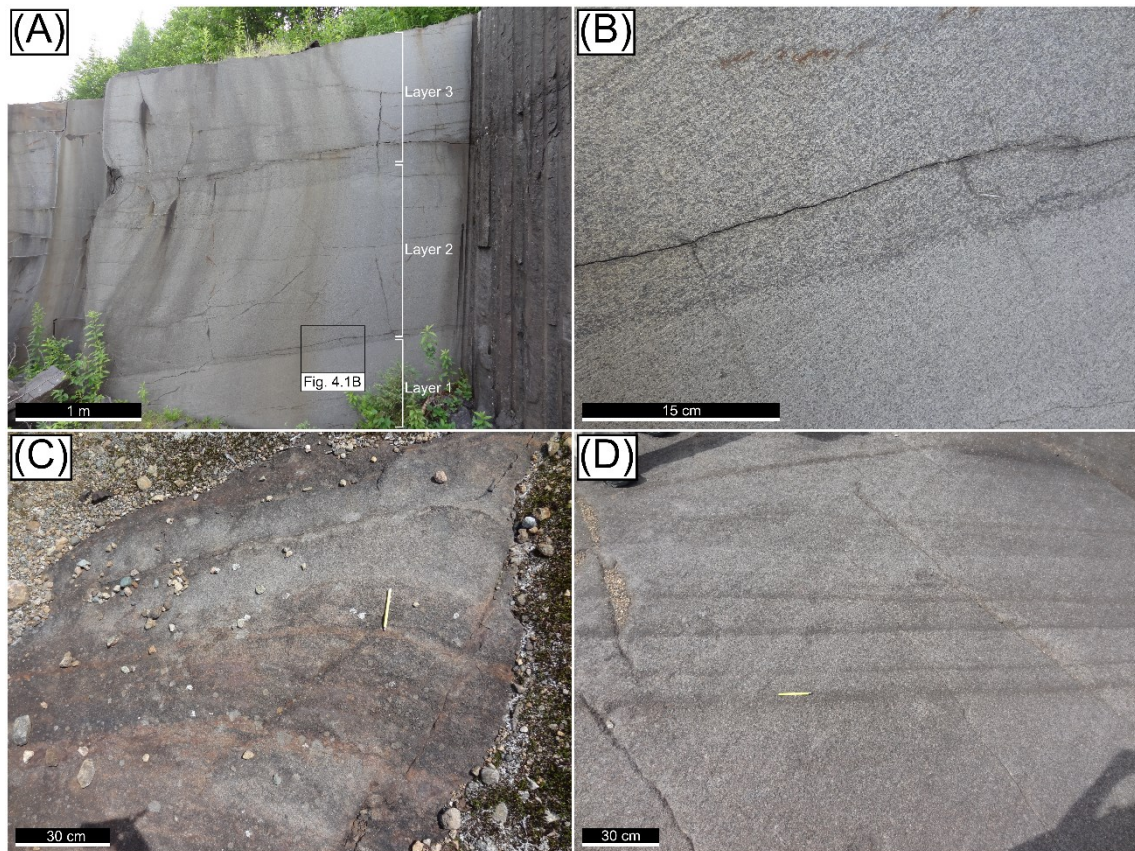


**Figure 4.1:** Field photographs of selected outcrops from the mafic part of the Étoile Suite. **(A)** Example of modal layering, where the base of the outcrop is noticeably more leucocratic than the top. Three distinct layers can be recognized. Layer 1 is leucogabbro. Layers 2 and 3 are mesogabbro. There is subtle modal layering within the three layers, especially in Layer 2. **(B)** Close-up photograph of the contact between Layer 1 and Layer 2 from Figure 4.1A. **(C)** Layers of mela-olivine-gabbro sandwiched between more leucocratic olivine gabbro. **(D)** Rhythmic layering in olivine gabbro defined by thin (<5 cm-thick) layers of mela-olivine-gabbro interlayered with more leucocratic olivine gabbro.

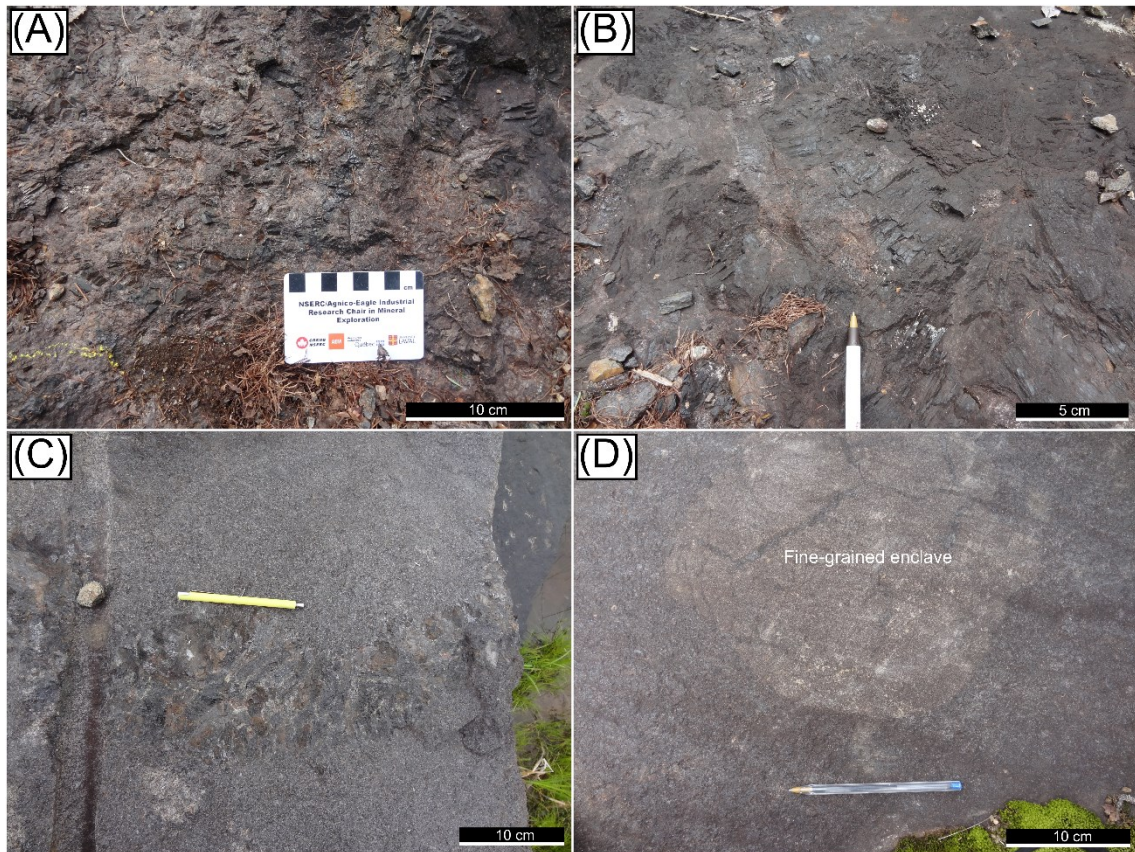


**Figure 4.2:** Field photographs of two pegmatoidal gabbros and a fine-grained mafic enclave found in the mafic part of the Étoile Suite. **(A)** and **(B)** Pegmatoidal gabbro with large (5 cm) crystals of plagioclase and clinopyroxene (RM15; Zone A; 54 m above the base). **(C)** Pegmatoidal gabbro with large (5 cm) crystals of plagioclase and clinopyroxene (RM29; Zone B; 1861 m above the base). **(D)** 20 cm-diameter fine-grained gabbroic enclave (RM26F; Zone B; 1805 m).

The proportions of the main silicate minerals of the mafic part of the Étoile Suite are plotted in the plagioclase-clinopyroxene-olivine ternary diagram of Streckeisen (1976) (Figure 4.3). The observed rock types include wehrlite (n = 6), mela-olivine-gabbro (n = 8), olivine gabbro (n = 6), leuco-olivine-gabbro (n = 6), gabbro (n = 9), leucogabbro (n = 4), and leucotroctolite (n = 1). Note that the relatively melanocratic rocks (<35 % plagioclase) tend to be relatively oxide-rich (>20 % Fe-Ti oxides).

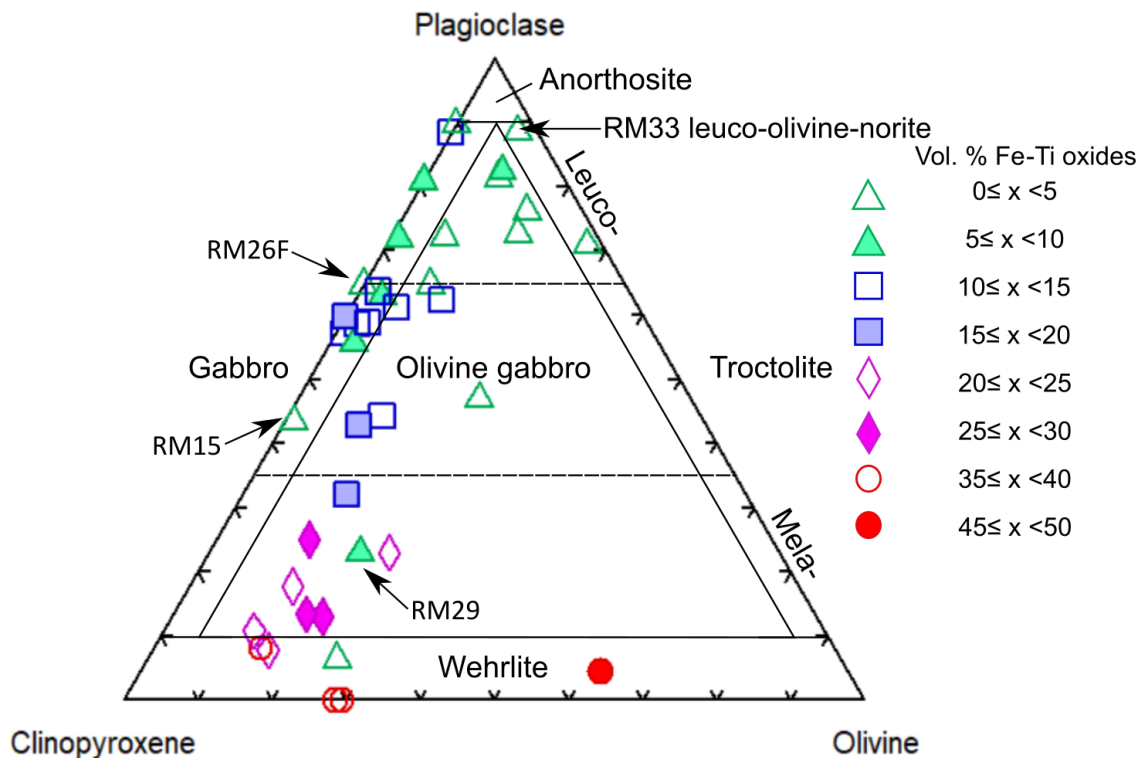


**Figure 4.3:** Samples from the mafic part of the Étoile Suite plotted in the plagioclase-clinopyroxene-olivine ternary diagram of Streckeisen (1976). RM15 and RM29 are the two pegmatites described above (Figure 4.2A, B, C). RM26F is the fine-grained enclave shown in Figure 4.2D. Mineral proportions determined by point counting.

#### 4.1.1 Stratigraphic variation in modal mineralogy

The proportions of the main rock-forming minerals in the mafic part of the Étoile Suite show considerable variation with stratigraphic height. The range in the modal proportions of plagioclase, olivine, clinopyroxene, and Fe-Ti oxides is 0 to 78 %, 0 to 28 %, 2 to 64 %, and 0 to 49 %, respectively. Amongst the oxide minerals, magnetite and ilmenite occur in broadly even proportions (see Chapter 5.3). Cumulus orthopyroxene is totally absent, except in the uppermost sample (RM33; 4304 m above the base) which is an olivine norite with 69 % plagioclase, 7 % olivine, 2 % clinopyroxene, and 8 % orthopyroxene.

On the basis of their cumulus mineralogy, the mafic part of the suite is subdivided into three distinct stratigraphic zones (A, B, C from bottom to top) (Figure 4.4). Zone A (0-832 m) is characterised by oxide-poor (typically  $\leq 3$  %) leuco-olivine-gabbros with intercumulus Fe-Ti oxides. Plagioclase and olivine are cumulus phases throughout, and clinopyroxene becomes a cumulus phase towards the top of the zone. Note that there is one sample at the very base of

Zone A that is somewhat anomalous in that it contains a relatively large proportion of cumulus Fe-Ti oxides (28 %, Figure 4.4).

Zone B (832-3815 m) is characterised by relatively high Fe-Ti oxide contents (12-49 %) and the onset of Fe-Ti oxide crystallisation. Plagioclase, olivine, clinopyroxene and the Fe-Ti oxides show cumulus habit throughout this part of the intrusion. Note that cumulus clinopyroxene starts to crystallise just before the oxides. Based on the proportion of plagioclase, this zone can be subdivided into a melanocratic lower portion and a leucocratic upper portion. The lower portion (832-1805 m) comprises olivine gabbros, mela-olivine-gabbros and wehrlites. It is mostly relatively poor in plagioclase (0-52 %), but enriched in olivine (2-28 %), clinopyroxene (15-59 %) and Fe-Ti oxides (12-49 %). The Lac Fabien V-rich oxide mineralisation is located near the base of Zone B, hosted predominantly in wehrlite containing 15-59 % clinopyroxene, and 2-28 % olivine.

The upper portion of Zone B (1805-3815 m) comprises predominantly olivine-free leucogabbros, that are richer in plagioclase (up to 78 %), but poorer in mafic silicates (olivine: 0-17 %, clinopyroxene: 8-57 %) and oxides (1-23 %) than the lower portion of Zone B. Plagioclase, clinopyroxene and oxides generally display cumulus habit throughout, whereas olivine only intermittently displays cumulus habit.

Zone C (>3815 m) bears certain similarities to Zone A in that both are characterised by oxide-poor leuco-olivine-gabbros. However, unique to Zone C is the presence of cumulus orthopyroxene at the very top (in sample RM33 at 4304 m).

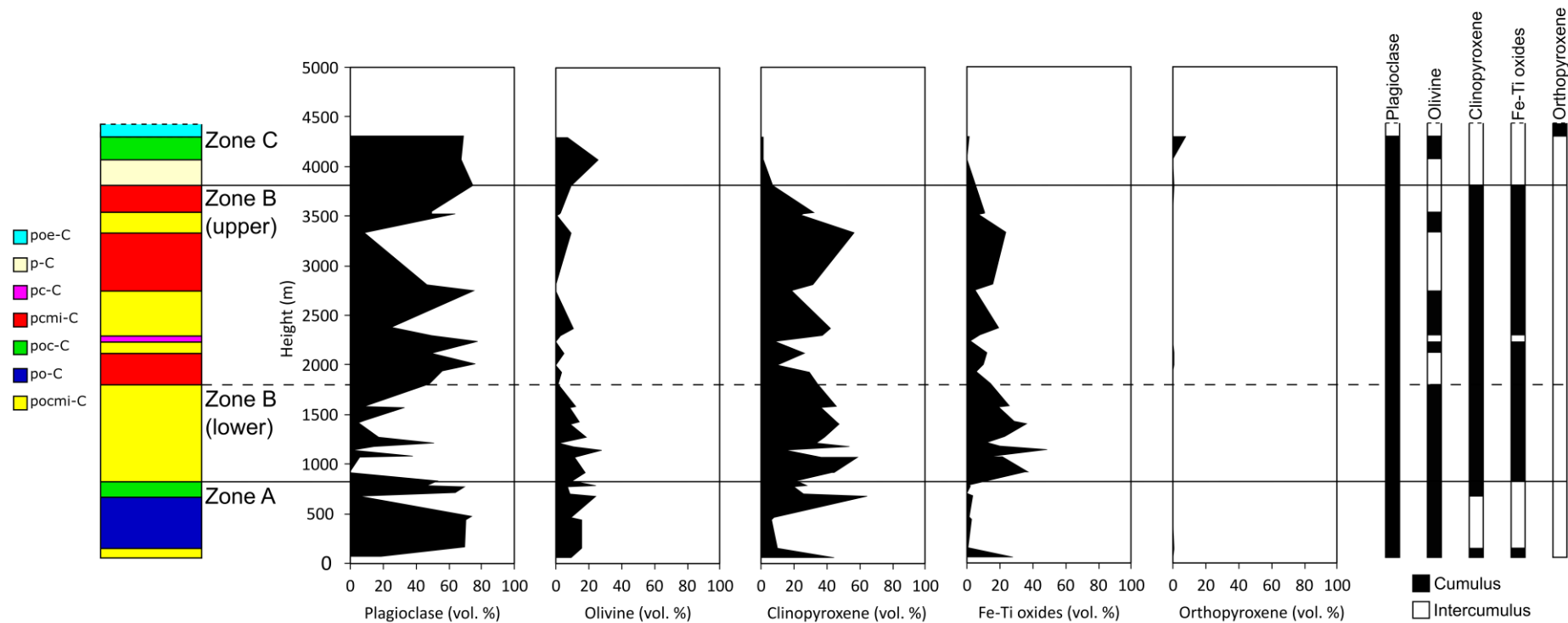


**Figure 4.4:** Cumulus assemblages vs. stratigraphic height for the mafic part of the Étoile Suite intrusion, following the nomenclature of Irvine (1982). P = plagioclase; o = olivine; c = clinopyroxene; m = magnetite; i = ilmenite; e = enstatite. Suffix '-C' stands for cumulate. Pegmatoidal gabbros (RM15 and RM29) are not plotted as they are not cumulates, and fine-grained enclave "RM26F" is not plotted, as it is possibly an autolith.

## 4.2 Petrography of the silicate minerals

### 4.2.1 Description of the main rock-forming minerals

#### *Plagioclase*

Plagioclase is the most abundant mineral in the intrusion and is always a cumulus phase, even when present in low abundance in the mineralized wehrlites at the base of Zone B. Plagioclase forms euhedral or subhedral tabular crystals with a typical grain size of 1-2 mm (Figure 4.5A, B). In rare cases, the plagioclase laths can be up to 10 mm in length, notably in the leucocratic cumulates of zones A and C (e.g., sample RM20 at 160 m and RM11 at 4073 m), as well as in the two pegmatoidal gabbros (RM15 at 54 m and RM29 at 1861 m) (Figure 4.7B). Plagioclase crystals are usually randomly oriented, but in some samples may define a preferred orientation, especially in more leucocratic lithologies, such as leuco-olivine-gabbro. Plagioclase-plagioclase grain boundaries are commonly straight (Figure 4.5A), and less commonly curved, irregular or interpenetrating (Figure 4.5C). The mineral shows rare signs of deformation in the form of bent and tapered twin lamellae, undulose extinction and subgrains (neoblasts) (e.g., Figure 4.5C). Deformation is most pronounced in samples RM31 and RM33 at ~2237 m (in the middle of Zone B) and 4304 m (at the top), respectively. In some rocks, plagioclase shows evidence of textural equilibration in the form of 120° dihedral angles at three-grain junctions (Figure 4.5D). The polygonal texture in part of the fine-grained enclave (sample RM26F) represents a particularly advanced degree of textural equilibration not seen in the remainder of the intrusion (Figure 4.5E). In some samples, plagioclase forms clusters of grains that are separated by clinopyroxene- and olivine-rich domains (Figure 4.5F). Plagioclase is generally unaltered, only a few grains show minor sericitisation.

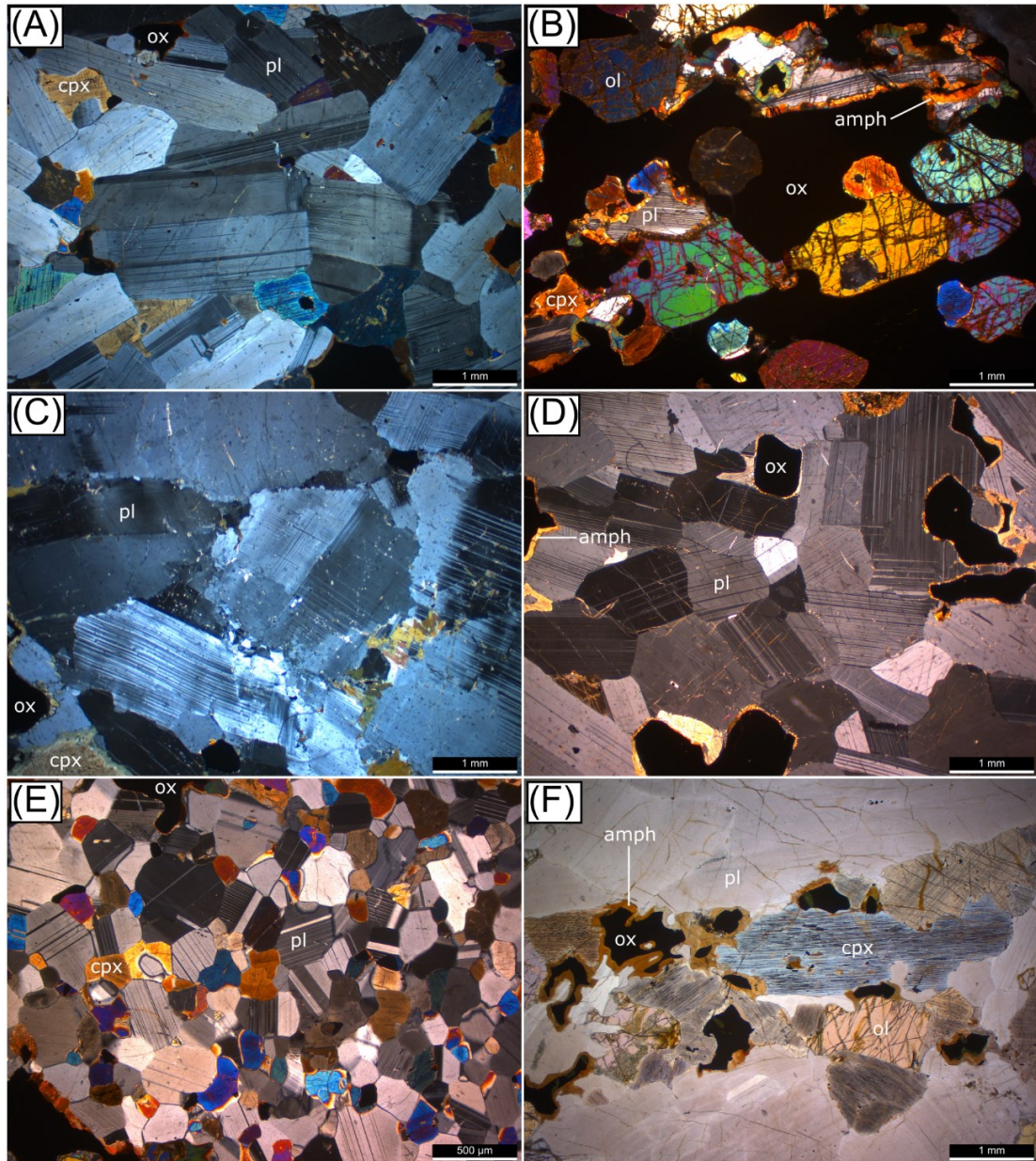


**Figure 4.5:** Photomicrographs displaying selected features of plagioclase. A-E are taken under cross-polarised light (XPL). F is taken under plane-polarised light (PPL). **(A)** Leucogabbro with cumulus crystals of euhedral and subhedral tabular plagioclase, with some intercumulus clinopyroxene (RM32; Zone B; 2752 m). **(B)** Cumulus plagioclase in oxide-rich wehrlite. Note reaction coronas between plagioclase and Fe-Ti oxides (PM6; Zone B; 1143 m). **(C)** Relatively deformed plagioclase in leucogabbro. Deformation manifests itself in the form of bent twin lamellae, undulose extinction and subgrain formation. (RM31; Zone B; 2237 m). **(D)** Texturally-equilibrated domain of plagioclase adcumulate in leucogabbro (RM19; Zone B; 2007 m). **(E)** Fine-grained gabbro with a polygonal texture (RM26F; Zone B; 1805 m). **(F)** Olivine gabbro showing distinct oxide-olivine-clinopyroxene-rich domains and monomineralic plagioclase domains (RM21; Zone A; 787 m). Abbreviations: pl = plagioclase; ol = olivine; cpx = clinopyroxene; ox = oxide; amph = amphibole.

## *Olivine*

Olivine typically forms anhedral or, in rare cases, subhedral crystals 1-2 mm in size (Figure 4.6A, B). In some cases, olivine forms oikocrysts hosting small (0.2 mm) subrounded inclusions of plagioclase (Figure 4.6C) and/or oxide (Figure 4.6D) where they may form irregular extensions into interstitial space. Large oikocrysts, up to 10 mm in diameter (Figure 4.6E), are found in some rocks, especially in the leucocratic rocks of Zone A and Zone C. Olivine is generally unaltered, but some grains show minor serpentinisation. The mineral rarely shows undulose extinction or sector zoning, indicating negligible deformation.

In general, relatively equant grains (Figure 4.6A, C, D) are interpreted to be of cumulus origin whereas wedge-shaped crystals that fill the interstices between tabular plagioclase crystals (Figure 4.6B) are interpreted to be of intercumulus origin. However, as most equant grains form extensions into interstitial space, there is clearly significant postcumulus overgrowth, making the distinction between cumulus and postcumulus grains difficult and somewhat subjective. In such cases, the abundance of the mineral in question can serve as an additional tool for differentiation, as minerals with abundances of more than approximately 10 percent by volume are unlikely to be intercumulus in origin.

In a few cases olivine is rimmed by amphibole (Figure 4.6F, H). As the rims tend to be localised phenomena, they are interpreted to represent interstitial liquid rather than reaction products between olivine and neighbouring minerals. The amphibole rims are more common in leucocratic rocks, possibly suggesting that zones A and C are enriched in interstitial liquid. In addition, in samples that contain amphibole rims, some of them (e.g., in samples RM16, RM20, RM19, LR03, RM32, RM3, RM12) contain olivine that is partially surrounded by a wormy intergrowth of magnetite and hypersthene (collectively termed oxysymplectite) (Figure 4.6H). Oxysymplectites have been interpreted to form as a result of olivine reacting with interstitial liquid via the reactions  $\text{fayalite} + \text{O}_2 \rightarrow \text{magnetite}$ , and  $\text{forsterite} + \text{quartz} \rightarrow \text{enstatite}$  (Morse 2015).

In rare cases one can observe the development of a fan-shaped reaction rim or 'corona' around olivine. Figure 4.6F shows that the feature only occurs at the olivine-plagioclase contact, and that when olivine is rimmed by amphibole this reaction rim is absent. The corona therefore probably represents a subsolidus reaction between olivine and plagioclase.

### *Clinopyroxene*

Clinopyroxene typically forms subhedral or anhedral crystals. Grain sizes are variable; cumulus grains within Zone B are equant and typically 0.5-2 mm in size (Figure 4.7A) whereas interstitial grains in zones A and C – interpreted to be of intercumulus origin (Figure 4.7B) – can be up to 8 mm in size. Clinopyroxene typically contains fine lamellae of Fe-Ti oxide (Figure 4.7A). Such lamellae are more pronounced in samples that contain a high proportion of Fe-Ti oxide minerals (i.e., samples from the lower portion of Zone B). In rare cases, clinopyroxene contains small (0.2 mm) subrounded, grains of oxides (Figure 4.7C).

In some cases, intercumulus clinopyroxene in zones A and C is surrounded by thin rims of amphibole (Figure 4.7B). Similar to the amphibole rims surrounding olivine, these rims are interpreted to have crystallised from evolved (i.e., hydrous) interstitial liquid.

Clinopyroxene is typically unaltered, except in two samples: (1) the leuco-olivine-norite at the top of the intrusion (RM33; 4304 m), where grains of pyroxene may be altered to a fine-grained mass of clay minerals (Figure 4.7D); and (2) a leucogabbro in the centre of the intrusion (RM31; 2237 m), where many clinopyroxene crystals are partially replaced by amphibole.

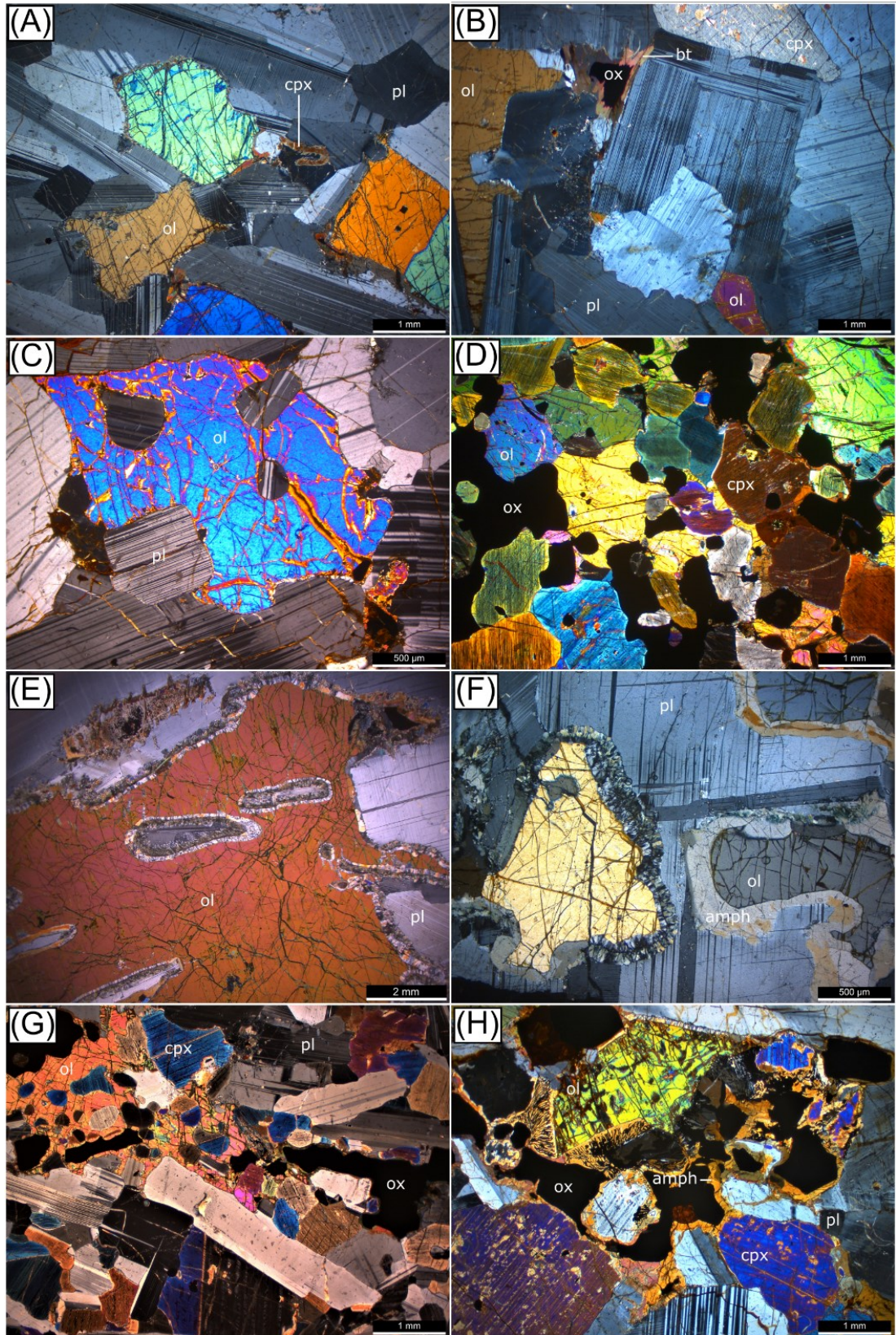


**Figure 4.6:** XPL photomicrographs displaying selected features of olivine. **(A)** Cumulus olivine in leuco-olivine-gabbro (RM16; Zone A; 439 m). **(B)** Wedge-shaped intercumulus olivine in

leuco-olivine-gabbro (RM12; Zone C; 3815 m). **(C)** Cumulus olivine hosting subrounded inclusions of plagioclase in gabbro (RM13; Zone B; 1217 m). **(D)** Cumulus olivine in wehrlite hosting subrounded blebs of oxide (PM4; Zone B; 917 m). **(E)** Large olivine oikocryst in troctolite (RM11; Zone C; 4073 m). **(F)** Thick amphibole rim surrounding olivine in leuco-olivine-gabbro (RM22; Zone A; 471 m). **(G)** Anhedral mass of olivine in mela-olivine-gabbro. Olivine grain forms extensions into interstitial space and contains inclusions of clinopyroxene and oxide (RM26C; Zone B; 1806 m). **(H)** Oxysymplectite – comprising hypersthene and oxide – appears to invade olivine in olivine gabbro (LR03; Zone B; 2122 m). Abbreviations: pl = plagioclase; ol = olivine; cpx = clinopyroxene; ox = oxide; amph = amphibole; bt = biotite.

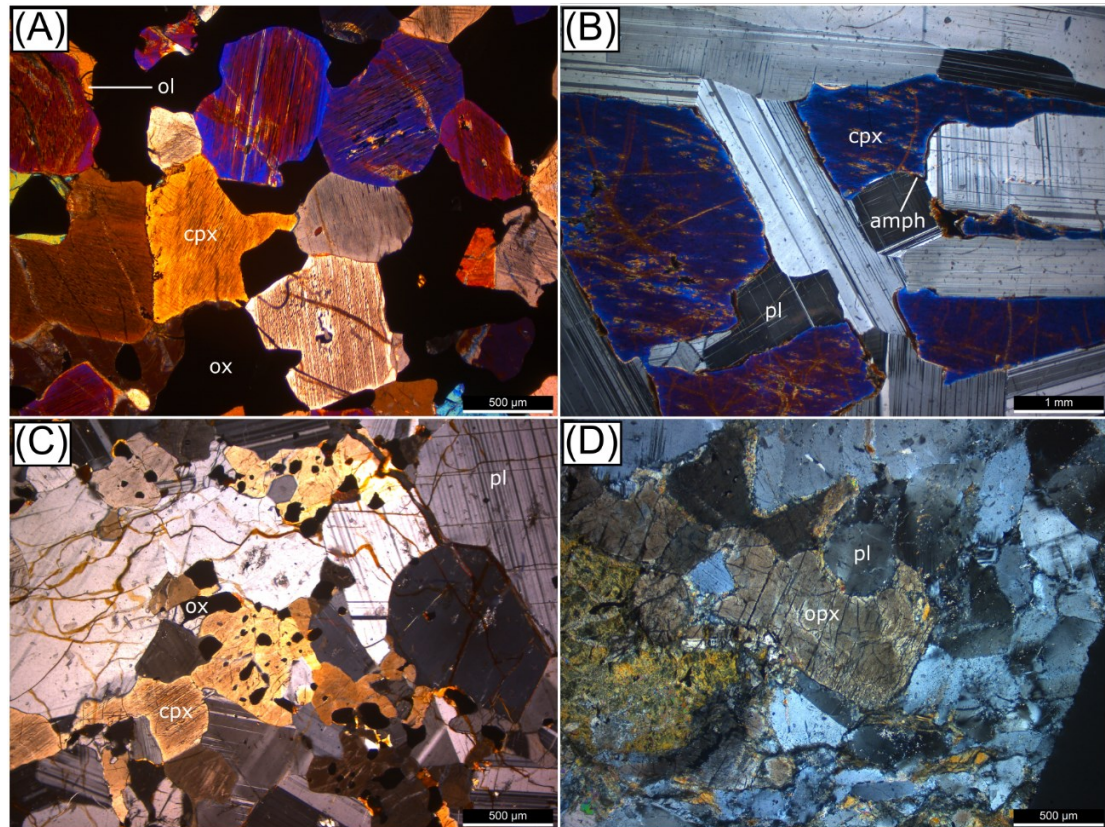


**Figure 4.7:** XPL photomicrographs showing key features of clinopyroxene (A, B, and C) and orthopyroxene (D). **(A)** Cumulus clinopyroxene forming equant grains in oxide-rich wehrlite (RM6; Zone B; 922 m). **(B)** Interstitial crystals of clinopyroxene in leuco-olivine-gabbro (RM20; Zone A; 160 m). **(C)** Clinopyroxene hosting rounded oxide grains in gabbro (RM13; Zone B; 1217 m). **(D)** Cumulus grain of orthopyroxene in leuco-olivine-norite, some of which is altered (RM33; Zone C; 4304 m). Abbreviations: pl = plagioclase; ol = olivine; cpx = clinopyroxene; ox = oxide; opx = orthopyroxene.

### *Orthopyroxene*

Orthopyroxene is a relatively rare mineral in the studied intrusion. In most samples it is restricted to oxysymplectites (Figure 4.6H), as well as rims around clinopyroxene (RM16, RM20, RM32, RM19).

Broadly equant grains of orthopyroxene, interpreted to be of cumulus origin, have only been identified in one leuco-olivine-norite at the top of the intrusion (Figure 4.7D) where they form subhedral grains with a typical grain size of ~1 mm. The grains are variably altered, being locally partially replaced by a fine-grained assemblage likely consisting of chlorite and hornblende.

#### **4.2.2 Description of the Fe-Ti oxides**

The main Fe-Ti oxides are magnetite and ilmenite, and they are present as both cumulus (Figure 4.8A, B) and intercumulus phases (Figure 4.8C, D). When they are cumulus phases, they form either isolated subhedral to anhedral grains in oxide-poor samples (<20 % oxides) (Figure 4.8A) or interconnected networks in oxide-rich samples (>20% oxides) (Figure 4.8B). The interstitial appearance of net-textured cumulus oxides in oxide-rich samples can be accounted for by a process of subsolidus grain boundary adjustment whereby cumulus Fe-Ti oxides locally become mobilised (Duchesne 1999).

Ilmenite formed both by primary (crystallisation) and secondary (exsolution) processes. Primary ilmenite grains have broadly equant granular shapes, of similar size to magnetite, and are interpreted to have co-crystallised with magnetite (Figure 4.9A). They occasionally contain thin (<10 µm) exsolution lamellae of hematite that form in two planes of the host mineral's crystal lattice at ~80° to one another (Figure 4.9B).

Secondary ilmenite formed as a result of oxy-exsolution from Ti-rich magnetite (Buddington and Lindsley 1964). Three discrete subtypes of exsolved ilmenite are recognized: (1) granular exsolutions, forming broadly equant grains resembling primary magmatic ilmenite (Figure 4.9C); (2) trellis-type exsolutions of thin (<10 µm) ilmenite lamellae, forming at ~110° angles to one another (Figure 4.9D) (Haggerty 1976); and (3) sandwich-type exsolutions of thick (~20 µm) ilmenite lamellae, forming in one plane of the magnetite crystal lattice (Figure 4.9E) (Haggerty 1976).

Magnetite also hosts ulvöspinel exsolutions which typically form fine-grained ( $\ll 1 \mu\text{m}$ ), cloth-textured intergrowths within magnetite (Figure 4.9F) (Ramdohr 1953). Ulvöspinel intergrowths are more commonplace in oxide-rich samples ( $\geq 20\%$  Fe-Ti oxides), which are mainly found in the lower portion of Zone B.

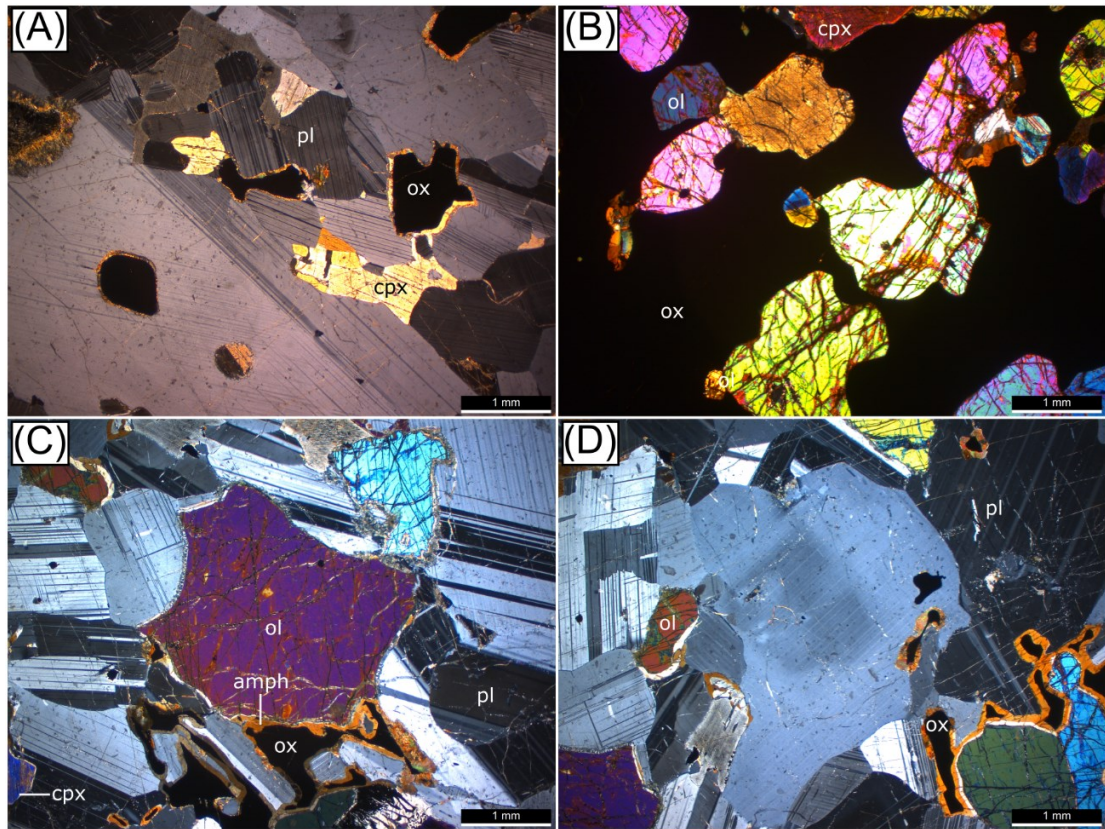


**Figure 4.8:** XPL photomicrographs showing key features of the oxides. **(A)** Isolated rounded grains of cumulus oxide in leucogabbro (RM19; Zone B; 2007 m). **(B)** Net-textured cumulus oxide in wehrlite from the mineralized zone (PM6; Zone B; 1143 m). **(C)** and **(D)** Intercumulus oxide with rims of amphibole in oxide-poor leuco-olivine-gabbro (RM16; Zone A; 439 m). Abbreviations: pl = plagioclase; ol = olivine; cpx = clinopyroxene; ox = oxide; amph = amphibole.

Mg-bearing hercynite is an accessory mineral, typically constituting  $<1\%$  of the oxide assemblage in oxide-poor samples, and up to  $4\%$  in oxide-rich samples. It is bright green in transmitted light and dark grey in reflected light. Three types of hercynite are recognized: (1) granular hercynite ( $200 \mu\text{m}$ ) in magnetite (Figure 4.9D; Figure 4.10A); (2) granular/lamellar hercynite ( $<50 \mu\text{m}$ -thick) hosted in lamellar or granular ilmenite exsolutions at/near the border

with magnetite (Figure 4.9G; Figure 4.10B, C, D); (3) intergrowths of very fine lamellae of hercynite in magnetite (Figure 4.9H; Figure 4.10D). These bear a similarity to cloth-textured ulvöspinel intergrowths, however hercynite intergrowths can be distinguished as they are typically disc-shaped, larger in size, darker in colour, and form at right angles to one another.

The abundance of hercynite intergrowths is inversely correlated with the abundance of cloth-textured ulvöspinel intergrowths. Consequently, hercynite lamellae are less common in the oxide-rich samples in the mineralized zone towards the base of Zone B (Figure 4.9F).

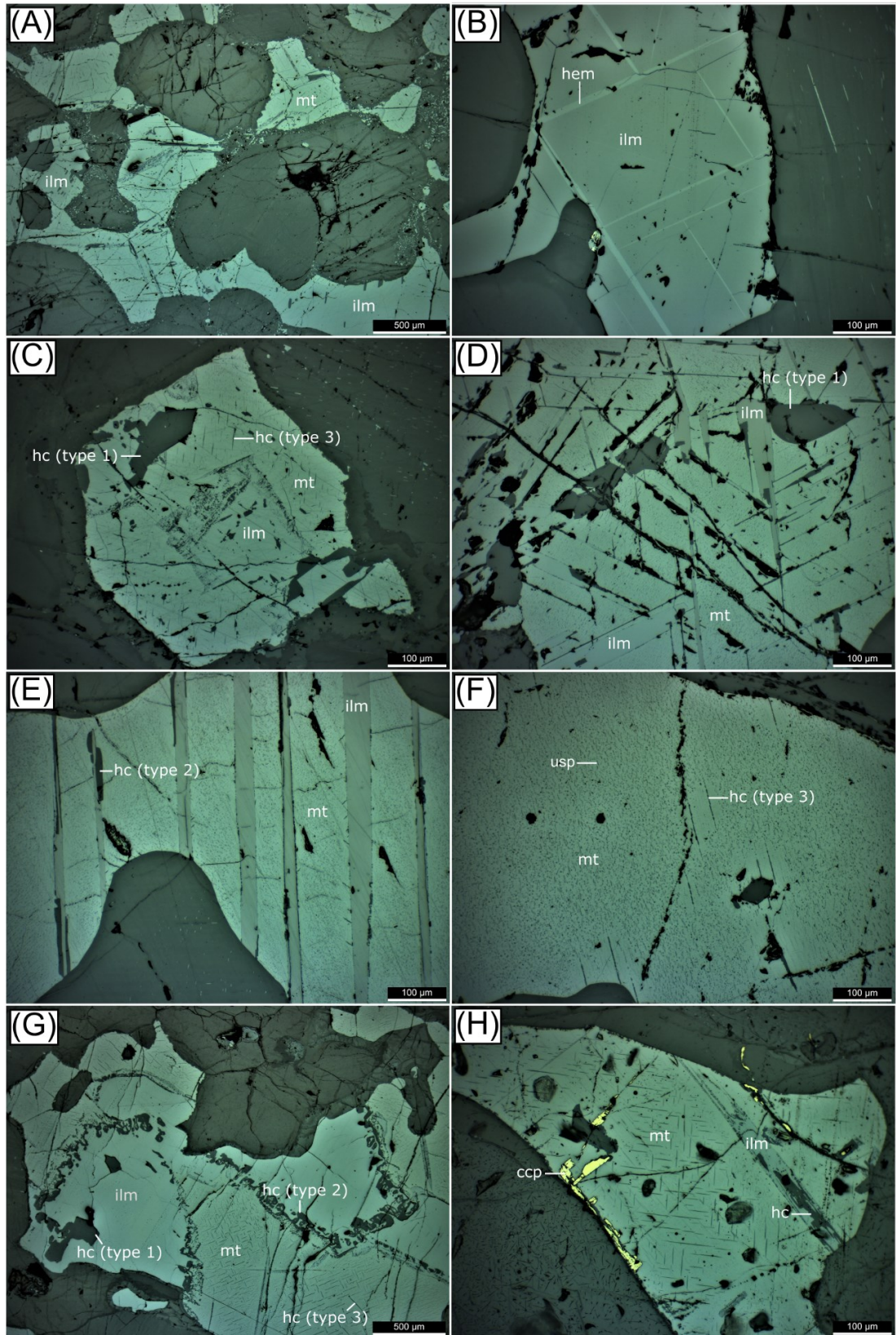


**Figure 4.9:** Reflected light photomicrographs displaying the key textural characteristics of the oxides. **(A)** Net-textured assemblage of co-crystallised magnetite and ilmenite in olivine gabbro

(RM8; Zone B; 832 m). **(B)** Coarse granular ilmenite (primary) containing hematite exsolution lamellae (wehrlite; PM4; Zone B; 917 m). **(C)** Magnetite grain containing granular exsolutions of ilmenite and hercynite in its core (olivine gabbro from Zone B, RM8; 832 m). **(D)** Criss-crossing ( $\sim 110^\circ$ ) thin trellis-type and coarser sandwich-type ilmenite exsolutions in magnetite. Small granules of hercynite are also visible. Sample is a wehrlite (PM4; Zone B; 917 m). **(E)** Sandwich-type ilmenite lamellae in magnetite, some of which contain lamellar hercynite exsolutions at the contact with magnetite (wehrlite; RM6; Zone B; 922 m). **(F)** Magnetite containing a large number of fine, cloth-textured ulvöspinel exsolutions and a zone of ulvöspinel-free magnetite surrounding hercynite exsolution lamellae in oxide-rich wehrlite (Zone B, PM4; 917 m). **(G)** Magnetite, hosting granular exsolutions of ilmenite, contains two types of hercynite (described in text). Type 1 is granular hercynite in magnetite (top-left). Type 2 is characterised by granular/lamellar hercynite at/near the magnetite contact within granular ilmenite. Type 3 is characterised by fine intergrowths of hercynite in magnetite (gabbro; RM13; Zone B; 1217 m). **(H)** Close-up highlighting type 3 hercynite. Here the intergrowths form slightly coarser, disc-shaped exsolutions compared with Zone B samples (wehrlite; RM23; Zone A; 674 m). Abbreviations: mt = magnetite; ilm = ilmenite; hc = hercynite; ccp = chalcopyrite; hem = hematite; usp = ulvöspinel.

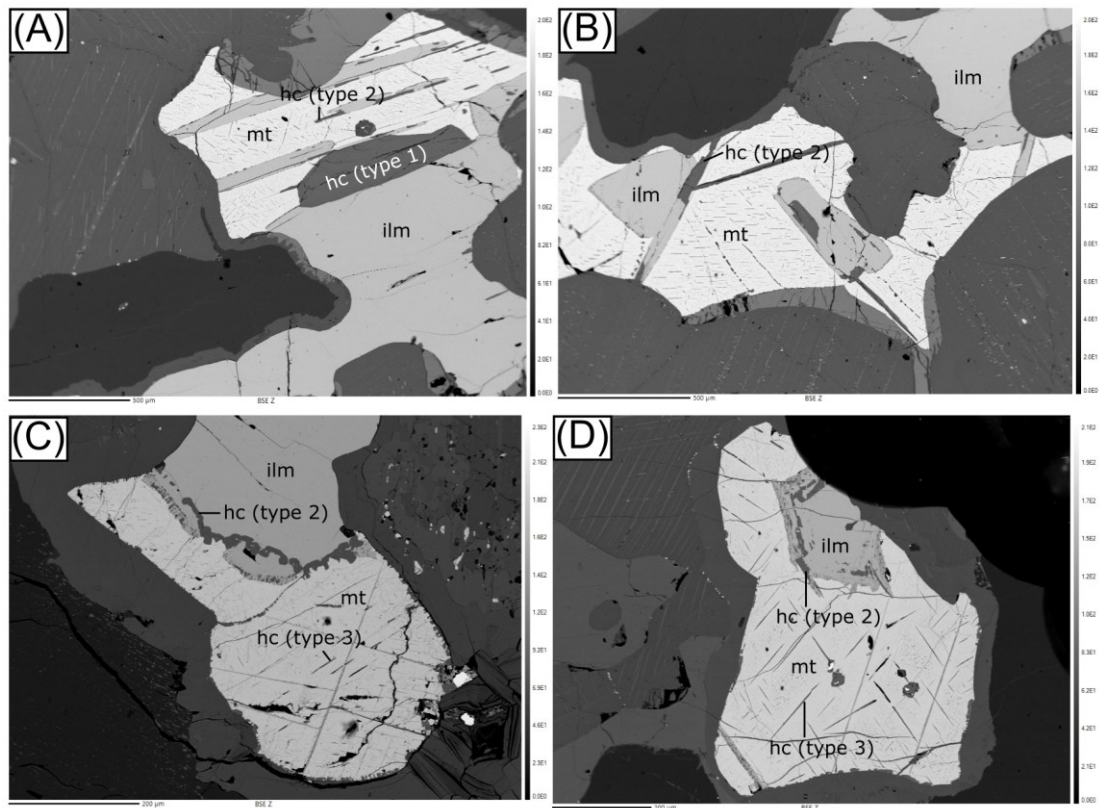


**Figure 4.10:** Back-scattered electron images, highlighting the three types of hercynite exsolution textures (see text for description) in Fe-Ti oxides from Zone B of the Étoile Suite. **(A)** Example of type 1 hercynite, characterised by a large ( $\sim 500 \mu\text{m}$ ) grain of granular hercynite in magnetite. Type 2 hercynite lamellae in sandwich-type ilmenite lamellae also visible (mela-olivine-gabbro; RM17; Zone B; 1585 m). **(B)** Type 2 hercynite (granular/lamellar hercynite in ilmenite at/near the magnetite contact) on the left (mela-olivine-gabbro; RM17; Zone B; 1585 m). **(C)** Coarse granular ilmenite (primary in origin) in contact with magnetite. Contact is marked by a chain of fine granular hercynite exsolutions. A second chain of coarser granular hercynite within ilmenite may mark the former border between the ilmenite and magnetite. The two chains

represent type 2 hercynite. Type 3 hercynite (hercynite intergrowths) also visible within the magnetite (gabbro; RM24; Zone B; 2813 m). **(D)** Multiple generations of type 2 hercynite at/near the border of secondary ilmenite granule. The ilmenite granule forms extensions into the host magnetite. Type 3 hercynite (hercynite intergrowths) also visible within the magnetite (leuco-gabbro; RM32; Zone B; 2752 m). Abbreviations: mt = magnetite; ilm = ilmenite; hc = hercynite.

#### **4.2.3 Description of the accessory minerals**

##### *Amphibole*

Brown amphibole (predominantly pargasite and Ti-rich pargasite, see Appendix 3) is a common accessory mineral and typically forms rims around oxides (Figure 4.11A) and, less commonly, around olivine and clinopyroxene (Figure 4.6F; Figure 4.7B). As stated above, rims surrounding mafic silicates are interpreted to represent the crystallisation products of interstitial liquid. In contrast, the ubiquitous rims surrounding Fe-Ti oxides may have formed due to reactions between the Fe-Ti oxides and silicates (mainly plagioclase). While it is possible that the amphibole rims surrounding Fe-Ti oxides also represent trapped liquid, they are much more ubiquitous, and are present even in samples that otherwise show little evidence for trapped liquid. In one relatively fine-grained sample (RM02; Zone B; 3544 m) amphibole forms euhedral or subhedral crystals that are possibly cumulus in origin (Figure 4.11B).

##### *Biotite*

Brown biotite is most common in leucocratic lithologies where it can make up to ~2 % of the rock (Figure 4.11C). The mineral tends to be associated with amphibole rims, specifically in samples where the amphibole is interpreted to have crystallised from interstitial liquid.

##### *Apatite*

(Fluoro)Apatite is a rare mineral observed in only three sample, where it is typically euhedral and hexagonal in shape, with a grain size of up to ~1 mm (Figure 4.11D). Two of the

samples (RM15; 54 m and RM29; 1861 m) are gabbroic pegmatites which formed from fluid/volatile-rich pockets of evolved residual liquid. Sample RM20 (160 m) is a coarse-grained leuco-olivine-gabbro cumulate from Zone A and occurs with interstitial clinopyroxene that crystallised from trapped liquid.

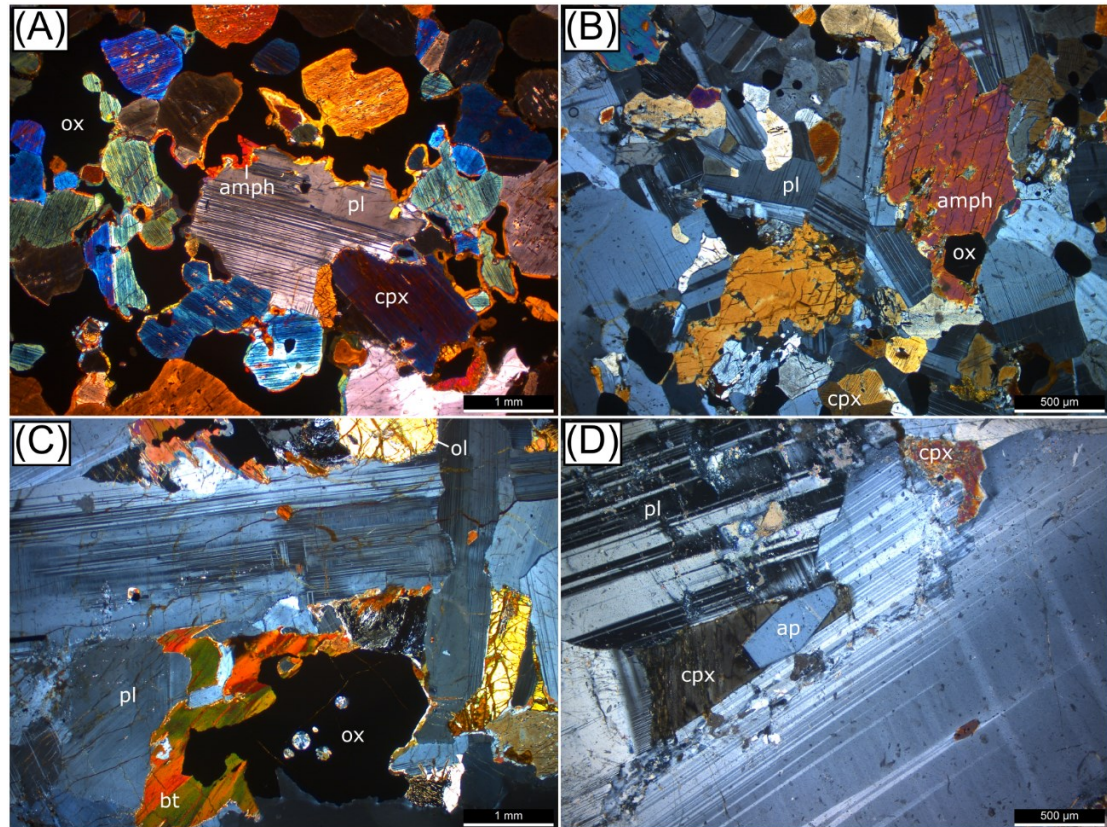


**Figure 4.11:** XPL photomicrographs highlighting key features of amphibole, biotite and apatite. **(A)** Reaction-type amphibole rims surrounding Fe-Ti oxides. Rims occur more commonly where Fe-Ti oxides are in contact with plagioclase, and less commonly where in contact with clinopyroxene (LR06; oxide-rich wehrlite, Zone B; 1073 m). **(B)** Euhedral to subhedral amphibole grains in gabbro (RM02; Zone B; 3544 m). **(C)** Biotite partially surrounding Fe-Ti oxide grain in leuco-olivine-gabbro (RM12; Zone C; 3815 m). **(D)** Hexagonal apatite crystal hosted by intercumulus clinopyroxene in leuco-olivine-gabbro (RM20; Zone A; 160 m). Abbreviations: pl = plagioclase; ol = olivine; cpx = clinopyroxene; ox = oxide; amph = amphibole; bt = biotite; ap = apatite.

### *Sulphides*

Sulphides are present in trace proportions (<0.1 %) in most samples, but can reach proportions of up to several percent in the Fe-Ti oxide-mineralized zone. They are typically 0.1-0.5 mm in size and form anhedral grains filling the interstices between silicate and oxide

minerals (Figure 4.12A). However, in some samples, the sulphides form rounded blebs (Figure 4.12B). The most common sulphide mineral is pyrrhotite, with chalcopyrite, pentlandite, and pyrite being less common. Pyrrhotite and chalcopyrite are present throughout the intrusion whereas pentlandite is only present in zones A and C, as well as the lowermost samples of Zone B (i.e., the Fe-Ti oxide-mineralized zone). Pyrite is largely restricted to the centre of the intrusion.

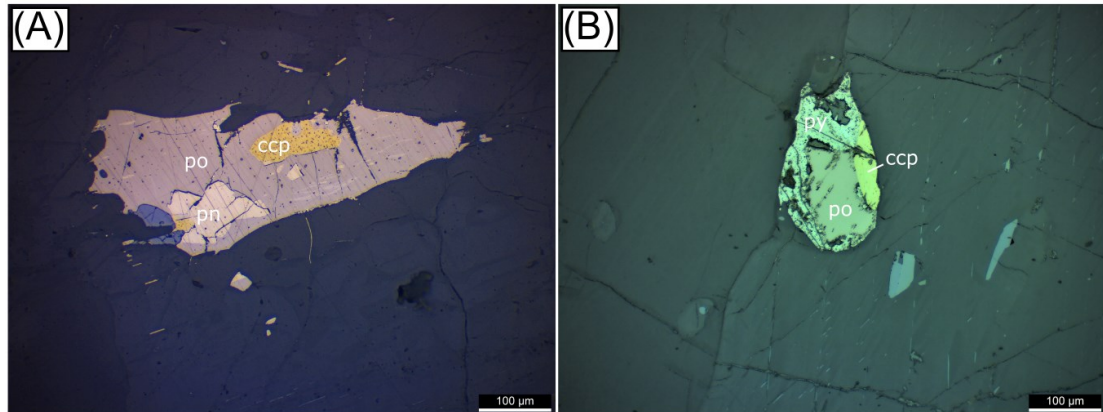


**Figure 4.12:** Photomicrographs of sulphides. **(A)** Magmatic sulphide assemblage of pyrrhotite containing pentlandite exsolution flames, as well as subordinate chalcopyrite and granular pentlandite (RM11, troctolite; Zone C; 4073 m). **(B)** Weak alteration of composite bleb-like sulphide containing pyrrhotite and chalcopyrite to a fine-grained pyrite-marcasite assemblage (RM17; mela-olivine-gabbro; Zone C; 1585 m). Abbreviations: pn = pentlandite; po = pyrrhotite; ccp = chalcopyrite.

### 4.3 Element maps of selected samples

In order to highlight the textures and mineralogy of the mafic rocks from the Étoile Suite, SEM element maps of an ultramafic sample and a mafic sample from the lower portion of Zone B are presented below. The two samples are: an oxide-rich (approx. >20 %) wehrlite from the mineralized zone (RM6; 922 m), and a leucocratic oxide-bearing gabbro from just above the mineralized zone (RM13; 1217 m).

#### 4.3.1 Oxide-rich wehrlite

The medium-grained oxide-rich wehrlite (RM6, Figure 4.13) consists mainly of equigranular clinopyroxene (49.8 %), olivine (17.2 %), magnetite (20.7 %) and ilmenite (11.1 %), and a small amount of hercynite (0.77 %). The ratio of magnetite to ilmenite is thus approximately 2:1. Granular hercynite is fairly evenly distributed throughout the sample, occurring almost exclusively within magnetite. Magnetite contains sandwich-type ilmenite lamellae. Accessory minerals include sulphides (pyrrhotite, pentlandite, chalcopyrite), phlogopite, and apatite. Sulphides are heterogeneously distributed and there are domains which are essentially sulphide free. Plagioclase, chromite, quartz, K-feldspar and zircon are absent.

An enlarged element map (Figure 4.14) reveals small-scale exsolution features in magnetite that are not visible in the large-scale element map. Two types of hercynite (type 2 and type 3; described in Chapter 4.2.2) are visible. The map shows that the concentration of ulvöspinel intergrowths is relatively high in this sample, and that the distribution of ulvöspinel is not homogenous. Progressively less ulvöspinel is present towards the contact with ilmenite, and there is a domain with a ~10 µm radius around the disc-shaped hercynite intergrowths that is relatively free of ulvöspinel.

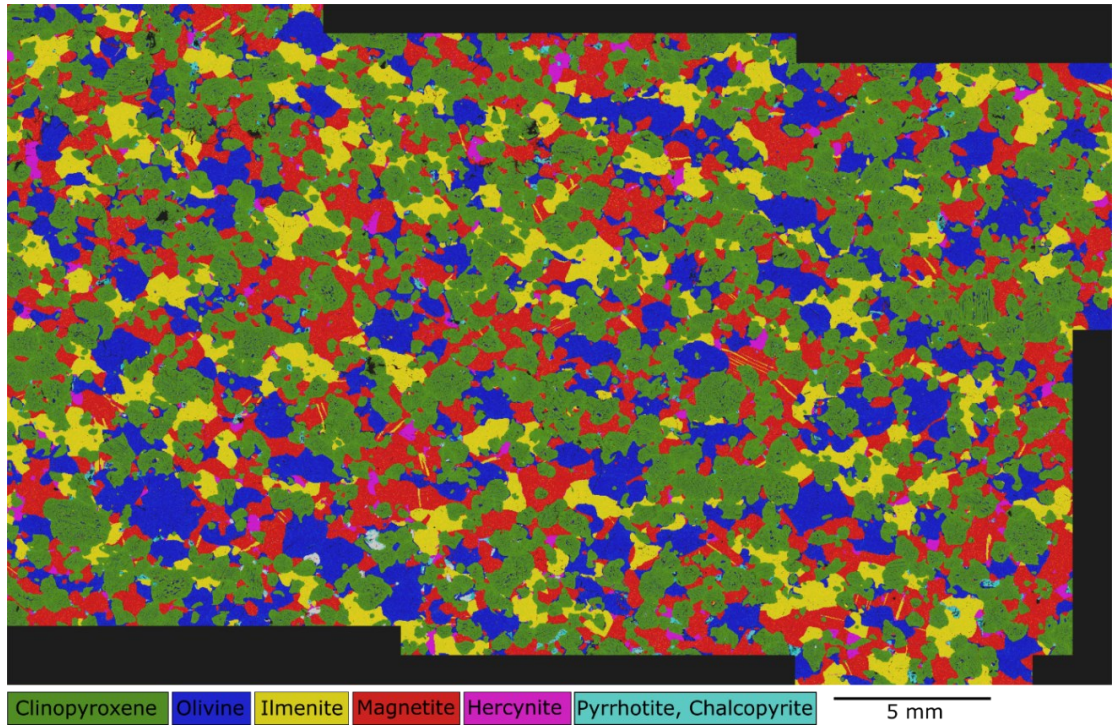


**Figure 4.13:** SEM map of the oxide-rich wehrlite. Note the interstitial nature of the oxides, the faint modal layering and the sandwich-type ilmenite exsolutions in magnetite (RM6; Zone B; 922 m).

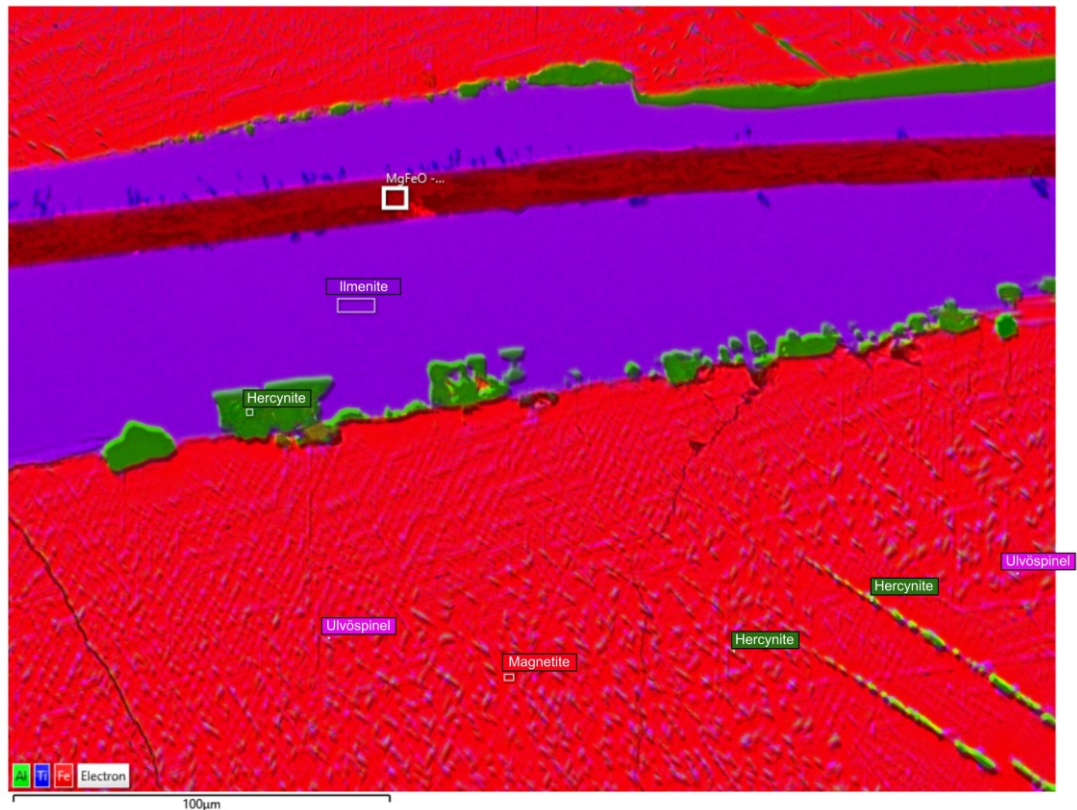


**Figure 4.14:** Detailed SEM map revealing exsolution of ulvöspinel (pink) and hercynite (green) in magnetite (red) within oxide-rich wehrlite (RM6; 922 m). Relatively coarse (~70 µm-wide) ilmenite (purple) sandwich lamella hosts type 2 granular hercynite (10 µm) at the contact with magnetite. Magnetite also contains very fine ilmenite and ulvöspinel intergrowths that become smaller towards the border with ilmenite. Hercynite also forms disc-shaped exsolution along one plane of the magnetite crystal lattice, around which exists a zone depleted in ulvöspinel intergrowths.

#### 4.3.2 Oxide-bearing gabbro

Sample RM13 also comes from the lower portion of Zone B, but in contrast to most other samples from this subzone, it contains a substantial amount of plagioclase. The rock is a medium-grained oxide-bearing gabbro, consisting mainly of plagioclase (50.8 %) and clinopyroxene (36.2 %) with minor olivine (2.2 %), magnetite (5.1 %) and ilmenite (5.2 %). The proportion of olivine to clinopyroxene is thus lower than in the oxide-rich wehrlite. Notably, this sample contains a ~1:1 ratio of magnetite and ilmenite. Hercynite (0.5 %) occurs preferentially within oxides but in contrast to sample RM6, hercynite does not appear to show a strong

preference for magnetite – a significant amount of hercynite occurs within ilmenite as well. Accessory minerals include sulphides (pyrrhotite, pentlandite, chalcopyrite), biotite, and apatite. There is no chromite, quartz, K-feldspar or zircon.

In contrast to the homogenous texture of the oxide-rich wehrlite, this sample is varitextured, with some areas being significantly coarser grained than others. The coarse-grained portion is characterised by a prominent layer of clinopyroxene, magnetite and ilmenite running through the middle of the sample. Finer-grained domains are scattered throughout the sample (Figure 4.15). The clinopyroxene-, magnetite-, and ilmenite-rich layer highlights the previously mentioned preferred association between the oxides and the mafic silicates. The association is further evidenced by the presence of plagioclase-only domains that are essentially free of oxides. This sample also displays the presence of olivine rims surrounding oxides – a feature not seen in sample RM16. Figure 4.16 shows an enlargement of the finer-grained part of the slide, illustrating the presence of numerous small, subrounded oxide grains within clinopyroxene and, to a lesser degree, plagioclase. The inclusions consist largely of pure magnetite.

A high-resolution element map of part of the sample displays some of the exsolution textures in detail (Figure 4.17). The main features are: (1) the near absence of cloth-textured ulvöspinel compared to the oxide-rich wehrlite; (2) the high abundance of hercynite compared to the oxide-rich wehrlite; (3) the reduced amount of type 3 hercynite (hercynite intergrowths) in the vicinity of type 1 hercynite (granular hercynite in magnetite), as well as the sandwich-type ilmenite lamella; (4) the somewhat different appearance of type 3 hercynite (hercynite intergrowths), which, in this sample, is characterised by hercynite lamellae in two planes of the magnetite crystal lattice rather than only one plane.

In sum, there are less ulvöspinel exsolutions, and more hercynite grains in the gabbroic sample (RM13) compared to the ultramafic sample (RM6). The higher abundance of ulvöspinel in RM6 probably reflects higher  $\text{TiO}_2$  in magnetite contents than in RM13. The magnetite:ilmenite ratio in RM6 is higher (2:1) than in RM13 (1:1). Either low proportions of

ilmenite crystallisation in RM6 facilitated higher uptake of  $\text{TiO}_2$  in co-crystallising magnetite, or higher degrees of ilmenite exsolution in RM13 have left magnetites depleted in  $\text{TiO}_2$ .

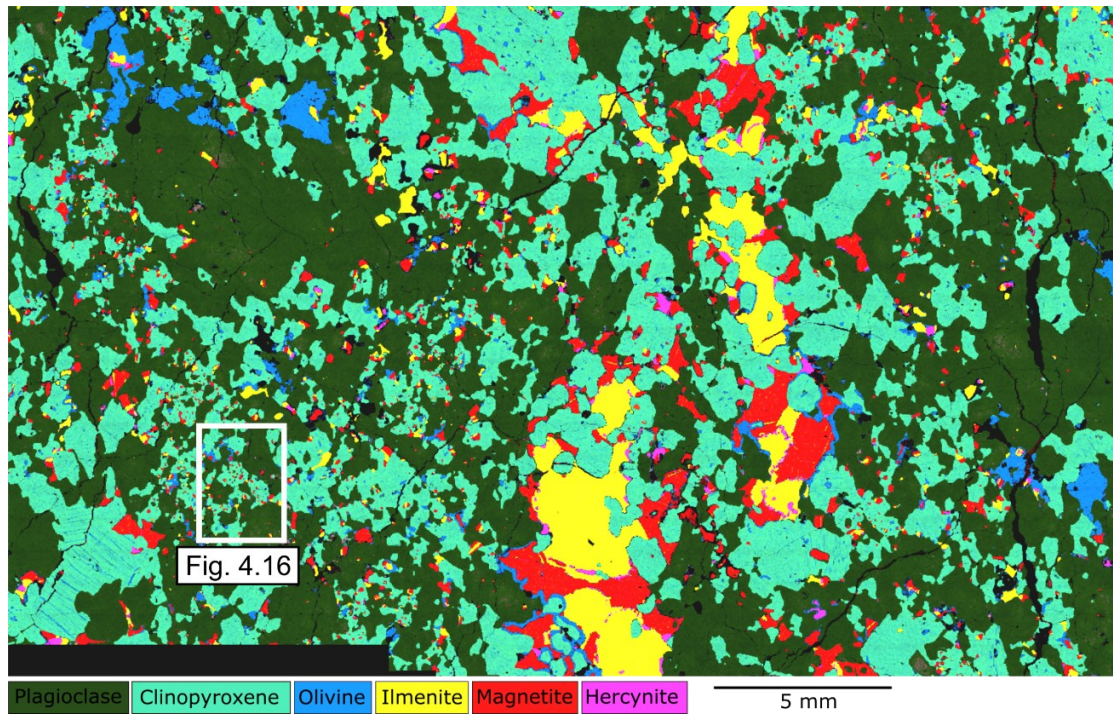


**Figure 4.15:** SEM map of the oxide-bearing gabbro. Note the close association between oxides and clinopyroxene. Plagioclase, on the other hand, is relatively free of oxides. Olivine commonly forms rims around oxide minerals (RM13; Zone B; 1217 m).

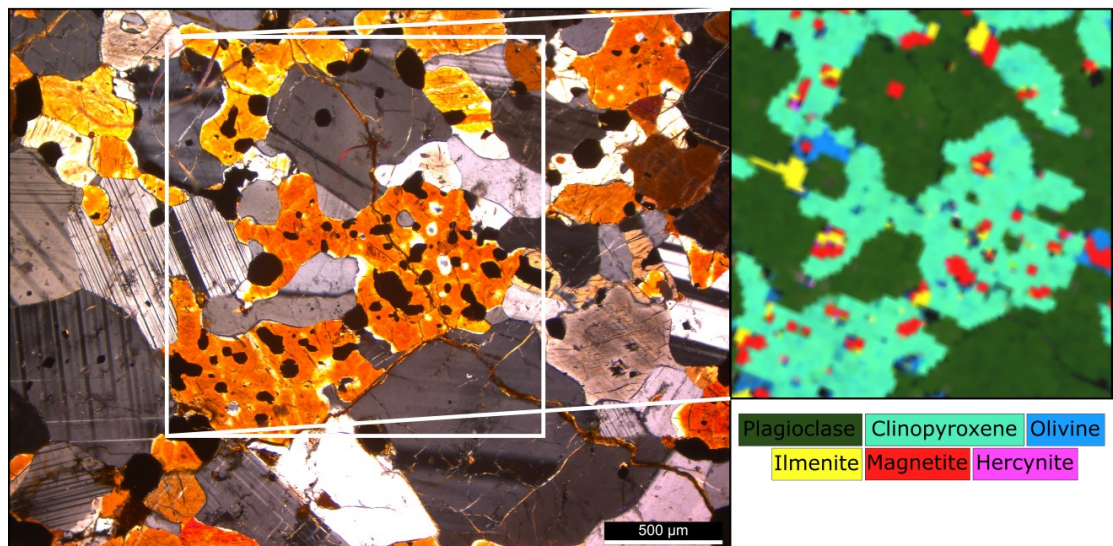


**Figure 4.16:** Close-up of a fine-grained portion of sample RM13, showing small rounded oxides of predominantly magnetite and minor ilmenite in clinopyroxene.

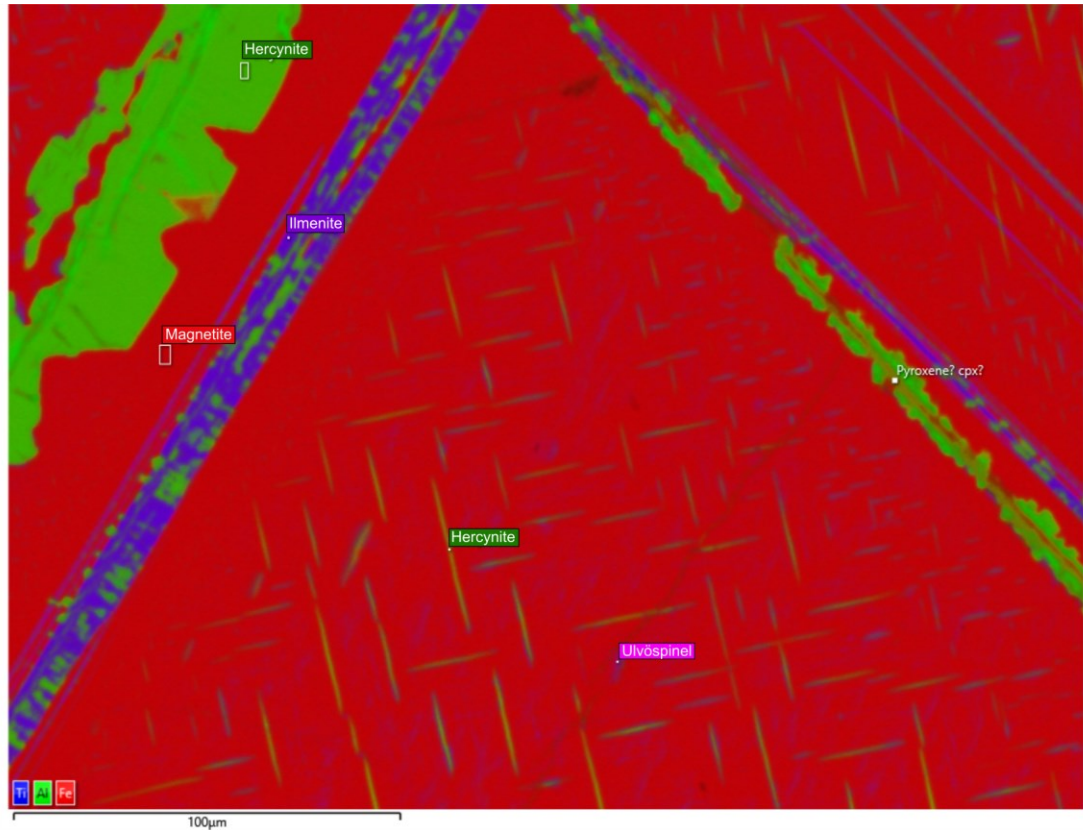


**Figure 4.17:** High-resolution element map of a magnetite grain in RM13. The grain contains ilmenite exsolution lamellae and two types of hercynite, namely granular hercynite (top-left), and disc-shaped hercynite (centre). The latter forms intergrowths in two directions, at right angles to one another. Note the near absence of cloth-textured ulvöspinel, especially in proximity to the granular hercynite.

#### 4.4 Whole-rock concentrations of the major elements

Based on the petrographic observations presented in Chapter 4.2.1, the mafic samples from the Étoile Suite are a mixture of Fe-Ti oxides and silicates. Therefore, plots of SiO<sub>2</sub> vs. other elements provide information on the composition of the Fe-Ti oxide component (Figure 4.18). The concentration of SiO<sub>2</sub> in the rocks ranges between 15.5 and 53.2 wt. %, TiO<sub>2</sub> between 0.38 and 14.4 wt. %, Al<sub>2</sub>O<sub>3</sub> between 13.6 and 21.2 wt. %, FeO<sub>(total)</sub> between 5.88 and 53.2 wt. %, MnO between 0.09 and 0.35 wt. %, MgO between 2.05 and 11.5 wt. %, CaO between 2.97 and 11.7 wt. %, Na<sub>2</sub>O between 0.25 and 5 wt. %, K<sub>2</sub>O between 0 and 0.61 wt. %, and P<sub>2</sub>O<sub>5</sub> between 0 and 0.19 wt. %. The complete data are listed in Appendix 2.

The samples form two clusters in the binary variation diagrams: (1) a high-silica (>42.9 wt. %) cluster enriched in  $\text{Al}_2\text{O}_3$ ,  $\text{Na}_2\text{O}$ ,  $\text{K}_2\text{O}$  and  $\text{P}_2\text{O}_5$ ; and (2) a low-silica cluster (<37.2 wt. %) enriched in  $\text{TiO}_2$ ,  $\text{Fe}_2\text{O}_3$ ,  $\text{FeO}_{(\text{total})}$ ,  $\text{MnO}$ , and  $\text{V}_2\text{O}_3$  (Figure 4.18). The high-silica cluster consists primarily of oxide-poor (leucocratic) rocks with more than 35 % plagioclase by volume, whereas the low-silica group consists primarily of oxide-rich melanocratic to ultramafic rocks with less than 35 % plagioclase by volume (Figure 4.19). Stratigraphically, the high-silica rocks are restricted to Zone A, the upper portion of Zone B, and Zone C. The low-silica rocks occur predominantly in the lower portion of Zone B.

The major and minor element oxides are controlled by the proportions of the main rock-forming minerals plagioclase, clinopyroxene, olivine, magnetite and ilmenite, which explains the trends in the binary variation diagrams. The low-silica group is enriched in elements hosted predominantly by the Fe-Ti oxide minerals (Ti, Fe, Mn, V), and to a lesser degree olivine (Mg), whereas the high-silica group is enriched in elements hosted mainly by plagioclase (Al, Ca, Na, K) and clinopyroxene (Ca).

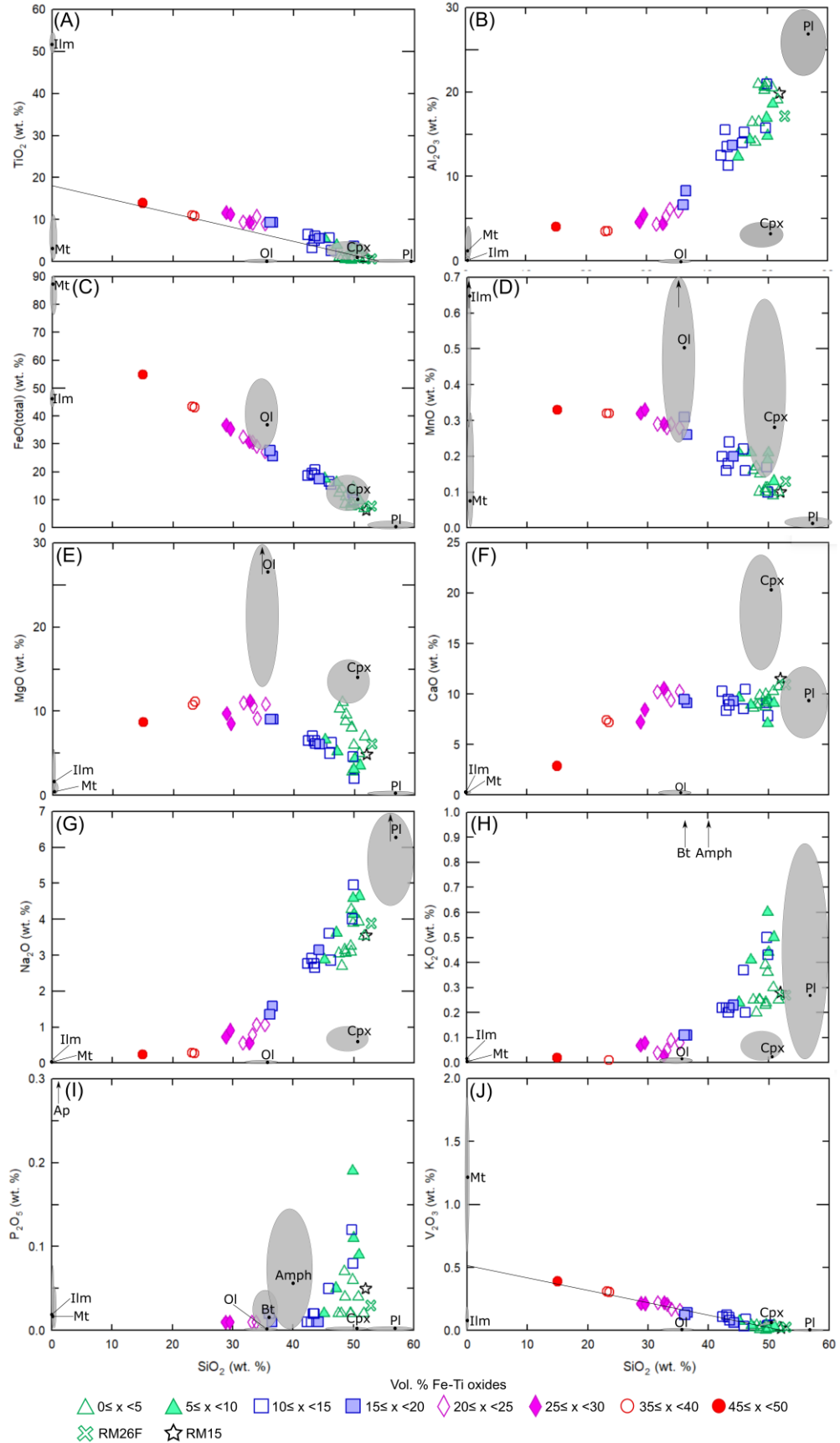


**Figure 4.18:** Bivariate diagrams displaying whole-rock data for the mafic part of the Étoile Suite. SiO<sub>2</sub> is plotted against TiO<sub>2</sub> (A), Al<sub>2</sub>O<sub>3</sub> (B), FeO<sub>(total)</sub> (C), MnO (D), MgO (E), CaO (F), Na<sub>2</sub>O (G), K<sub>2</sub>O (H) and P<sub>2</sub>O<sub>5</sub> (I), V<sub>2</sub>O<sub>3</sub> (J). Mineral compositions are plotted using electron microprobe data (this study).

Note that there is a significant amount of scatter for the leucocratic high-silica samples in the SiO<sub>2</sub> vs. K<sub>2</sub>O and SiO<sub>2</sub> vs. P<sub>2</sub>O<sub>5</sub> plots. The scatter may be attributed to the presence of a liquid component that has crystallised to form amphibole, biotite, apatite and other trace phases, consistent with petrographic observations (Figure 4.6F; Figure 4.7B), meaning that many leucocratic samples are mesocumulates, whereas oxide-rich melanocratic samples are adcumulates.

In Figure 4.20 the concentrations of selected major element oxides are plotted as a function of stratigraphic height. MgO and Al<sub>2</sub>O<sub>3</sub> contents show considerable scatter without clear trends, although MgO appears to be slightly enriched in the lower portion of the intrusion. The elements FeO<sub>(total)</sub>, TiO<sub>2</sub> and V<sub>2</sub>O<sub>3</sub>, on the other hand, show a marked enrichment in the centre of the intrusion, notably in the lower portion of Zone B, reflecting the relatively high proportion of Fe-Ti oxides in and around the mineralized zone.

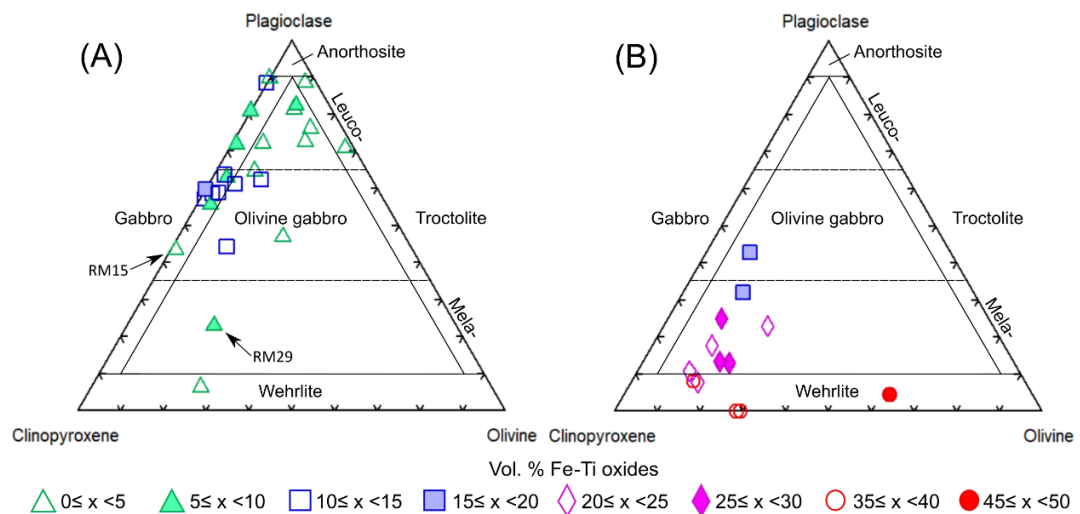


**Figure 4.19:** High-silica samples (A) and low-silica samples (B) plotted in the clinopyroxene-plagioclase-olivine ternary diagram of Streckeisen (1976).

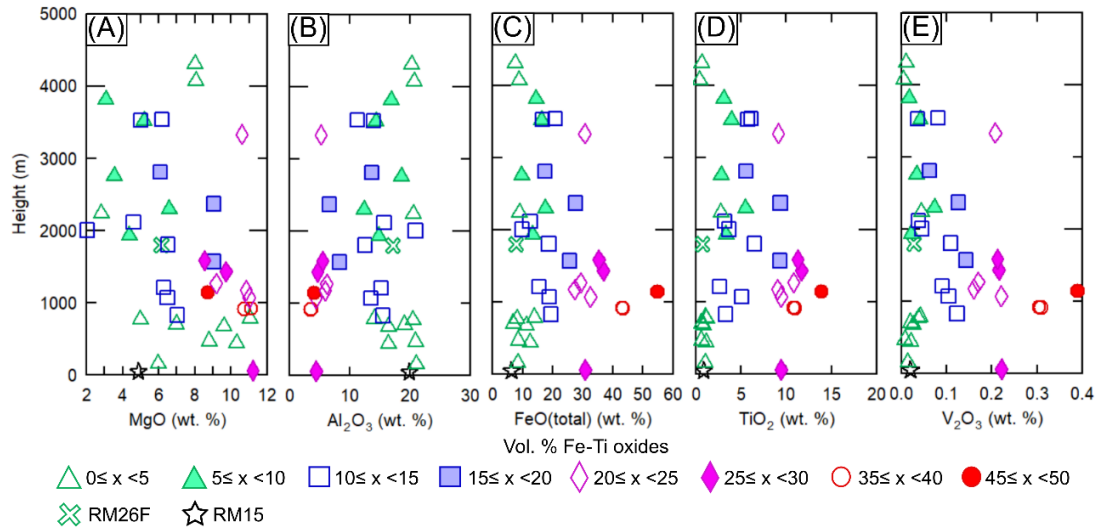


**Figure 4.20:** Whole-rock concentrations of MgO (A), Al<sub>2</sub>O<sub>3</sub> (B), FeO<sub>(total)</sub> (C), TiO<sub>2</sub> (D), V<sub>2</sub>O<sub>5</sub> (E) plotted as a function of stratigraphic height in the intrusion.

#### 4.5 Whole-rock concentrations of trace elements

Binary variation diagrams of selected trace elements plotted against SiO<sub>2</sub> are shown in Figure 4.21, and selected elements are plotted as a function of stratigraphic height in Figure 4.22.

Chromium and, to a lesser extent, Ni are relatively enriched in some samples of the leucocratic high-silica cluster, notably at ~50 % SiO<sub>2</sub>, which likely reflects control by clinopyroxene and olivine, respectively. Figure 4.22 clearly shows that only the leucocratic rocks (typically oxide- and clinopyroxene-poor) from Zone A and Zone C are enriched in Ni and Cr. In contrast, there is a strong depletion of Cr and Ni in Zone B, despite clinopyroxene and oxides being abundant (Figure 4.4).

Cobalt is enriched in the oxide-rich low-silica cluster of rocks. The element shows a good negative correlation with SiO<sub>2</sub> suggesting control by Fe-Ti oxides. Cobalt is compatible in magnetite, with a partition coefficient of 2-25 (mean 7.5, Dare et al. 2012). Considering that Ni and Cr are even more compatible into magnetite ( $D_{Ni} = 12-77$ , mean = 30;  $D_{Cr} = 19.3-340$ , mean = 67.4, Dare et al. 2012), the contrast between the trends of Co and Ni-Cr is somewhat puzzling. Perhaps the strong enrichment of Cr and Ni in the plagioclase-olivine and plagioclase-

olivine-clinopyroxene cumulates of Zone A (Figure 4.22) suggests that the effect of the silicates outweighs the effect of the Fe-Ti oxides with regard to Cr and Ni behaviour.

Copper is enriched in the oxide-rich low-silica group (Figure 4.21D). Figure 4.22D shows that Cu contents are generally low throughout the intrusion, with the exception of 4 samples occurring in a 311 m-thick interval at the base of Zone B (between RM8 at 832 m and PM6 at 1143 m) corresponding to the horizon of oxide mineralization. The increase of Cu in this interval is consistent with the appearance of cumulus sulphide, expressed by a sharp increase in Cu at this level (Figure 4.22D). The abrupt fall of Cu to ~40 ppm in the remainder of the intrusion suggests that the magma had become depleted in Cu, due to the high D values of Cu with regard to sulphide melt (~1000, Barnes et al. 1997).

Strontium is strongly correlated with Si content. Since Sr is compatible into plagioclase, it is controlled by the modal proportion of plagioclase in the rocks (Figure 4.21E). In Figure 4.22E, Sr shows a scattered distribution (analogous to  $Al_2O_3$ ) likely reflecting the highly variable proportion of plagioclase in the intrusion.

The highly incompatible elements Zr, La and Th are enriched in the high-silica cluster in the binary variation diagrams (Figure 4.21F, G, H). All three elements show an enrichment in several samples of the upper portion of the intrusion (Figure 4.22F, G, H). As such, abundances of these elements reflect the amount of highly evolved interstitial liquid (forming accessory apatite and zircon) within the cumulates.

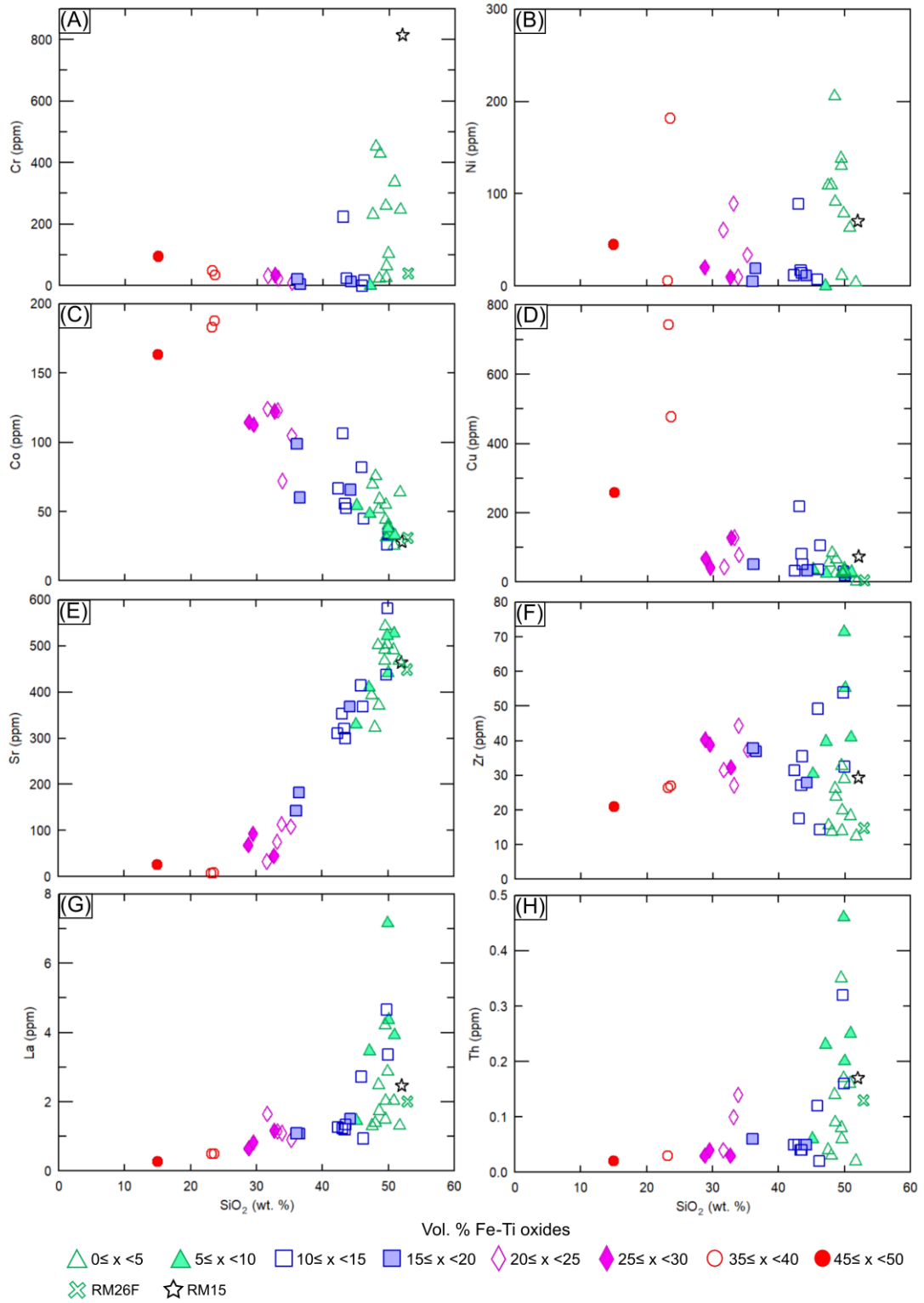


**Figure 4.21:** Whole-rock concentrations of SiO<sub>2</sub> vs. Cr (A), Ni (B), Co (C), Cu (D), Sr (E), Zr (F), La (G), Th (H). See text for details.

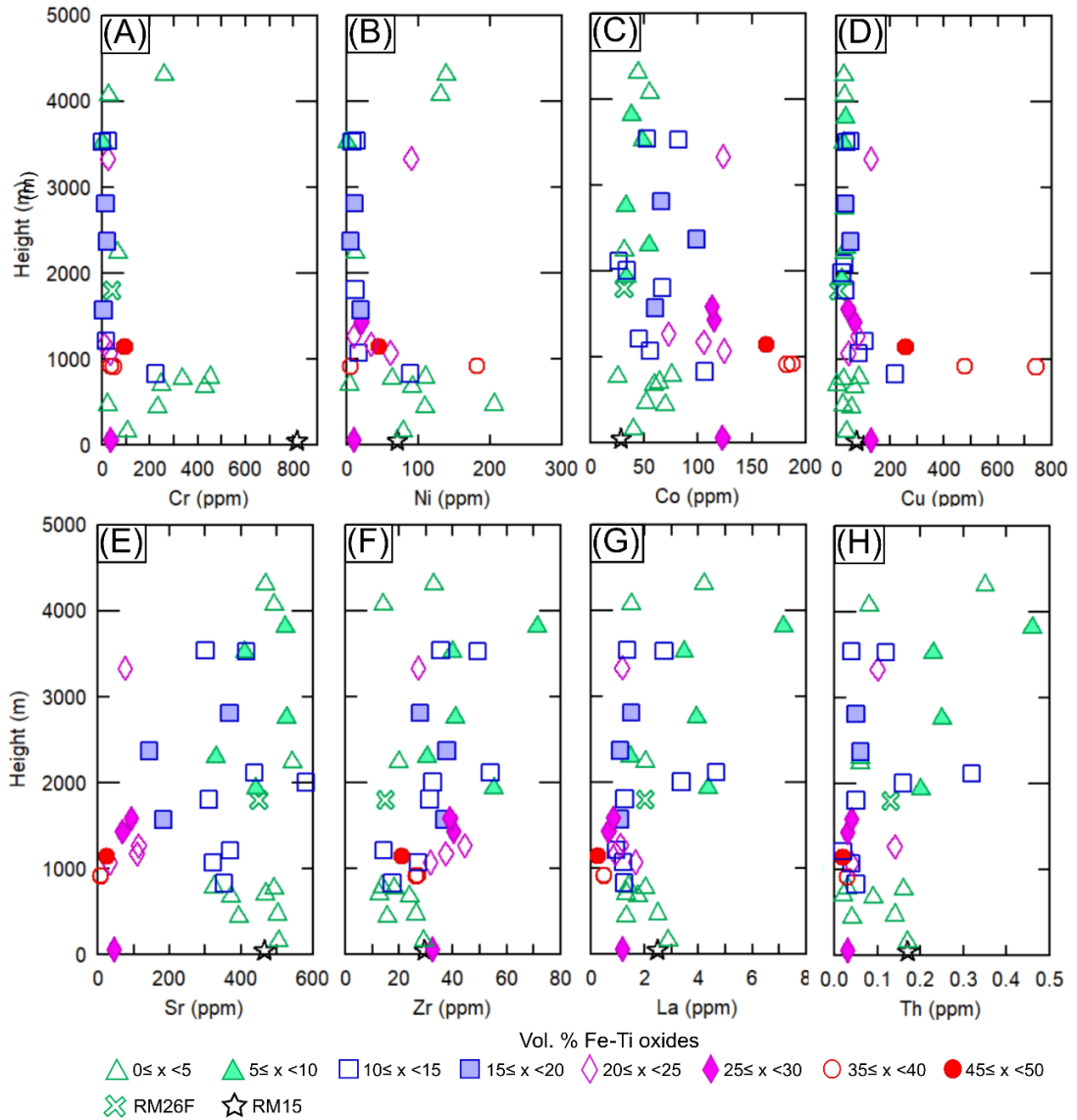


**Figure 4.22:** Whole-rock concentrations of Cr (A), Ni (B), Co (C), Cu (D), Sr (E), Zr (F), La (G), Th (H) as a function of stratigraphic height in the intrusion. See text for details.

Differences in the concentrations of trace elements between the oxide-poor high-silica, and oxide-rich low-silica groups can be further highlighted by plotting the samples in multi-element variation diagrams, normalised to primitive mantle (Figure 4.23).

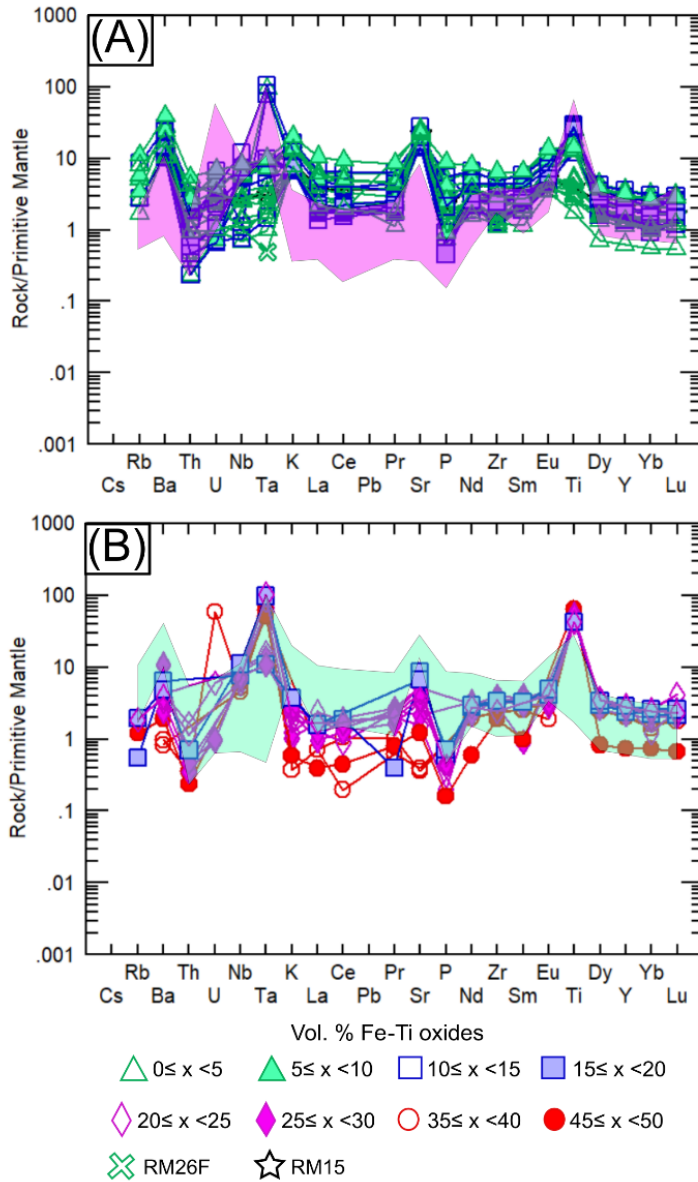


**Figure 4.23:** Multi-element variation diagrams showing signatures for high-silica samples **(A)** and low-silica samples **(B)** from the mafic part of Étoile Suite. Purple and green fields denote compositional range of low-silica and high-silica groups, respectively. RM26F = fine-grained enclave; RM15 = pegmatoidal gabbro. Note Pb is not plotted. Normalisation factors from Sun and McDonough (1989).

These plots show broad trends of relative enrichment of the most highly incompatible elements (on the left of the diagrams) relative to less incompatible elements (on the right of the diagrams). Figure 4.23A shows the patterns for the high-silica rocks, whereas Figure 4.23B shows the patterns for the low-silica rocks. It can be seen that Rb, Ba, Th, K, La, Ce, Pr, Sr, Nd, Zr, Sm, and Eu are relatively enriched in the silica-rich rocks, as expected due to the high

plagioclase and trapped liquid content of the leucocratic rocks. In contrast Nb, Ta, and Ti are relatively enriched in the silica-poor rocks, also as expected since these elements are hosted by ilmenite. Uranium, Dy, Y, Yb, Lu do not appear to be preferentially enriched in either group. In both groups there are marked positive anomalies in Ba and Sr (from plagioclase) and Ti and Ta (from ilmenite). In the high-silica group, there are negative anomalies in Rb, Th, Ta, and P. The same negative anomalies are seen in the low-silica group, with the exception of Ta.

The rare earth elements (REEs) highlight the relative degree of fractionation in the two clusters (Figure 4.24). There is no significant difference in the concentration of the middle and heavy rare earth elements, but the high-silica rocks are relatively enriched in light rare earth elements (LREEs), probably due to the presence of a substantial trapped liquid component in these rocks. In contrast, the low-silica rocks contain negligible trapped liquid, and thus negligible LREEs. The differing LREE patterns therefore support the idea that the high-silica rocks are orthocumulates or mesocumulates, whereas the low-silica rocks are adcumulates. It is also worth noting that the high-silica rocks are characterised by a positive Eu anomaly, due to the presence of cumulus plagioclase (Figure 4.24B).

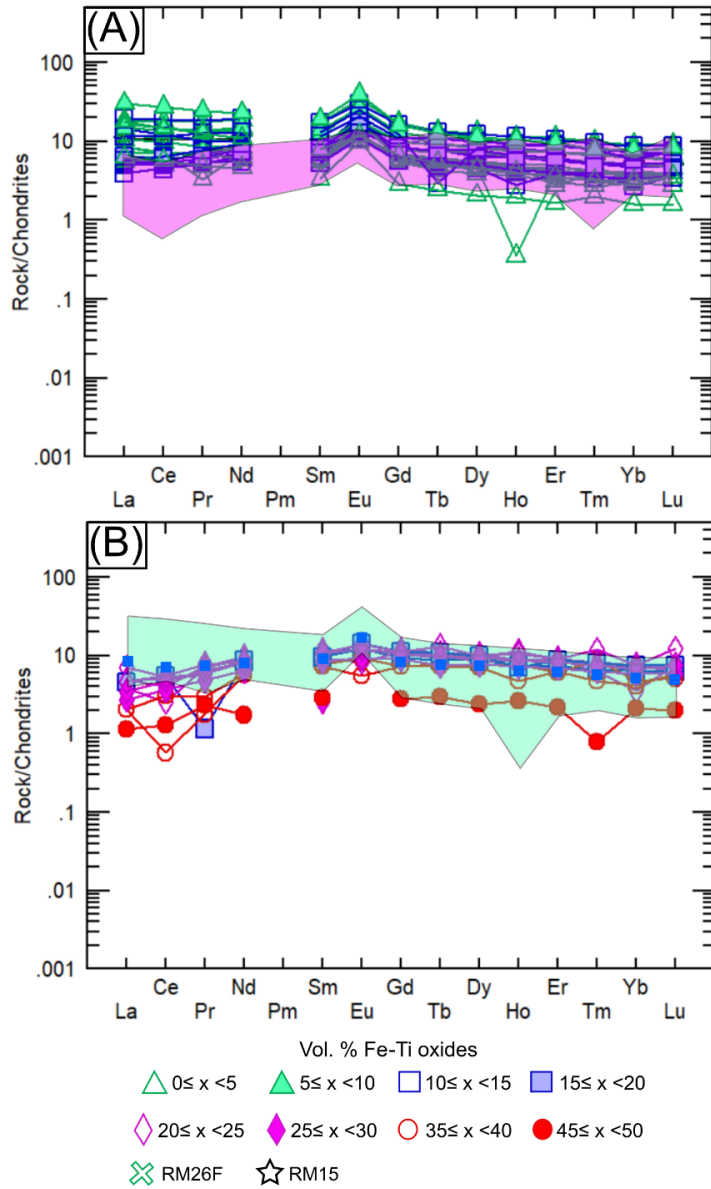


**Figure 4.24:** Multi-element variation diagrams showing rare earth element (REE) signatures for high-silica samples (A) and low-silica samples (B). Purple and green fields denote compositional range of low-silica, and high-silica groups, respectively. Normalisation factors from Sun and McDonough (1989).

## 4.6 Mineral compositions

### 4.6.1 Plagioclase

Plagioclase shows a compositional range of Anorthite content ( $An = Ca/[Ca + Na]$ ) from  $An_{35}$  to  $An_{57}$ , with most samples plotting in the andesine field ( $An < 50$ ) and only a few in the labradorite field ( $An > 50$ , Figure 4.25). Technically, gabbros containing plagioclase with An contents of  $< 50$  are actually diorites, but the term gabbro will continue to be used as there is no cumulus hornblende or biotite in any of the rocks. The grains show relatively subdued zonation, mostly not exceeding  $\pm 5\%$  An, with a subtle tendency towards reverse zonation (i.e., higher An in rims) (Figure 4.26).

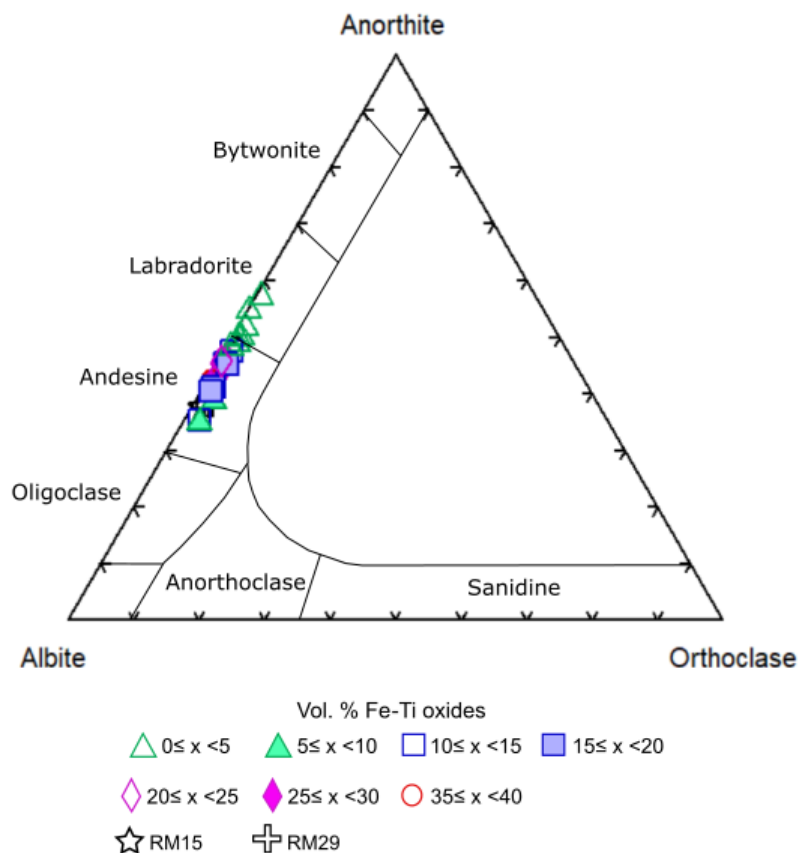


**Figure 4.25:** Albite-Anorthite-Orthoclase ternary diagram showing the composition of plagioclase in the intrusion ( $n = 25$ ). Data source is Appendix 3 (electron microprobe results).

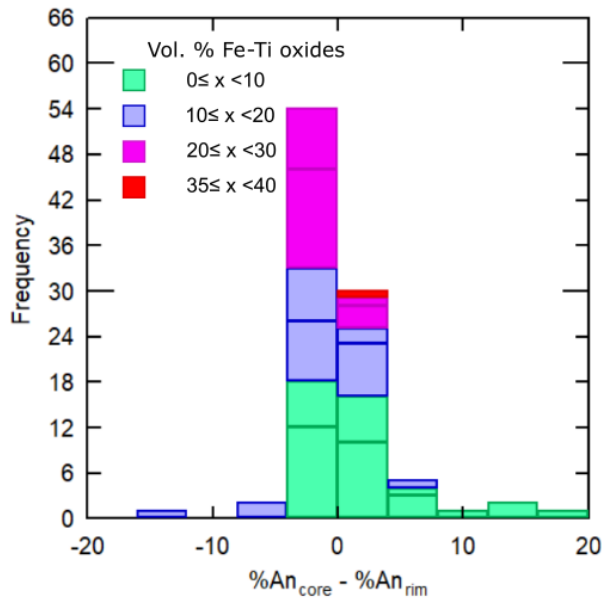


**Figure 4.26:** Histogram showing difference in An content of core and rim analyses of plagioclase. Negative values indicate reverse zoning with relatively An-rich rims. Positive values reflect normal zoning with relatively sodic rims (n = 96).

The variation in anorthite content with stratigraphic height is shown in Figure 4.27. The An content increases with height from the base of Zone A ( $An_{46}$  to  $An_{52}$ ), after which point An decreases progressively throughout the remainder of the intrusion to  $An_{35}$  at the top of Zone B. Three samples from Zone B (RM31-2237 m, LR04-3333 m and RM11-4073 m) represent minor reversals to higher An contents (albeit still andesine in composition). The reversal in Zone C at 4073 m is the most striking. Zone C plagioclases are amongst the most An-rich in the intrusion (up to 57 mol %).

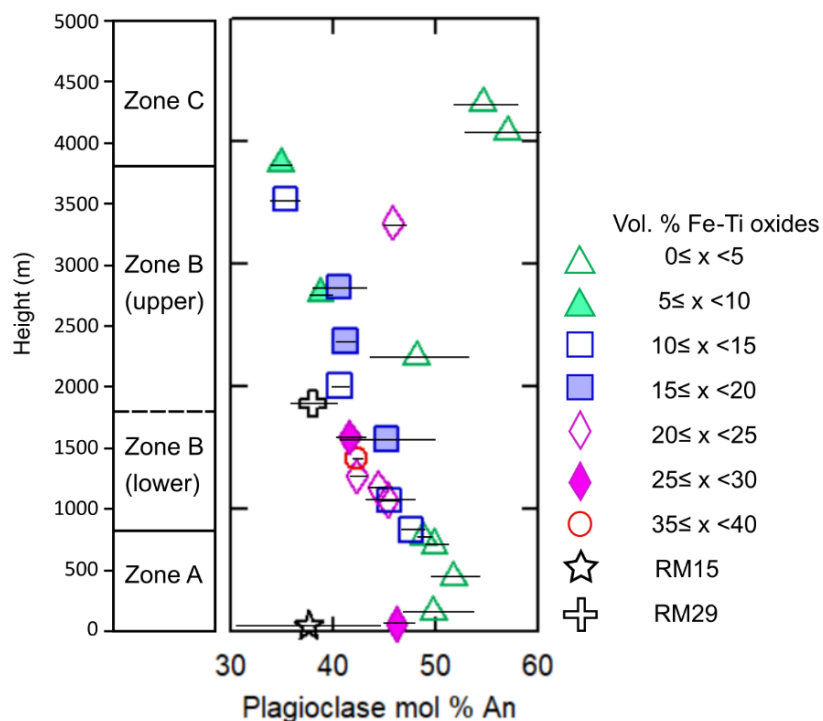


**Figure 4.27:** Plagioclase An content (mol %) plotted against stratigraphic height. Error bars reflect the within-sample variation in An. Note the relatively evolved (i.e., low An) composition of plagioclase in the RM15 and RM29 pegmatoidal gabbros (38 mol % An). Data source is Appendix 3 (electron microprobe results).

#### 4.6.2 Olivine

Olivine shows a compositional range in Forsterite content ( $Fo = Mg/[Mg + Fe]$ ) between  $Fo_{31}$  and  $Fo_{68}$ . The mineral exhibits negligible zonation in terms of Fo content (Figure 4.28). There is a small Fo enrichment in rims relative to cores (~3% Fo), in particular for oxide-rich samples, possibly reflecting subsolidus equilibration with oxide minerals.

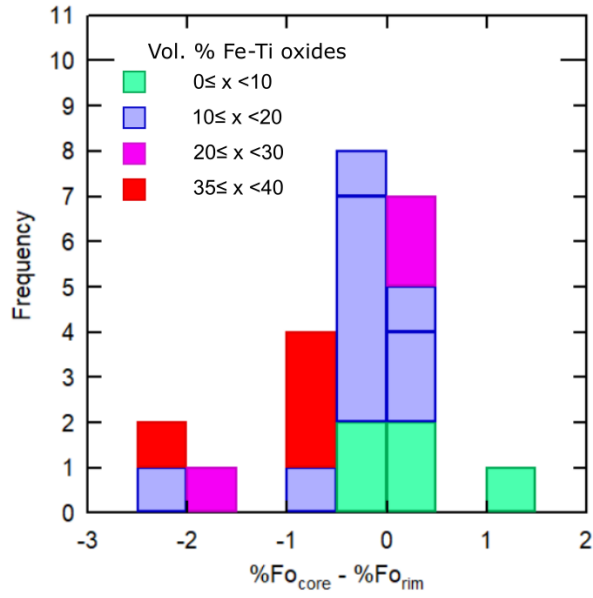


**Figure 4.28:** Histogram showing the difference in Fo between core and rim in olivine. Negative values indicate reverse zoning (n = 23). Data source is Appendix 3 (electron microprobe results).

The compositional variation of olivine is assessed using a binary plot of forsterite (Fo) vs. NiO (wt. %) content (Figure 4.29). The data show a weak positive correlation, resulting from the relatively high D values of Ni with regard to olivine (D = 6.1-24.8, see Mysen 1979).

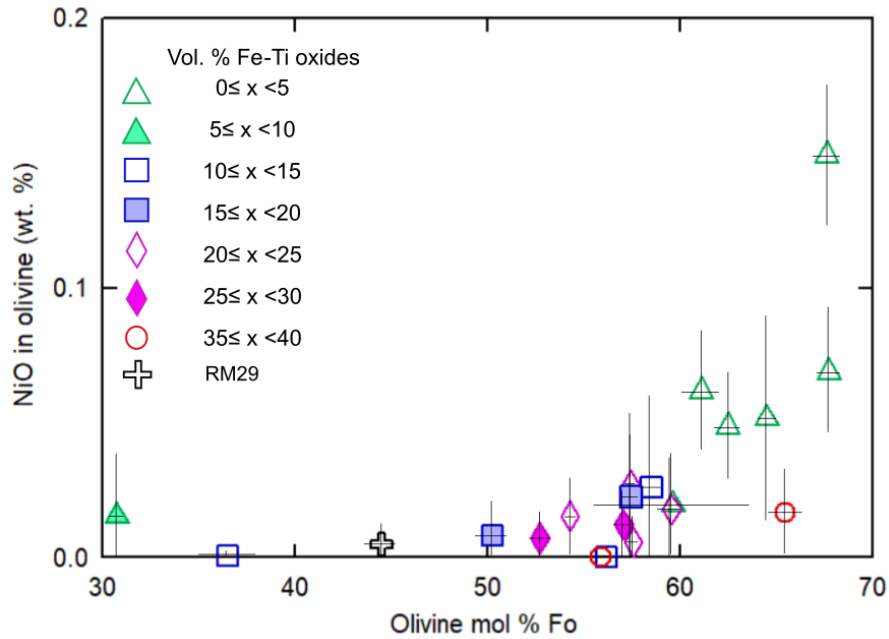


**Figure 4.29:** Binary variation diagram showing Fo content of olivine vs. NiO in olivine. There is a positive correlation in the data due to the compatible nature of NiO with respect to olivine. Error bars reflect the within-sample variation in Fo and NiO content of olivine in each sample NiO detection limit = 0.03 wt. %. Data source is Appendix 3 (electron microprobe results).

In Figure 4.30, the forsterite and NiO content of olivine is plotted against height in order to illustrate the stratigraphic variation in the composition of the mineral. In general, the trends of both Fo and Ni in olivine resemble the trend for An content in plagioclase (Figure 4.27). From the base, there is a progressive increase in forsterite with height until samples RM9 (771 m), followed by a progressive decrease throughout the remainder of the intrusion, with notable reversals at LR04 (3333 m) and RM11 (4073 m). The most magnesian olivines in the entire intrusion (Fo = ~69) are found at the top of the intrusion (Zone C). The NiO content of olivine is plotted against height in Figure 4.30B. The data show elevated NiO contents in zones A and C, with a strong NiO depletion in Zone B, mirroring the trends in the whole-rock compositions of Ni (Figure 4.22B).

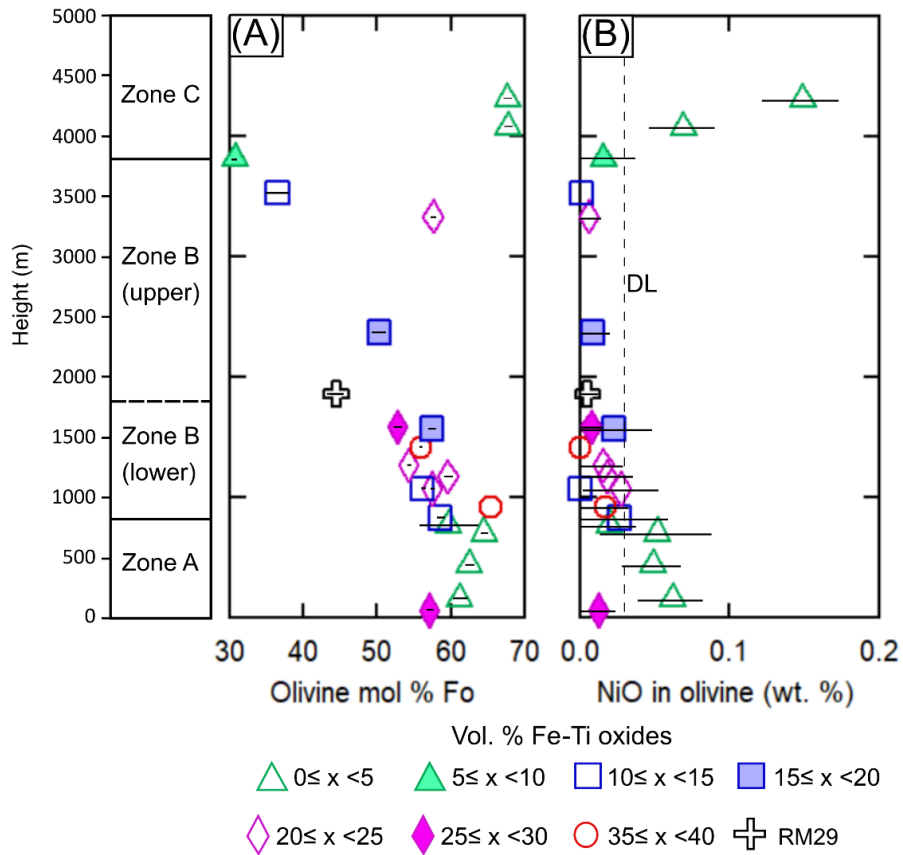


**Figure 4.30:** Stratigraphic variation of olivine according to: **(A)** Forsterite content (mol %) and **(B)** NiO (wt. %). Error bars reflect the within-sample variation in Fo and NiO content of olivine in each sample. Note the relatively evolved (i.e., low Fo) composition of olivine in the RM29 pegmatoidal gabbro (45 mol % Fo). DL = detection limit. Data source is Appendix 3 (electron microprobe results).

#### 4.6.3 Clinopyroxene

The magnesium number ( $Mg\# = Mg/[Mg + Fe]$ ) of clinopyroxene ranges from 62-77. The majority of clinopyroxene grains, in both the oxide-rich and oxide-poor samples, are slightly zoned (typically less than 5 % absolute difference between core and rim) (Figure 4.31). The maximum difference in Mg# between core and rim is 10.7 (RM31; 2232 m).

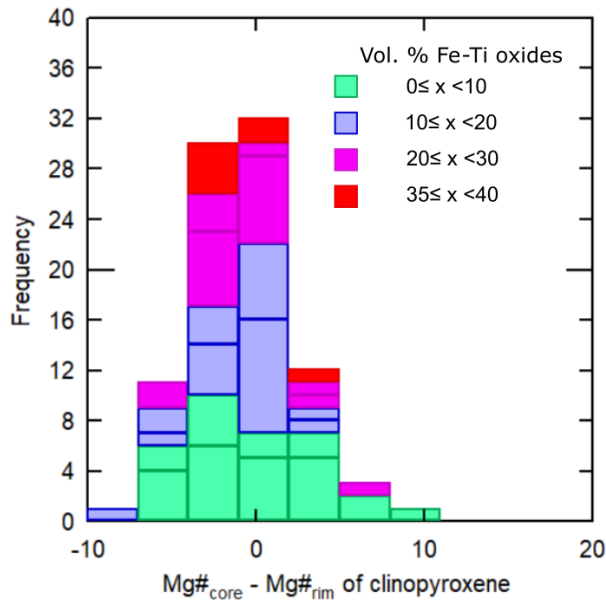


**Figure 4.31:** Histogram showing the difference in Mg# between core and rim in clinopyroxene. Negative values indicate reverse zoning (i.e., higher Mg# in rims) whereas positive values indicate normal zoning (n = 92). Data source is Appendix 3 (electron microprobe results).

In Figure 4.32, the magnesium number (Mg#) and Cr content of clinopyroxene is plotted against stratigraphic height. A general decrease from the bottom of Zone A to the top of Zone B can be recognized for both elements, with Mg# ranging from 74-63 and Cr<sub>2</sub>O<sub>3</sub> from 0.19 wt. % to below detection limit (<0.0048 wt. %) in this interval. Sample RM11 at 4073 m in Zone C clearly represents a reversal to this downward trend. Other reversals are difficult to pick out, as the standard deviation (i.e., the within-sample variation in Mg# of clinopyroxene) of Mg# in clinopyroxene is high. In sum, Mg numbers appear to be higher in Zone A and Zone C than in Zone B. Likewise, it is evident in the Cr<sub>2</sub>O<sub>3</sub> vs. height plot that while most samples contain <0.04 wt. % Cr<sub>2</sub>O<sub>3</sub>, the leucocratic samples of Zone A and Zone C are markedly more Cr-rich, containing up to 0.19 wt. % Cr<sub>2</sub>O<sub>3</sub>.

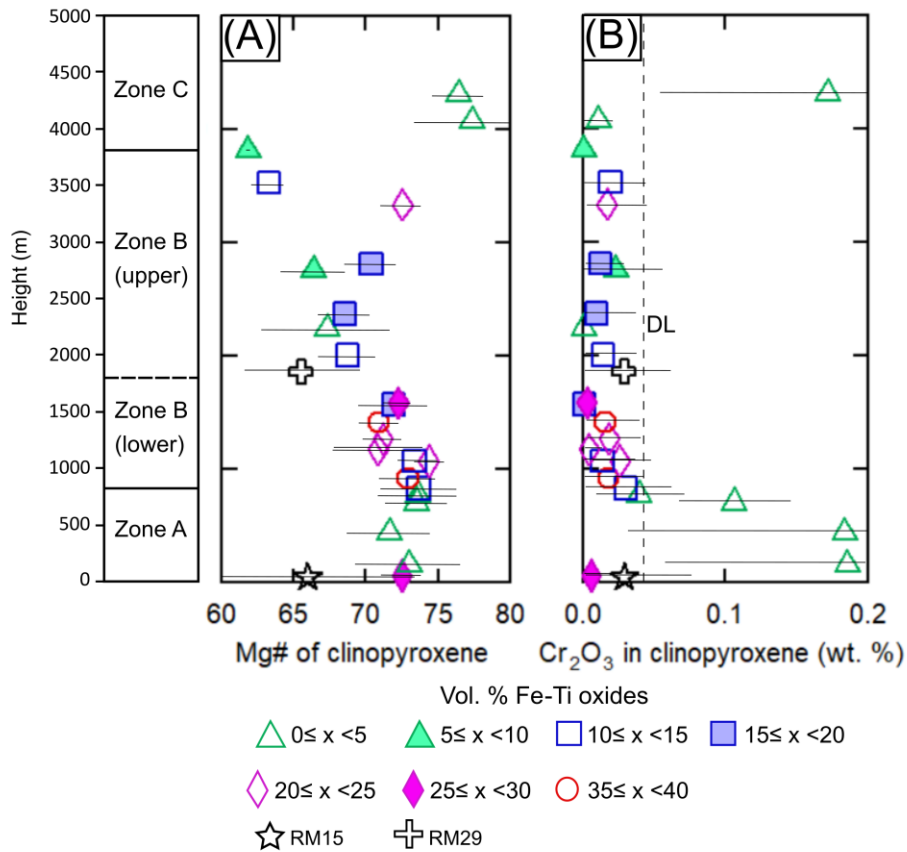


**Figure 4.32:** Stratigraphic variation of clinopyroxene according to: **(A)** Mg# and **(B)** Cr<sub>2</sub>O<sub>3</sub>. Error bars reflect the within-sample variation in Mg#/Cr<sub>2</sub>O<sub>3</sub> of clinopyroxene in each sample. Note the relatively evolved (i.e., low Mg#) composition of clinopyroxene in the RM15 and RM29 pegmatoidal gabbros (Mg# = 66). DL = detection limit. Data source is Appendix 3 (electron microprobe results).

In Figure 4.33, Mg# of clinopyroxene is plotted against Cr<sub>2</sub>O<sub>3</sub>, TiO<sub>2</sub>, Al<sub>2</sub>O<sub>3</sub>, and MnO in clinopyroxene. In general, the most magnesian-rich clinopyroxenes have the highest Cr, Ti and Al contents, and the lowest Mn contents. The correlation is strong for Al<sub>2</sub>O<sub>3</sub> and MnO, but much weaker for Cr<sub>2</sub>O<sub>3</sub> and TiO<sub>2</sub>.

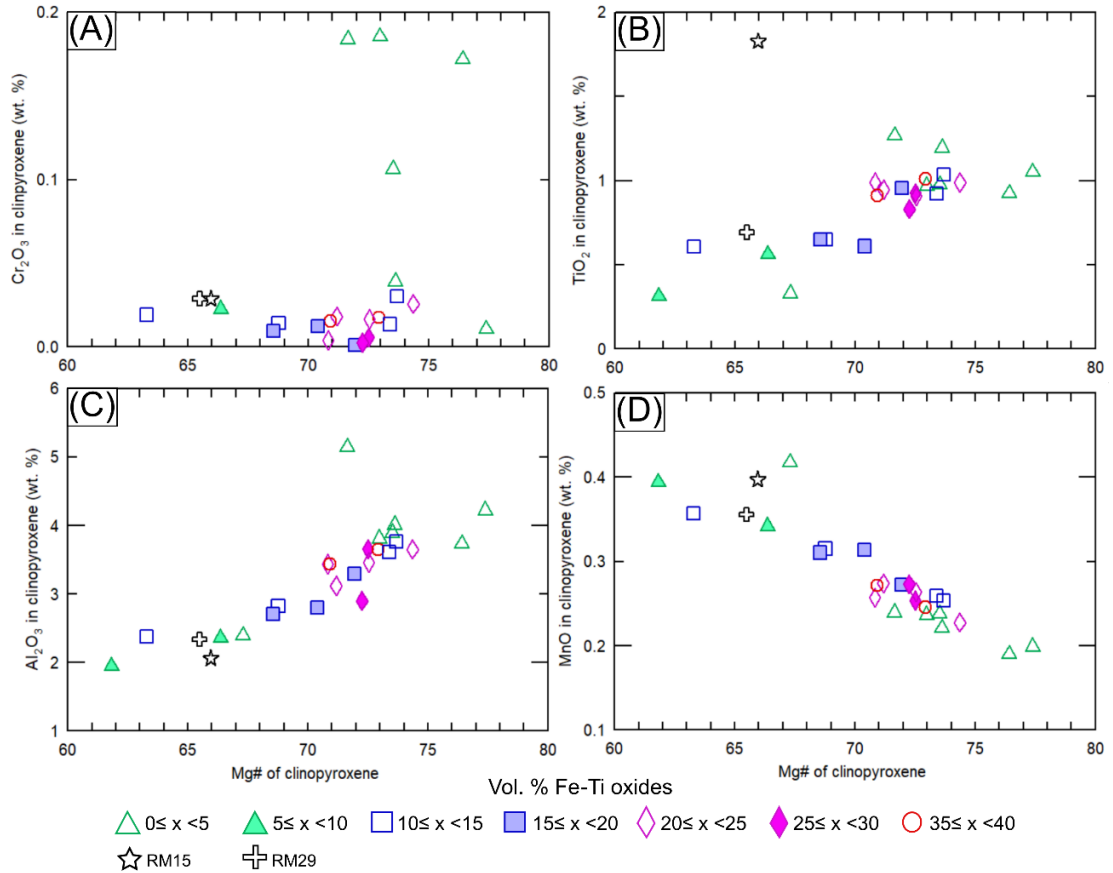


**Figure 4.33:** Binary variation plots of Mg# of clinopyroxene versus a selection of elements in clinopyroxene. **(A)** Cr<sub>2</sub>O<sub>3</sub>. Note that the most Cr-enriched samples come from zones A and C, and are poor in oxide minerals (<5 %). **(B)** TiO<sub>2</sub>. The highly Ti-enriched sample is RM15 (gabbroic pegmatite). **(C)** Al<sub>2</sub>O<sub>3</sub>. The highly Al<sub>2</sub>O<sub>3</sub>-enriched sample is RM16 (Zone A leuco-olivine-gabbro). **(D)** MnO. The samples that fall off the trend are RM31 (Zone B leuco-gabbro) with 0.42 wt. % MnO, and RM15 (gabbroic pegmatite) with 0.40 wt. % MnO. Data source is Appendix 3 (electron microprobe results).

The trace elements in clinopyroxene, determined by LA-ICP-MS, are plotted in a multi-element variation diagram in Figure 4.34. The pattern for the REEs is relatively flat with a subtle depletion in the LREEs relative to the HREEs. Two features are worth noting: (1) there is a broad increase in incompatible trace elements with increasing stratigraphic height in the intrusion, except for sample RM24 (Zone B; 2813 m) and RM6 (Zone B; 922 m) which are out of sequence; (2) there is a negative Sr and negative Eu anomaly, suggesting plagioclase was crystallising at the same time or before clinopyroxene.

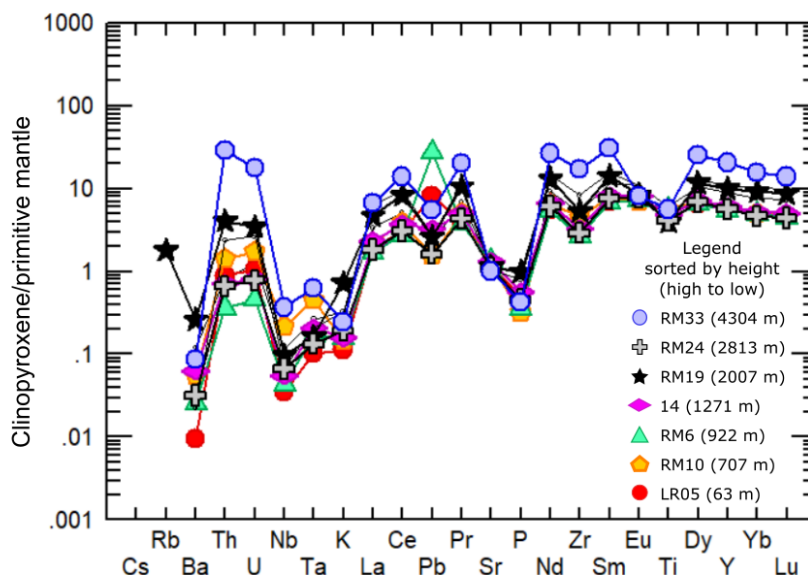


**Figure 4.34:** Multi-element variation diagram displaying average compositions of clinopyroxene in selected samples, as determined by LA-ICP-MS. In general, the concentration of most elements increases with stratigraphic height. Samples RM6 and RM24, however, do not conform to this trend. For most elements, both samples have lower concentrations than their respective underlying sample. Normalisation factors from Sun and McDonough (1989).

#### 4.6.4 Orthopyroxene

Equant grains of orthopyroxene interpreted to be of cumulus origin have only been identified in the uppermost sample of the intrusion (RM33; 4304 m) where the grains have an average Mg# of 69.9 (standard deviation = 0.94) and a very low average Cr<sub>2</sub>O<sub>3</sub> content of 0.017 wt. %.

#### 4.6.5 Magnetite

The compositional variation of magnetite is plotted versus stratigraphic height in Figure 4.35. In general, intercumulus magnetite in Zone A of the intrusion has elevated Cr<sub>2</sub>O<sub>3</sub> contents (0.37-2% Cr<sub>2</sub>O<sub>3</sub>) which is typical of intercumulus magnetite in mafic intrusions crystallising plagioclase, olivine and clinopyroxene (Namur et al. 2010). In the remainder of the intrusion, magnetite is relatively depleted in Cr<sub>2</sub>O<sub>3</sub> (<0.1 wt. %), except in sample RM31 at 2237 m.

In general, NiO contents of magnetite are higher in Zone A than in Zone B but there is a large amount of scatter. Sample LR06 (1073 m) is exceptionally high in Ni considering its position.

TiO<sub>2</sub> shows a different trend in that concentrations within magnetite are relatively low in Zone A (mostly <2 wt. %), but high (>2 wt. %) in Zone B. The samples in the mineralized lower portion of Zone B are particularly rich in TiO<sub>2</sub> (up to 8.57 wt. % in RM6 at 922 m).

There is an overall decrease in V<sub>2</sub>O<sub>3</sub> content from the base (~1.5 wt. % V<sub>2</sub>O<sub>3</sub>) to the top (0.76 wt. % V<sub>2</sub>O<sub>3</sub>). Several exceptions are worth noting: (1) although this trend terminates at the beginning of Zone B, V<sub>2</sub>O<sub>3</sub> contents initially go up with height; (2) samples RM14 (1078 m), LPM11 (1573 m), RM31 (2237 m) and LR04 (3333 m) are exceptions to the overall trend of decreasing V<sub>2</sub>O<sub>3</sub> with height in that their V<sub>2</sub>O<sub>3</sub> contents are higher than neighbouring samples. This trend of upwardly decreasing vanadium contents in magnetite also seen in other layered intrusions, e.g., the Bushveld Complex (Klemm et al. 1985; Barnes et al. 2004).

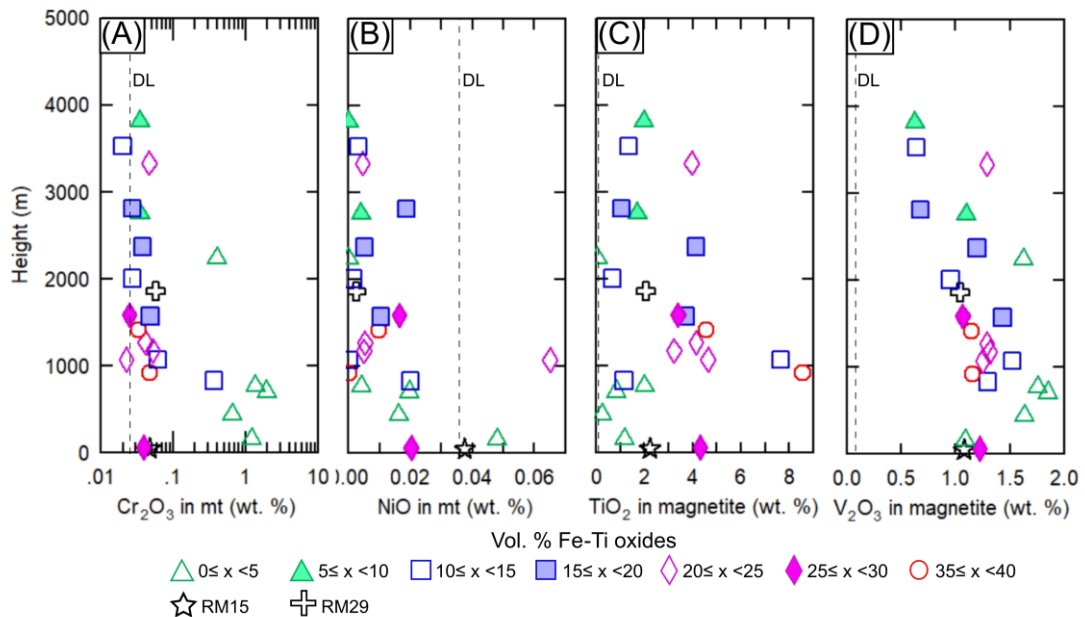


**Figure 4.35:** Stratigraphic variation of Cr<sub>2</sub>O<sub>3</sub> (A), NiO (B), TiO<sub>2</sub> (C), and V<sub>2</sub>O<sub>3</sub> (D) contents of magnetite (Mt) vs. height, as determined by electron microprobe. RM15 and RM29 are pegmatoidal gabbros. Note – magnetite not analysed in Zone C. DL = detection limit.

Bolsover (1986) observed that the TiO<sub>2</sub> content of magnetite from the Sybille Fe-Ti oxide deposit in Laramie, Wyoming, was positively correlated with the abundance of magnetite.

They inferred that this relationship is evidence of there having been just one original oxide phase that was a spinel rich in  $\text{Fe}_2\text{TiO}_4$  with 5-10%  $(\text{Fe,Mg})\text{Al}_2\text{O}_4$  (see Lindsley and Epler 2017). To test this model,  $\text{TiO}_2$  in magnetite is plotted as a function of vol. % Fe-Ti oxides (Figure 4.36). Volume % Fe-Ti oxides is used here as a proxy for vol. % magnetite, as the SEM images show that the oxide-rich rocks are proportionally richer in magnetite. There is a weak positive correlation, supporting the observations of Bolsover (1986). The positive correlation is also consistent with the observation that samples rich in Fe-Ti oxides are richer in cloth-textured ulvöspinel intergrowths (see Chapter 4.3.2). However, the model of Bolsover (1986) is not the only plausible explanation for the positive trend. Alternative models to explain the relative enrichment of  $\text{TiO}_2$  in the magnetites of oxide-rich rocks include: (a) lower proportions of cotectic ilmenite in oxide-rich rocks (facilitating higher uptake of  $\text{TiO}_2$  in magnetite during crystallisation); or (b) lower degrees of ilmenite exsolution in oxide-rich samples (leaving magnetites enriched in  $\text{TiO}_2$ ).

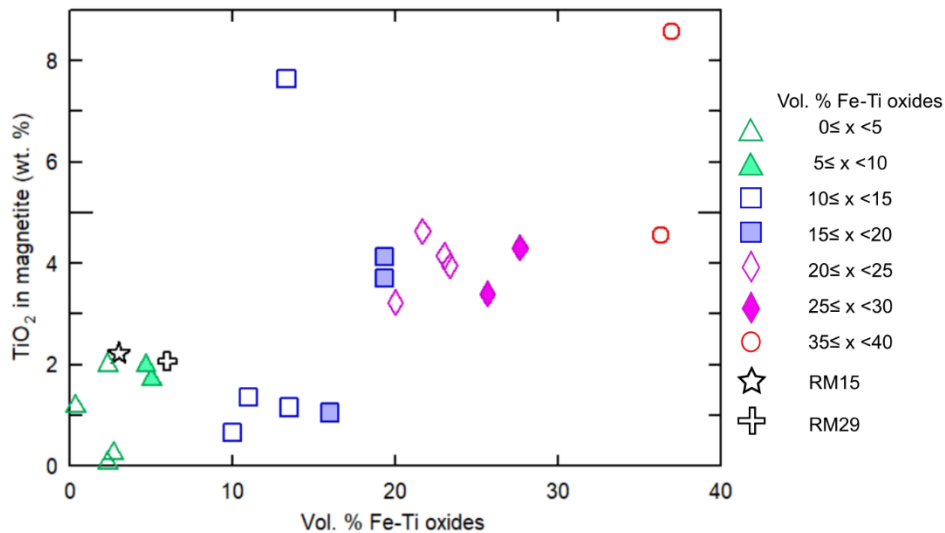


**Figure 4.36:**  $\text{TiO}_2$  content of magnetite versus the proportion of Fe-Ti oxides in the sample. Data source is Appendix 3 (electron microprobe results).

Trace element data for magnetite are plotted in the multi-element variation diagram of Dare et al. (2014) (Figure 4.37). The diagram distinguishes Fe-Ti-V and Fe-Ti-P deposits on the basis of trace elements. Two samples from Zone A (containing Cr-Ni rich intercumulus magnetite) plot in the Fe-Ti-V field (Figure 4.37A), whereas nearly all cumulus magnetite

(located in Zone B) plot in the Fe-Ti-P deposit field with lower Ni and Cr contents (Figure 4.37B). This is somewhat puzzling because the mafic part of the Étoile Suite contains very little apatite, and one would assume that the data should fall in the Fe-Ti-V field, which they do not.

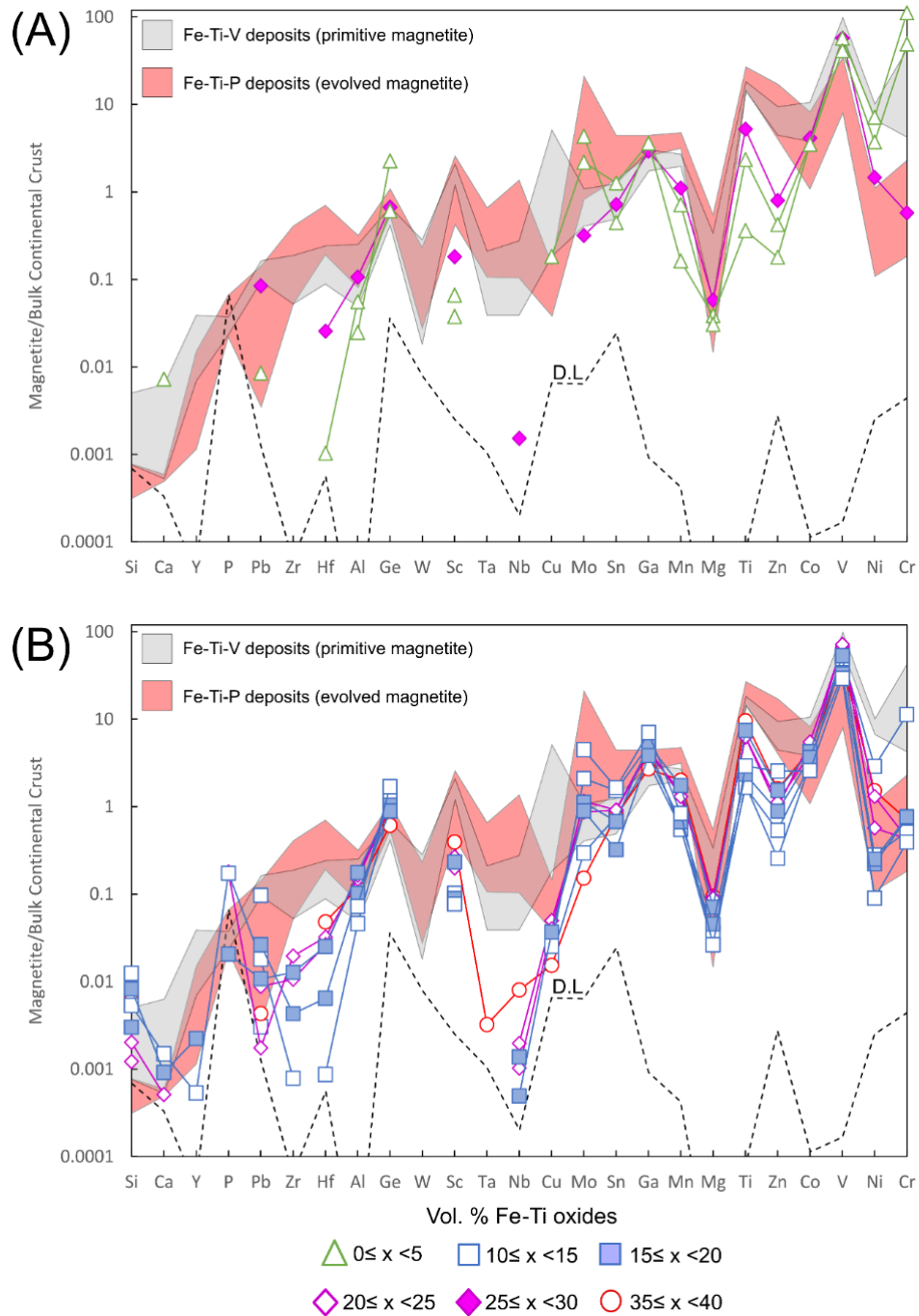


**Figure 4.37:** Multi-element variation diagrams for magnetite from Zone A (A) and Zone B (B) of the Étoile Suite. Gray field represents the range in composition of magnetite from Fe-Ti-V-mineralized magnetite layers of the Bushveld Complex, South Africa (Dare et al. 2014). Pink field represents the range in composition of magnetite from Fe-Ti-P-mineralized layers of

layered intrusions (Bushveld Complex, South Africa; Sept Iles, Canada) and anorthosite massifs (St. Charles de Bourget, Canada) (Dare et al. 2014). Normalisation factors from Rudnick and Gao (2003).

#### **4.6.6 Ilmenite**

In general, the microprobe data indicate that Cr, Ni and V contents of ilmenite are far lower than those of magnetite (Figure 4.38). Nevertheless, Cr in ilmenite shows somewhat similar trends to Cr in magnetite, albeit with more scatter. Concentrations are highest in Zone A (0.01-0.05 % Cr<sub>2</sub>O<sub>3</sub>), with generally lower concentrations being seen in the remainder of the intrusion, except for in reversals at 2237 m (RM31) and 4073 m (RM11). There is large scatter for NiO in ilmenite (Figure 4.38B), but there is a suggestive pattern of ilmenites in Zone B being relatively depleted in Ni compared to those in zones A and C. V<sub>2</sub>O<sub>3</sub> in ilmenite shows a large amount of scatter, but it is notable that the oxide-rich rocks at the base of Zone B display amongst the lowest V in ilmenite contents, possibly due to partitioning of V into magnetite.

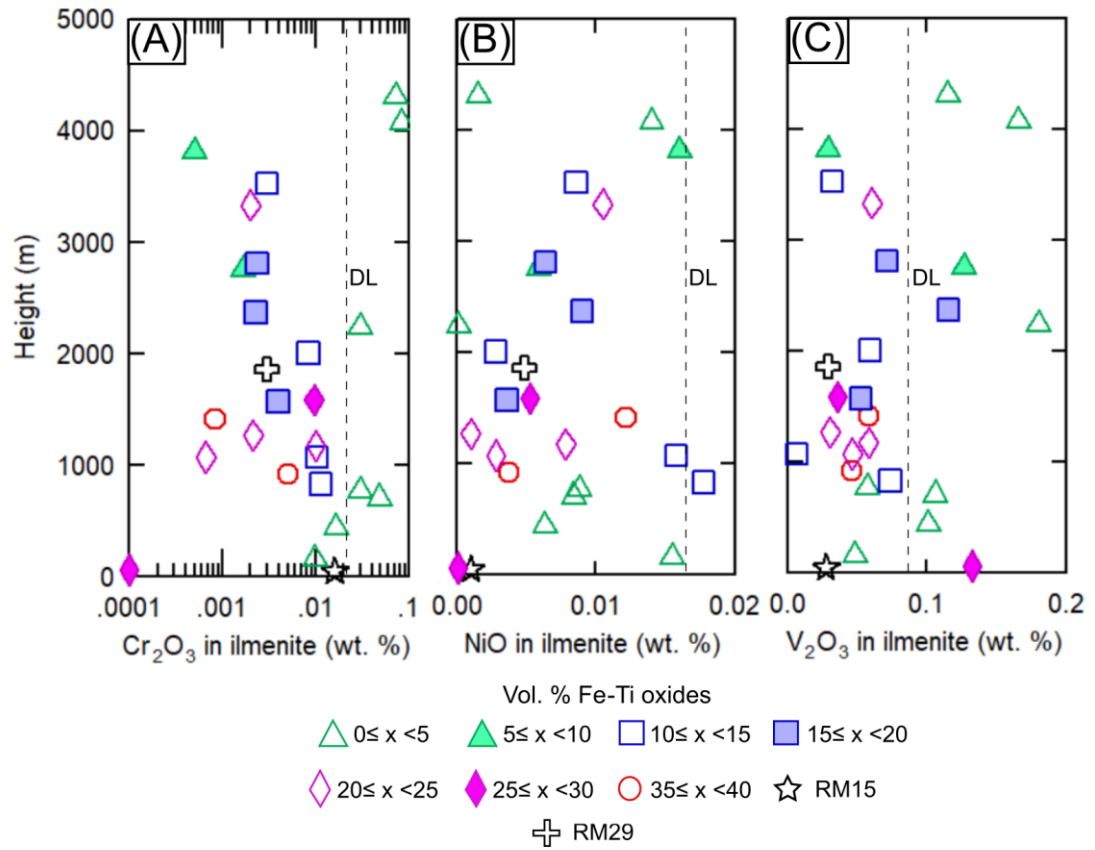


**Figure 4.38:** Concentration of selected elements in ilmenite plotted against stratigraphic height. **(A)**  $\text{Cr}_2\text{O}_3$ . **(B)** NiO. **(C)**  $\text{V}_2\text{O}_3$ . Data source is Appendix 3 (electron microprobe results).

## Chapter 5

### Discussion

#### 5.1 Crystallisation and emplacement history

##### 5.1.1 Fractional crystallisation history

The data collected in the present study place some constraints on the emplacement and crystallisation history of the Étoile Suite. The intrusion shows a broad trend of progressively more evolved compositions from the SE to the NW. This is recorded by cryptic mineral-chemistry variations, of e.g., anorthite in plagioclase (Figure 4.27), forsterite in olivine (Figure 4.30A), and Mg# in clinopyroxene (Figure 4.32A), which show a broad decrease towards the NW, suggesting that the base of the intrusion is in the SE and the top is in the NW. This interpretation is consistent with the decreasing trends of V, Cr and Ni in the whole-rock analyses (Figure 4.20E; Figure 4.22A, B) and in magnetite (Figure 4.35A, B, D). Zone A at the base crystallised from a more primitive melt ( $An > 50$ ) forming troctolites/olivine gabbros prior to oxide saturation. Oxides started to crystallise in Zone B from a more evolved magma ( $An < 50$ ), forming melanocratic oxide-rich wehrlites/gabbros in the lower part, and leucocratic oxide-poor gabbros/olivine gabbros in the upper part. Zone C is marked by a return to more primitive compositions (e.g., higher An in plagioclase) and the absence of cumulus oxides (Figure 4.30A; Figure 4.4). As the magmatic layering dips to the NW, it can be concluded that the intrusion is not overturned.

The stratigraphic distribution of the cumulus minerals can be used to provide an estimate of the crystallisation sequence in the mafic part of the Étoile Suite (Figure 4.4). Ignoring the anomalous oxide-rich sample at the base of Zone A (which could be an autolith or a faulted block), the crystallisation sequence appears to be: plagioclase + olivine → plagioclase + olivine + clinopyroxene (+ orthopyroxene in Zone C) → plagioclase + olivine + clinopyroxene + Fe-Ti oxides → plagioclase + olivine + clinopyroxene + Fe-Ti oxides + sulphides (Figure 4.4

and, with regard to sulphides, Figure 4.22D). This crystallisation sequence explains many of the compositional trends in the intrusion, including the general depletion of Cr in magnetite which can be attributed to prior formation of cumulus clinopyroxene as Cr is compatible into clinopyroxene ( $D = \sim 34$ , see Arth 1976). Likewise, the Ni depletion in magnetite can be explained by earlier olivine crystallisation as Ni is compatible into olivine ( $D = 6.1-24.8$ , see Mysen 1979).

The general trend of differentiation with height is interrupted by several compositional reversals, as evidenced by stratigraphic intervals where differentiation indices, such as An in plagioclase, Mg# in clinopyroxene and forsterite in olivine, as well as  $\text{Cr}_2\text{O}_3$  in magnetite and ilmenite become suddenly more primitive with height. The reversals are interpreted to reflect two minor magma replenishments to the chamber within Zone B (at 2237 m, RM31 and 3333 m, LR04) and a major replenishment at the start of Zone C (4073 m, RM11). The relatively pronounced degree of deformation in samples RM31 (Zone B) and RM33 (Zone C) further supports this interpretation (Figure 4.5C; Figure 4.7D).

### 5.1.2 Contamination

The presence in Zone C, and absence throughout zones A and B of cumulus orthopyroxene has implications for contamination. Fourny et al. (2019) modelled the degree of contamination in a number of troctolitic (olivine- and plagioclase-dominated) and noritic (orthopyroxene- and plagioclase-dominated) intrusions in the Nain Plutonic Suite and concluded that the noritic intrusions generally record higher degrees of crustal contamination (up to 30 %) compared to the troctolitic intrusions. The work of Fourny et al. (2019) therefore demonstrates that the degree to which orthopyroxene is predominant over olivine is – to a first order – the most important indicator of contamination. The results presented in Chapter 4 show that the mafic part of the Étoile Suite is troctolitic (i.e., olivine-bearing and orthopyroxene-free), and was thus likely little contaminated by crust. Quantitatively assessing the degree to which the magma parental to the Étoile Suite intrusion was contaminated during or after emplacement

is not straightforward as there is currently little information on the composition of the country rocks or the parent magma. For Zone C, it can be said that assimilation probably occurred given the presence of cumulus orthopyroxene. At the Étoile Suite, contamination could have occurred prior to final emplacement, in a staging chamber or magma conduit. Assessing the role of contamination in the orthopyroxene-free rocks (e.g., the oxide-rich rocks of Zone B) is more difficult as classical indicators of upper crustal contamination such as ratios of LILE vs. Nb or Ta (see Pearce et al. 2021) cannot be readily applied because the Nb and Ta are compatible with regard to magnetite, meaning that ratios of LILE vs. Nb or Ta are controlled by modal proportions.

### **5.1.3 Emplacement**

The major reversal at the base of Zone C potentially has major implications for the intrusion's mode of emplacement. The reversal is characterised by increases of An in plagioclase (Figure 4.27), Fo in olivine (Figure 4.30A), Mg# in clinopyroxene (Figure 4.32A), as well as the loss of cumulus oxides and the reappearance of pentlandite (Figure 4.27; Figure 4.30A; Figure 4.32A; Figure 4.12A). As will be shown in Chapter 5.5, this reversal is also characterised by an increase in Cu/Zr from around 0.5 to 2.5, i.e., the level of primitive mantle (Sun and McDonough 1989; Taylor and McLennan 1985). In addition, one of the samples from this zone contains cumulus orthopyroxene, which is not seen elsewhere in the intrusion. The compositional reversal at the base of Zone C could therefore be explained by a relatively late-stage magma replenishment which has undergone enhanced contamination. One issue with this model (Model 1) is that it is somewhat implausible that a later injection would undergo more contamination than earlier injections. Therefore, an alternative model (Model 2) is proposed in which the earlier injections are more contaminated. In Model 2, zones A and C represent remnants of the earliest contaminated magma pulses lining the margins of the Étoile Suite, and the Zone B cumulates represent subsequent magma pulses that displaced the bulk of the earlier contaminated magma. This model would explain the lack of orthopyroxene in the rocks

that crystallised from later-intruding magma pulses (i.e., the Zone B gabbros and olivine gabbros), which presumably underwent less country rock contamination, as the crystallisation products of the preceding magma pulses had lined the contacts of the magma conduits and magma chamber. Snyder and Simons (1999) proposed a similar explanation to account for the relatively uncontaminated nature of the later 'Hybrid Series' in the Newark Island Intrusion, Labrador, Canada. The lack of observed cumulus orthopyroxene in Zone A, however, is somewhat inconsistent with Model 2.

A number of authors have proposed that layered intrusions undergo a prolonged late-stage history of evolved melt and volatile percolation (Boudreau 2019 and references therein). This model could explain the reverse zonation of plagioclase, given that Na and K are soluble in relatively cold Si-undersaturated rocks derived from the lower levels of intrusions (Meurer et al. 1997). This model only accounts for reverse zonation of plagioclase – reverse zonation of olivine and clinopyroxene is more likely a result of subsolidus equilibration with oxides.

## **5.2 Origin of the Fe-Ti-(V) oxide mineralization**

Massive to semi-massive layers of magnetite and ilmenite are common in the upper portions of mafic-ultramafic layered intrusions (Namur et al. 2015). However, the origin of the mineralization remains debated. Formation of economic deposits typically requires two steps, namely saturation of the magma in Fe-Ti oxide minerals (see below), followed by concentration of the Fe-Ti oxide minerals into massive or semi-massive layers or veins via gravitational processes (e.g., crystal settling according to Stokes' Law, McBirney and Noyes 1979; and slumping of semi-consolidated cumulates, Forien et al. 2015).

### 5.2.1 Triggers of oxide saturation

#### *Fractionation of the silicate parent magma*

The observation that oxides typically occur in the upper portions of layered intrusions suggests that fractionation plays a key role in bringing the magma to Fe-Ti oxide saturation. Fractionation (and the associated increase in  $fO_2$ ) may trigger: (a) saturation in Fe-Ti oxide **crystals** (Toplis and Carroll 1995) or (b) formation of silica-rich and iron-rich immiscible **melts** (Charlier and Grove 2012). There is debate as to the composition of the proposed Fe-rich immiscible melt. Some authors advocate for an 'Fe-Ti *oxide* melt' consisting almost entirely of iron oxide and apatite, with little or no  $SiO_2$  (Philpotts 1967). Others advocate for an Fe-rich *silicate* melt with more modest  $FeO_{(total)}$  values of ~30 wt. % (see Charlier and Grove 2012). The various models for the origin of Fe-Ti oxide mineralization are discussed below, starting with the two liquid immiscibility models.

#### *Fe-Ti oxide liquid immiscibility*

This model was first proposed by Philpotts (1967) who was able to produce three immiscible melts by heating a mixture of diorite, magnetite and apatite to 1420 °C. One of the melts consisted of approximately two parts  $Fe_3O_4$ , and one part apatite (plus minor silicate). Philpotts (1967) suggests that crystallisation of this melt can account for the formation of massive accumulations of magnetite and apatite.

The model offered an explanation for the essentially silicate-free nature of many oxide ores, as well as the cross-cutting relationships seen between the ores and their host rocks. Freestone (1978), Roedder (1979), and Naslund (1983) were subsequently able to produce immiscible iron oxide liquids from silicate liquids. However, the composition of the starting liquid in their experiments differed to that of naturally occurring rocks. Using compositions similar to natural rocks, magnetite and ilmenite crystals form before immiscible Fe-Ti oxide liquids (Toplis

and Carroll 1995). Furthermore, Wang et al. (2007) have shown that a dry mixture of two-thirds Fe-Ti oxides and one-third apatite by weight only melts at above  $\sim 1450$  °C, which is an unrealistically high melting temperature for liquids in the upper crust (Lindsley and Epler 2017). Many authors have called upon fluxes (mainly apatite, fluorine, and carbon) to lower the melting point of Fe-Ti oxide melts to geologically plausible temperatures, but Lindsley and Epler (2017) concluded that the addition of fluxes like phosphate, fluorine and apatite fails to do so. Based on the weight of the above evidence, the immiscible Fe-Ti oxide liquid model is not considered viable for the Étoile Suite.

#### *Silicate liquid immiscibility*

Charlier and Grove (2012) have shown that increased levels of  $\text{Na}_2\text{O}$ ,  $\text{K}_2\text{O}$ ,  $\text{P}_2\text{O}_5$ ,  $\text{TiO}_2$  in silicate magmas may promote immiscibility of two conjugate silicate liquids, one being relatively Si-rich ( $\sim 70$  %  $\text{SiO}_2$ ,  $\sim 5$  %  $\text{FeO}$ ), and one being relatively Fe rich (40 %  $\text{SiO}_2$ ,  $\sim 25$  %  $\text{FeO}$ ).  $\text{TiO}_2$  and  $\text{FeO}$  partition into the Fe-rich conjugate, making it conducive to enhanced magnetite and ilmenite crystallisation.

The silicate liquid immiscibility model could offer an explanation for the preferred association of oxides with clinopyroxene in the Étoile Suite (Figure 4.5F); Based on a microtextural study at Skaergaard, Vukmanovic et al. (2018) have argued that the Fe-rich silicate liquid preferentially wets mafic phases and oxides, whereas the Si-rich liquid preferentially wets plagioclase.

However, the silicate liquid immiscibility model predicts that the crystallisation products of the Fe-rich conjugate should have a substantial phosphate component, as  $\text{P}_2\text{O}_5$  preferentially partitions into the Fe-rich melt during unmixing (Charlier and Grove et al. 2012). In view of the absence of apatite in the cumulates, this model is not considered for the Étoile Suite.

### *Contamination*

Oxide crystallisation from a silicate magma or immiscibility of Fe-rich liquids could have been triggered by contamination, notably if the contaminant is relatively oxidising. For example, assimilation of evaporite by basalt may lead to a significant increase in  $fO_2$  of the basalt (Iacono-Marziano et al. 2017), and Ganino et al. (2018) propose that the addition of  $CO_2$  to the Panzhihua magma when the footwall carbonates were converted into skarns and marbles lead to an increase in  $fO_2$ , triggering early crystallization of V-bearing magnetite.

### *Saturation and crystallisation of oxide crystals*

In view of the issues with the immiscibility models discussed above, direct crystallisation of oxide crystals from a single, evolved basaltic liquid is the preferred model for the Étoile Suite. The cotectic proportion of magnetite during crystallisation from basalt is as high as 45 % (see Toplis and Carroll 1996) – broadly consistent with the observed oxide contents in the Étoile Suite (maximum 48 %). Thus, the oxide mineralization in the intrusion can be largely explained by cotectic oxide crystallisation from an evolved basaltic melt, without significant additional concentration by gravitational processes. This constitutes a major difference to, e.g., the Bushveld Complex where massive oxide layers are common (Klemm et al. 1985), requiring a secondary concentration mechanism such as granular flow (Maier et al. 2013; Forien et al. 2015).

### **5.3 Oxygeothermometry**

The oxygen fugacity ( $fO_2$ ) of 19 samples from the Étoile Suite has been determined using compositions of co-existing oxides and silicates using the QUILF program by Andersen et al. (1993) (Table 5.1; Figure 5.1). The samples lie on a broadly horizontal trend at around 1.0 log units above the FMQ buffer (average = +1.15; min = +0.18; max = +1.7). Toplis and

Carroll (1995) show that the appearance temperature of magnetite increases by 30°C per log  $f_{O_2}$  increase above FMQ (Figure 5.2). As a result, at FMQ +1, magnetite (a) begins crystallising earlier (i.e., at lower degrees of magmatic differentiation), and (b) crystallises before ilmenite, which places further constraints on the crystallisation sequence of the parental magma. The higher proportion of magnetite in comparison to ilmenite (approximately 2:1) in the oxide-rich wehrlite (from the lower portion of Zone B) that was analysed via SEM (Figure 4.13; Figure 4.15) is consistent with magnetite crystallising before ilmenite.

Samples in which the Fe-Ti oxide assemblage is dominated by magnetite will cool along an ulvöspinel isopleth, whereas samples with significantly more ilmenite than magnetite will cool along an ilmenite isopleth (see Frost et al. 1988). It appears that the Étoile Suite data form a horizontal trend and thus do not plot on either an ulvöspinel or ilmenite isopleth. Therefore, it appears that the average magnetite to ilmenite ratio in the intrusion is approximately 1:1.

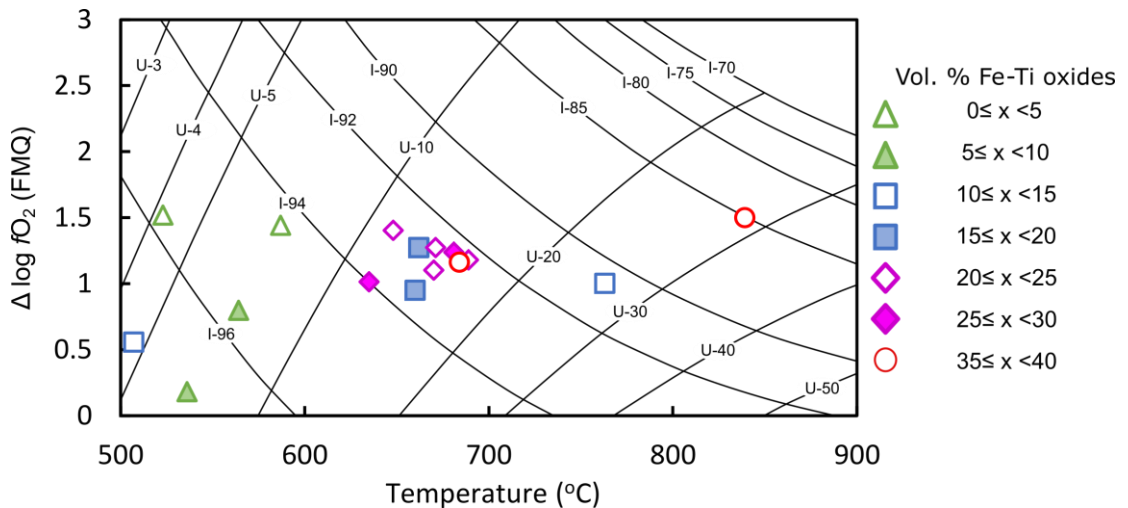


**Figure 5.1:**  $f_{O_2}$  and temperature conditions marking the end of the oxy-exsolution process for each sample, attained using QUILF by Andersen et al. (1993). Note that the closure temperature of the oxy-exsolution process is higher in the oxide-rich samples. FMQ = fayalite-magnetite-quartz buffer; QUILF = quartz-ulvöspinel-ilmenite-fayalite equilibrium; U = ulvöspinel isopleth; I = ilmenite isopleth. Ulvöspinel and ilmenite isopleths after Frost et al. (1988).

**Table 5.1:** Temperature and  $fO_2$  of selected samples calculated using QUILF by Andersen et al. (1993).

<b>Sample</b>	<b>Fe-Ti oxides (vol. %)</b>	<b>Height (m)</b>	<b>T (°C)</b>	<b>P (bars)</b>	<b>log <math>fO_2</math></b>	<b><math>\Delta\log</math> <math>fO_2</math> (FMQ)</b>	<b>Silica activity</b>
RM20	0	160	523	5000	-20.645	1.521	0.758
RM16	3	439	347	5000	-30.45	1.214	0.614
RM10	0	707	488	5000	-21.96	1.699	0.764
RM9	2	771	587	5000	-18.32	1.443	0.755
RM29	6	1861	564	5000	-19.803	0.799	0.749
RM12	5	3815	536	5000	-21.474	0.183	0.653
RM8	14	832	662	5000	-16.172	1.275	0.742
RM14	13	1078	763	5000	-13.891	1.004	0.689
RM3	11	3526	507	5000	-22.29	0.558	0.753
LPM11	19	1573	662	5000	-16.172	1.275	0.742
LR01	19	2374	660	5000	-16.573	0.95	0.742
LR06	22	1073	689	5000	-15.533	1.18	0.704
RM5	20	1175	648	5000	-16.463	1.403	0.75
14	23	1271	670	5000	-16.121	1.102	0.734
LR04	23	3333	671	5000	-15.93	1.275	0.743
LR05	28	63	681	5000	-15.709	1.237	0.739
RM17	26	1585	635	5000	-17.218	1.014	0.71
RM6	37	922	839	5000	-11.794	1.5	0.713
LPM09	36	1413	684	5000	-15.681	1.163	0.732

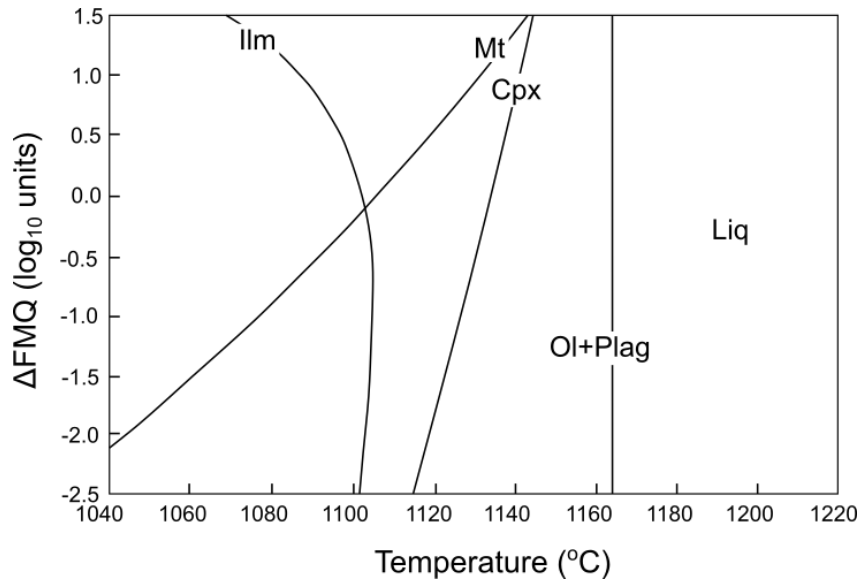


**Figure 5.2:** Experimentally determined phase equilibria for synthetic ferrobasalt. Reproduced after Toplis and Carroll (1995). Permission acquired from Journal of Petrology.

#### 5.4 Effect of oxygen fugacity on the V prospectivity of layered intrusions and anorthosite massifs

The V content of magnetite in the Étoile Suite is relatively high (up to 1.85 wt. %  $V_2O_5$  in the lower portion of Zone B) compared to magnetite from the Lac Saint-Jean (Quebec, Canada), Northwest River (Labrador, Canada) and Suwalki (Poland) anorthosite massifs (Figure 5.3), which varies between 0.62 and 1.25 wt. %  $V_2O_5$  (Grant 2020; Valvasori et al. 2020; Charlier et al. 2009). One factor that may play a role is oxygen fugacity ( $fO_2$ ), considering that the V content of magnetite is strongly controlled by  $fO_2$  (see Toplis and Corgne 2002). Toplis and Corgne (2002) showed that in ferrobasaltic melts, extremely  $V_2O_5$ -enriched magnetite (i.e., on the order of 2.25 wt. %  $V_2O_5$ ) only crystallises in a narrow window, between 0.25 log units above and 0.25 log units below the FMQ buffer (FMQ +0.25 to FMQ -0.25). Magnetite that crystallises at higher  $fO_2$  will be increasingly poor in V because the ratio of  $V^{5+}$  to  $V^{3+}$  and  $V^{5+}$  to  $V^{4+}$  increases with  $fO_2$  and  $V^{5+}$  is less compatible into magnetite than  $V^{3+}$  (Toplis and Corgne 2002). For example, at FMQ +1 (similar to the  $fO_2$  calculated for Étoile Suite magnetite in Figure 5.1) magnetite will have lower  $V_2O_5$  contents, on the order of 1.40

wt. %  $V_2O_5$ , and at FMQ +1.5, magnetite will have still lower concentrations of  $\sim 0.90$  wt. %  $V_2O_5$ ) (see Figure 11b in Toplis and Corgne 2002). The results of Toplis and Corgne (2002) may suggest that – in contrast to V deposits in troctolitic-gabbroic layered intrusions like the Étoile Suite – V deposits in anorthosite massifs, such as the Suwalki, Lac Saint-Jean and Northwest River anorthosite massifs may have crystallised from more oxidised magmas, in which (a) the partition coefficient of V into magnetite is lower, and (b) the appearance temperature of magnetite is higher (as illustrated by the phase equilibria of Toplis and Carroll 1995, Figure 5.2). Indeed, Charlier et al. (2009) calculated a high  $fO_2$  value of FMQ +2 to FMQ +3.46 using QUILF by Andersen et al. (1993) for sample U2-04 – a gabbroic Fe-Ti oxide ore from Suwalki. And in several samples, they observed the coexistence of labradorite-type plagioclase ( $An_{50-69}$ ) and cumulus magnetite, showing that magnetite began crystallising at relatively high temperatures, i.e., from a relatively primitive basaltic magma in equilibrium with labradorite-type plagioclase.

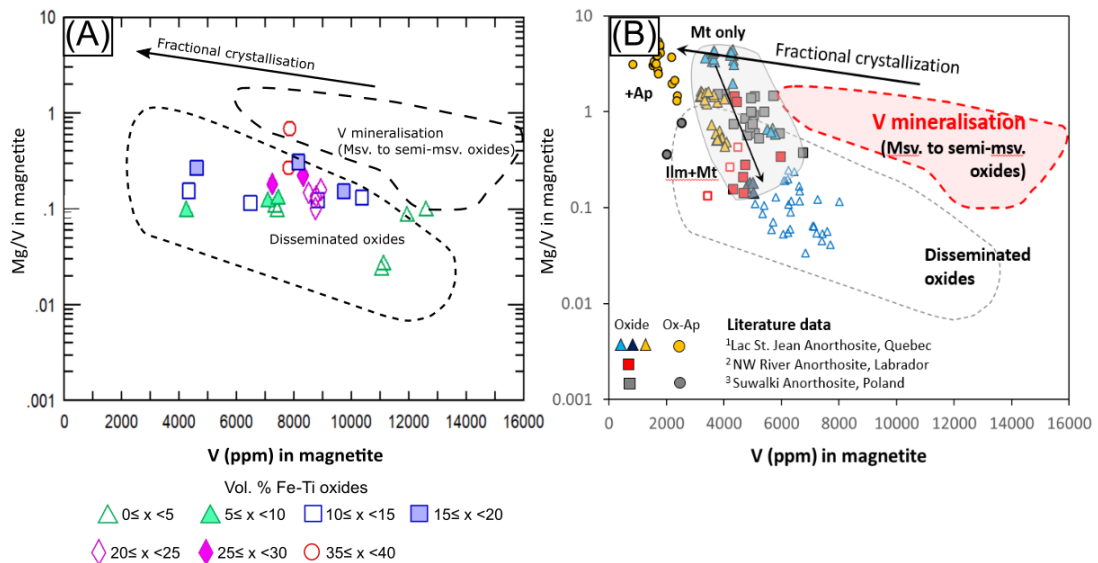


**Figure 5.3:** V vs. Mg/V diagrams by Dare et al. (2019) for discrimination of magnetite forming massive to semi-massive V mineralization from magnetite forming disseminated V mineralization. **(A)** V vs. Mg/V of magnetite from the Étoile Suite. Data source is Appendix 3 (electron microprobe results). **(B)** V vs. Mg/V of magnetite from oxide mineralisation in the Lac Saint-Jean Anorthosite (Quebec), NW River Anorthosite (Labrador) and Suwalki Anorthosite (Poland). Magnetite in disseminated form has lower Mg/V than magnetite in massive to semi-massive form due to the loss of Mg (indicated by arrow) from re-equilibration of oxides with mafic minerals (Dare et al. 2019). Solid symbols are massive oxides. Open symbols are

disseminated oxides. Superscript numbers indicate data sources: 1, Grant (2020); 2, Valvasori et al. (2020); 3, Charlier et al. (2009).

## 5.5 Origin of the sulphides

The Étoile Suite intrusion contains accessory sulphides throughout, mostly in proportions of  $\ll 1$  vol. %, except in the oxide-rich mineralised zone where sulphides can reach proportions of several percent by volume ( $\sim 2\%$ ). In many samples the sulphides are clearly of magmatic origin, as indicated by their frequently globular or interstitial texture, as well as their composition, consisting mainly of pyrrhotite, with additional chalcopyrite and minor pentlandite (Figure 4.12A). However, many sulphides in the central portion of the intrusion (Zone B) are commonly replaced by pyrite, marcasite and goethite (Figure 4.12B).

The whole-rock Cu/Zr ratio is plotted against stratigraphic height and shows that the proportion of sulphides is markedly enriched in the oxide-rich lower portion of Zone B from 832 m to 1143 m (Figure 5.4). A similar trend of elevated sulphide contents associated with oxide mineralization has been found in several other layered intrusions, e.g., Rincon del Tigre, Bolivia (Prendergast 2000), Koitelainen, Finland (Mutanen 1997) and Stella, South Africa (Maier et al. 2003). This sharp increase in sulphides, from  $\ll 1$  % to  $\sim 1-2$  %, is matched by an increase in Cu contents, from a background of  $\sim 50$  ppm to a peak of 743 ppm in the oxide rich interval (Figure 4.21H). One can assess the fertility of the parent magma by considering the Cu/Zr ratio of the rocks (Figure 5.4). It appears that the Cu/Zr ratio below the oxide mineralization is consistent with the Cu/Zr ratio of primitive mantle ( $\sim 2.5$ , Sun and McDonough 1989; Taylor and McLennan 1985). In the oxide-rich zone, Cu/Zr increases to 28, due to the presence of cumulus sulphides (Figure 5.4). Above the oxide zone, Cu/Zr falls to  $\sim 1$ , reflecting depletion of the magma in Cu. There is a reversal back to mantle-like Cu/Zr ratios in Zone C.

These data help to constrain several questions of petrogenesis, stratigraphy and mode of emplacement. Firstly, the data confirm that the base of the intrusion is in the south. Secondly, the data suggest that the initial magma was likely sulphide-undersaturated upon emplacement, forming cumulates with mantle-level Cu/Zr (zones A and C). Thirdly, the observation that sulphide saturation was reached at  $\sim 832$  m, broadly at the same level as the onset of significant

oxide crystallisation, suggests that the crystallisation of the oxides could have locally triggered sulphide saturation, possibly due to a decrease in FeO, which is the major bonding partner of S in a typical magma (Scoates and Mitchell, 2000). Alternatively, if Zone B was emplaced as a distinct oxide-rich magma batch, sulphide saturation could have occurred in a lower staging chamber.

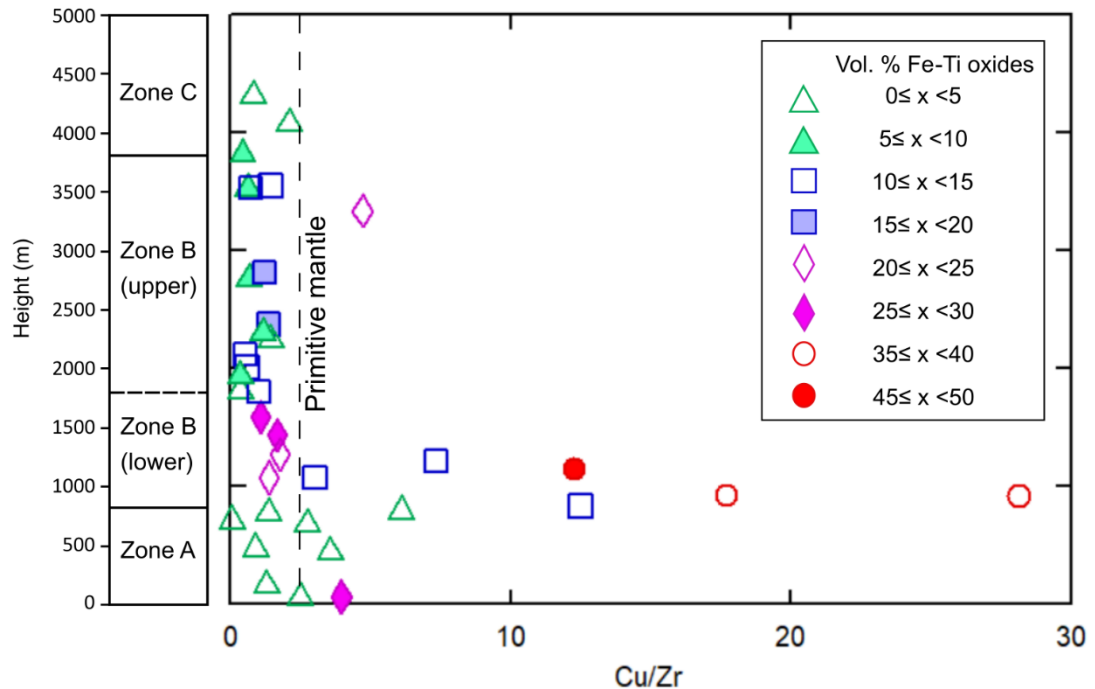


**Figure 5.4:** Whole-rock Cu/Zr ratio as a function of stratigraphic height in the mafic part of the Étoile Suite. Cu/Zr ratio in Zone A is roughly equivalent to primitive mantle. At the base of Zone B – corresponding to the oxide mineralization – it rises to ~30, before falling to <2, where it remains for the remainder of the intrusion (exceptions at 3333 m and 4073 m). Zr in primitive mantle = 11.2 (Sun and McDonough 1989); Cu in primitive mantle = 28 (Taylor and McLennan 1985).

## 5.6 Association with AMCG magmatism

### 5.6.1 Introduction

The age of the mafic part of the Étoile Suite intrusion is  $1148.3 \pm 9.6$  Ma (Jean David, personal communication), within the age range of the Lac Saint-Jean (LSJ) Anorthosite Suite, which has been dated at 1160-1135 Ma by Higgins and van Breemen (1996). This result shows



**Figure 5.5:** Distribution of anorthosite massifs and major mafic intrusions as well as their Fe-Ti deposits in the Grenville Province. *Anorthosite massifs:* ARA, Alexis River; BEA, Berté; LA, Labrie; DLBA, De La Blache; HSPA, Havre-Saint-Pierre; LFA, Lac Fournier; LSJA, Lac Saint-Jean; LVA, Lac Vaillant; MA, Morin; PA, Pambrun; PMA, Petit-Mécatina; RAA, Atikonak River; RPA, Rivière Pentecôte; SA, Shawinigan; SUA, Saint-Urbain; TA, Tortue. *Mafic intrusions and intrusive complexes:* GI, Grady Island; M, Musquaro; MMIS, Mealy Mountains; MT, Matamec; OM, Ossok Mountain; R, Raudot; SILC, Sept-Îles; WBA, White Bear Arm. *Sills:* R, Renzy; RN, Robe Noire. *Thrust faults:* GF, Grenville Front; ABT, Allochthon Boundary Thrust. Modified after Corriveau et al. (2007). Permission: <https://gac.ca/about/who-we-are/>

### 5.6.2 Comparison to the Lac Saint-Jean Anorthositic Suite

The Lac Saint-Jean (LSJ) Anorthositic Suite (Figure 5.5) is the largest (20000 km<sup>2</sup>) anorthosite massif in the world (see Ashwal 1993), and is dominated by 95 % anorthosite and leuconorite plus minor amounts of leucotroctolite, norite, olivine gabbro, gabbro, pyroxenite, peridotite, dunite, nelsonite, magnetite and charnockite-mangerite (Hébert et al. 2005). Labradorite (An<sub>50</sub>-An<sub>69</sub>) is the predominant type of plagioclase in the suite, but andesine-type plagioclase (An<sub>30</sub>-An<sub>49</sub>) is also present, especially in the northern and eastern parts (Hébert et al. 2005).

Hébert et al. (2005) studied 20 different Fe-Ti-V and Fe-Ti-P deposits in the northern portion of the LSJ Anorthositic Suite. One of their observations was that Fe-Ti-V deposits (comprising magnetite and ilmenite) occur only in rocks containing labradorite-type plagioclase, whereas Fe-Ti-P deposits (comprising magnetite, ilmenite, and apatite) are restricted to rocks containing andesine-type plagioclase. The data presented in this study paint a somewhat more complex picture in that the Étoile Suite is characterised by Fe-Ti-V mineralization that is predominantly associated with andesine-type plagioclase (An<sub>30</sub>-An<sub>49</sub>) (see Figure 4.25).

Hébert et al. (2005) observed that the composition of plagioclase within the 'south-central' Grenville Province becomes progressively more evolved with decreasing age: the ~1327 Ma De La Blache Mafic Plutonic Suite contains labradorite-type plagioclase, the 1160-1135 Ma Lac Saint-Jean suite contains both labradorite- and andesine-type plagioclase, and the 1016 Ma Mattawa, and 1010-1008 Ma Labrieville alkaline anorthosite suites contain predominantly andesine-type anorthosite. The age (1148.3 ± 9.6 Ma, Jean David, personal

communication), as well as the composition of plagioclase in the Étoile Suite (Figure 4.25) is consistent with their model.

The authors also observed a change in ore mineralogy with time, with the older suites (e.g., the 1327 Ma De La Blache Mafic Plutonic Suite and 1160-1135 Ma Lac Saint-Jean Anorthositic Suite) having a magnetite-ilmenite assemblage, and the younger suites (e.g., the 1080-1069 Ma Pipmuacan Suite and 1020-1008 Ma Valin Anorthositic Suite) having a hemoilmenite-magnetite-apatite assemblage. Again, the age and oxide assemblage (magnetite-ilmenite) of the Étoile Suite is consistent with their observations.

Hébert et al. (2005) proposed a couple of explanations for the temporal evolution in plagioclase compositions and ore mineral assemblages in the anorthosite massifs of south-central Quebec. They attributed decreasing anorthite in plagioclase to increasing differentiation of the parental magmas with time, and they attributed the changing ore mineral assemblages to increases in oxygen fugacity with time.

### **5.6.3 Comparison to the Kiglapait Intrusion**

Because there are certain lithological similarities between the Étoile Suite and the troctolite-gabbro intrusions of Kiglapait and Voisey's Bay in the Nain Plutonic Suite, Labrador (Figure 5.6), it is possible that their petrological evolution equally is comparable. This theme is explored in more detail in the following section.

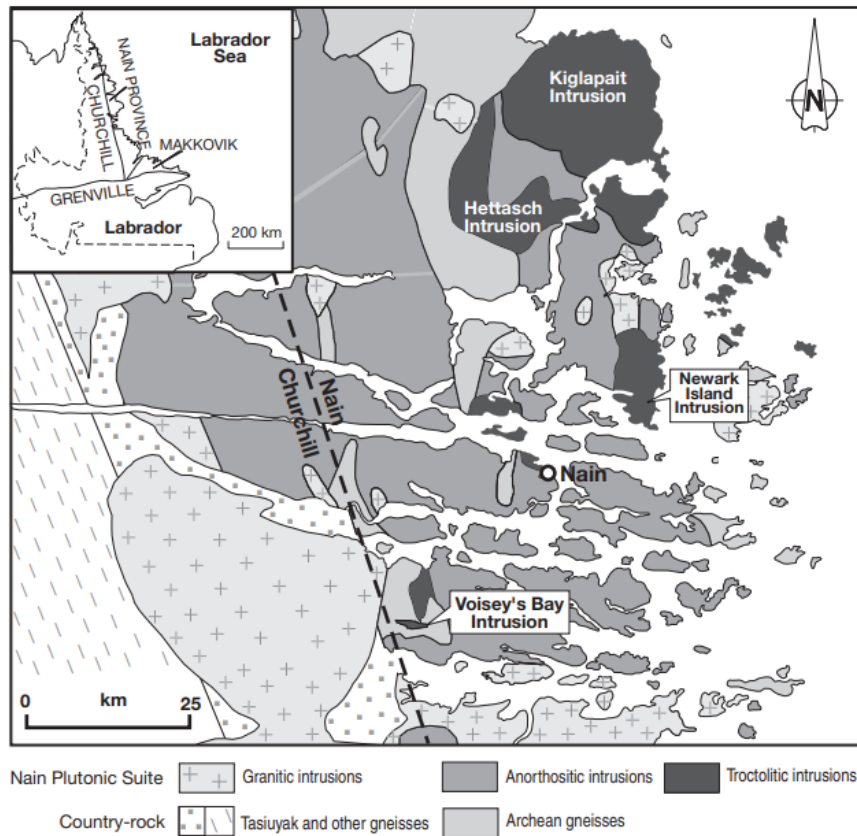


**Figure 5.6:** Regional geology of the area around the Kiglapait Intrusion and the Voisey's Bay deposit by Ripley and Li (2011) after Ryan et al. (1995). Permission: Copyright and Open Access | SEG (Society of Economic Geologists) (segweb.org)

Kiglapait is a bowl-shaped layered intrusion with an area of ~560 km<sup>2</sup> (Morse 2015) (Figure 5.7). The host rocks are Archean migmatites, supracrustal rocks of the Snyder Group, and anorthosites of the Nain Plutonic Suite (Ryan 1990; Morse et al. 2004; Scoates and Mitchell 2000). The Layered Series has a thickness of ~8.4 km (Morse 2015). It comprises a ~5 km-thick troctolitic Lower Zone and a ~4 km-thick olivine gabbroic Upper Zone containing an oxide-rich ore band with approximately 0.36 wt. % V<sub>2</sub>O<sub>5</sub> (Morse 2015; Kerr et al. 2013). Plagioclase and olivine are cumulus minerals throughout the Layered Series. They are joined by augite at 84 percent solidified (PCS), Fe-Ti oxide at 88.6 PCS, sulphide at 91 PCS, apatite at 94 PCS, and ternary feldspar (mesoperthite) at 99.65 PCS (Morse et al. 2004). The magnetite to ilmenite ratio in the ore bands is 82:18, and 50:50 in the silicate rocks (Morse 1980).

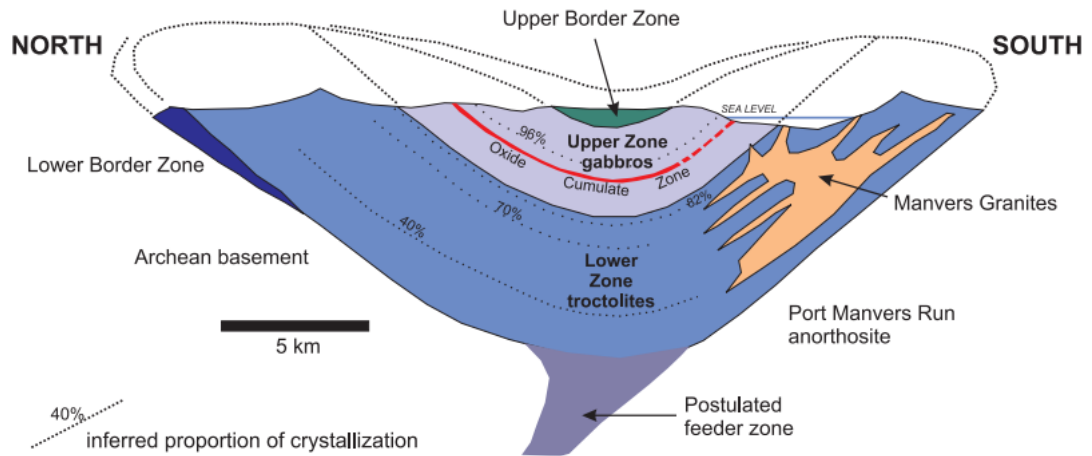


**Figure 5.7:** Schematic cross section of the Kiglapait intrusion modified by Kerr et al. 2013 after Morse (1969). Permission: <https://www.gov.nl.ca/disclaimer/>

The Lower Zone of the Kiglapait intrusion bears a strong similarity to Zone A of the Étoile Suite, as both are composed primarily of plagioclase-olivine cumulates (i.e., troctolite) with clinopyroxene and oxides as intercumulus phases (see Figure 4.4). Zone B of the Étoile Suite is broadly analogous to the Upper Zone of Kiglapait in that both consist largely of plagioclase-olivine-clinopyroxene cumulates (i.e., olivine gabbro) containing cumulus oxides (Figure 4.4). The Upper Zone of Kiglapait, however, does not contain plagioclase-clinopyroxene cumulates (i.e., gabbro), which are relatively abundant in the upper portion of Zone B of the Étoile Suite (Figure 4.4).

In order to compare the degree of fractionation in the two intrusions, the anorthite content of plagioclase is plotted against the forsterite content of olivine in Figure 5.8. The two intrusions show broadly similar fractionation trends, but the Étoile Suite lacks the highly evolved compositions (<30 mol % An, <15 mol % Fo) observed in the Upper Zone of Kiglapait, except in mafic pegmatite pockets containing apatite and zircon that were used to date the Étoile Suite. Similarly, the basal portion of Kiglapait is slightly more primitive than the basal portion of the Étoile Suite: An contents as high as ~66 mol % are found in the former, compared to 57 mol % in the latter. It is also worth comparing the relative timing of the saturation of the oxides in the two intrusions. Figure 5.8 shows that the first sample to contain cumulus magnetite in the Étoile

Suite plots at  $An_{\text{plagioclase}} = 48$ . This compares favourably to the An content of Kiglapait's Main Ore Band ( $An_{\text{plagioclase}} = 50$ ).

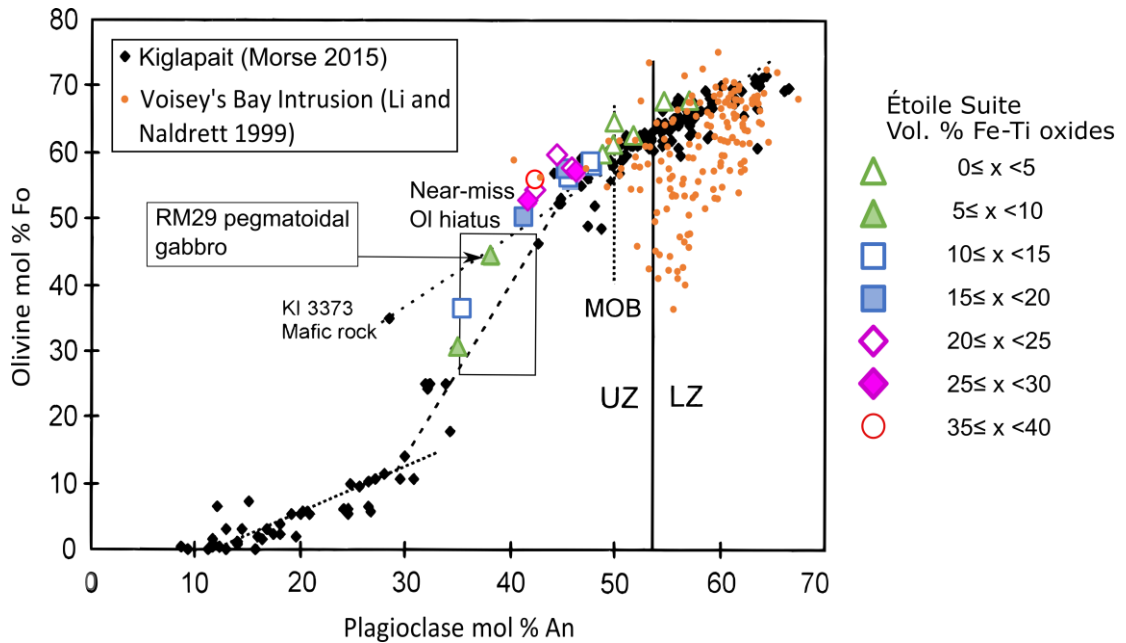


**Figure 5.8:** Anorthite (An) content of plagioclase versus forsterite (Fo) content of olivine at Kiglapait (black diamonds), Voisey's Bay (orange circles), and the Étoile Suite. MOB = Main Ore Body of Kiglapait. LZ = Lower Zone of Kiglapait; UZ = Upper Zone of Kiglapait. Source for Kiglapait data is Morse (2015); source for Voisey's Bay data is Li and Naldrett 1999. Modified after Morse (2015). Permission acquired from Springer.

#### 5.6.4 Comparison to the Voisey's Bay Intrusion

The Voisey's Bay intrusion is well-known for its world-class Ni-Cu sulphide deposit discovered in 1995 (Naldrett et al. 1996). A comparison with the Étoile Suite is potentially useful to assess the prospectivity of the latter with regard to Ni-Cu mineralization.

The Voisey's Bay Intrusion was emplaced in the ca. 1850 Ma, east-dipping collisional suture zone between the Archean Nain Province to the east and the Proterozoic Churchill Province to the west (Ryan et al. 1995). The Churchill Province consists largely of 'Tasiuyak gneiss' (interbanded garnet-sillimanite plus sulphide- and graphite-bearing quartzofeldspathic paragneiss) and minor amounts of massive or lineated enderbite gneiss, whereas the Nain Province consists of interbanded granitic, intermediate, and mafic orthogneiss (Li and Naldrett 1999).

The intrusion comprises two troctolitic magma chambers linked by a troctolitic-gabbroic feeder conduit (Li et al. 2007). The lower magma chamber is termed the Reid Brook Chamber, whereas the upper chamber is termed the Eastern Deeps Chamber. Anorthite in plagioclase ranges between 67.3 and 40.1 mol %, whereas forsterite in olivine ranges between 75.3 and 36.5 mol % (Figure 5.8). Voisey's Bay thus appears to be analogous to the more primitive Lower Zone of the Kiglapait Intrusion and Zone A of the Étoile Suite. The sulphide mineralization at Voisey's Bay is hosted in the feeder zone connecting the two chambers (exposed at e.g., the Discovery Hill Zone) as well as at the base of the Eastern Deeps Chamber (the 'Ovoid') (see Li and Naldrett 1999).

Li and Naldrett (1999) proposed that the magma in the lower chamber reached sulphide melt saturation due to contamination by assimilation of the sulphide-bearing Tasiuyak gneiss. As the magma continued its ascent through the feeder conduit into the upper chamber, the entrained sulphides precipitated in flow dynamic traps, such as the widened portions of the conduit and the exit of the conduit into the upper magma chamber (i.e., the Ovoid) (Li and Naldrett 1999).

The Ni content of olivine in the Voisey's Bay Intrusion has been used to indicate Ni-depletion as a result of sulphide saturation and/or interaction with sulphides (Li et al. 2007; Bulle and Layne 2015). The data of Li et al. (2007) show that olivines in the three sub-sections of the intrusion (i.e., the lower chamber, feeder and upper chamber) show a wide range of Fo and Ni contents (Figure 5.9). The least evolved olivines have ~80 % Fo and ~3000 ppm Ni, whereas the most evolved olivines have ~40 % Fo and ~250 ppm Ni. Two distinct fractionation trends can be distinguished: one population of olivines occurring in all three subsections follows a fractionation path consistent with a strongly Ni-depleted magma, whereas another population of olivines – mainly from troctolites of the upper (Eastern Deeps) chamber – is undepleted in Ni (Figure 5.9). The authors proposed that the depletion of Ni in some of the olivines resulted from the saturation and extraction of sulphides due to assimilation of the sulphide-bearing Tasiuyak gneiss country rocks.

More intriguing, however, is the fact that the Étoile Suite olivines also lie on the Ni-depleted fractionation curve (Figure 5.9). This could suggest that the mafic part of the Étoile Suite also crystallised from a magma that had equilibrated with sulphide melt. This is consistent with petrographic observations (i.e., increased sulphide contents in the lower portion of Zone B). However, olivines from the Étoile Suite are more evolved than those from Voisey's Bay (max Fo in Étoile Suite olivine = 67.7 mol % compared with 75.27 mol % in Voisey's Bay olivine). This suggests that any magmatic sulphides that may have formed would have lower Ni contents than those at Voisey's Bay. On the other hand, the sulphides would likely be more Cu rich, and possibly also contain elevated PGE.

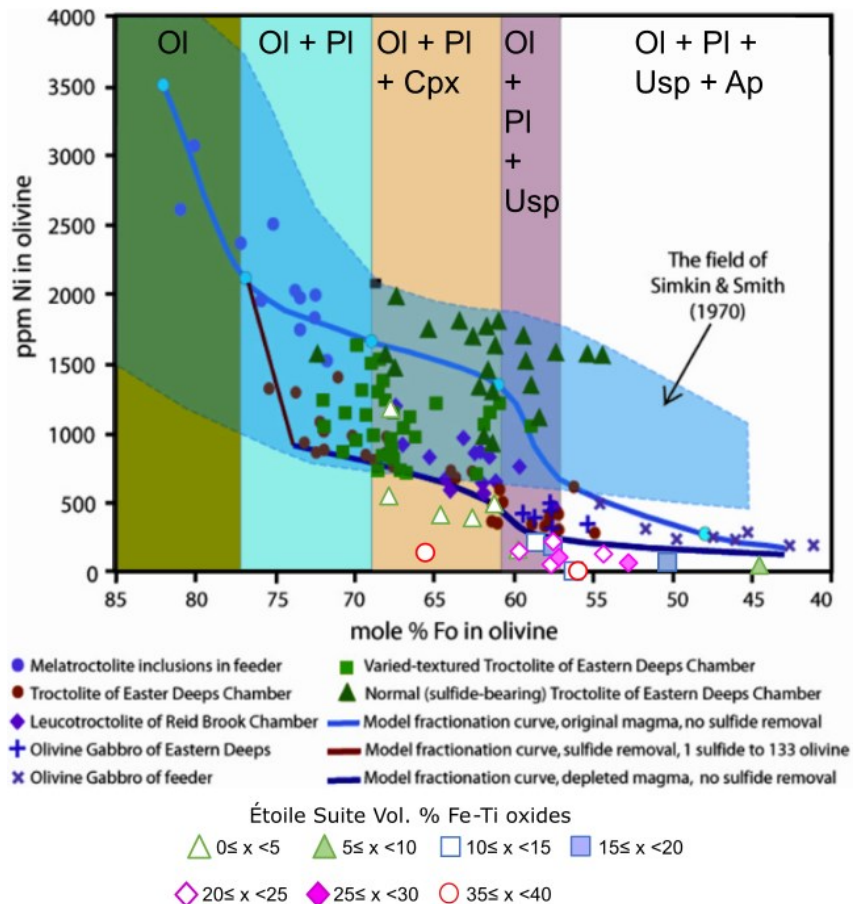


**Figure 5.9:** Nickel (Ni) in olivine versus forsterite (Fo) in olivine for troctolitic-gabbroic rocks from the Voisey's Bay Intrusion. The rocks are related to the initial introduction of magma (olivine gabbro of feeder, olivine gabbro of Eastern Deeps, leucotroctolite of Reid Brook, troctolite of Eastern Deeps, melatroctolite inclusions in feeder) and to later introductions of magma (varied-textured troctolite of Eastern Deeps, normal sulphide-bearing troctolite of Eastern Deeps). Data from the mafic part of the Étoile Suite are shown for comparison. Blue field is after Simkin and Smith (1970). Modified after Li et al. (2007).

## 5.7 Model for the formation of troctolitic intrusions in anorthosite-bearing terranes

Corrigan and Hanmer (1997) propose a model which reconciles the collisional tectonic setting of the Grenville Province with the formation of mantle-derived magmas that are parental to anorthosite. The model involves replacement of continental lithospheric mantle by asthenosphere, either via lithospheric delamination (Bird 1979) or convective thinning of the lithosphere (Houseman et al. 1981). Both processes may lead to crustal extension and to the production of mantle-derived melts (Platt and England 1993). In the Grenville Province, evidence for combined lithospheric delamination and extension manifests itself in the occurrence of sedimentary basins of broadly the same age as the 1180-1130 Ma magmatic pulse, as well as the many voluminous anorthosite complexes throughout the Grenville Province (Corrigan and Hanmer 1997).

The Lac Saint-Jean Anorthositic Suite is assumed to have formed according to the generalised model of Ashwal (1993). The model comprises the following steps: (1) ponding of mantle-derived basaltic magma in lower crustal magma chambers; (2) crystallisation of mafic silicates and plagioclase crystals; (3) accumulation of mafic silicates at the base, and plagioclase crystals at the top; and (4) ascent of the plagioclase-rich crystal mushes through the crust (along crustal shear zones such as the St.-Fulgence Deformation Zone) to their final sites of emplacement in the upper or middle crust (Figure 5.10A; Figure 2.3). However, in the case of troctolitic-gabbroic intrusions associated with AMCG suites, such as Kiglapait, Voisey's Bay and the Étoile Suite, the magma presumably did not pond at the lower crust and undergo fractionation of mafic silicates and plagioclase (Emslie et al. 1994; Kerr and Ryan 2000) (Figure 5.10B). Instead, it was transported more directly to its final site of emplacement along crustal shear zones.

Crucially, the Étoile Suite ( $1148.3 \pm 9.6$  Ma) slightly postdates the oldest rocks of the Lac Saint-Jean suite (1160 Ma), and the olivine-bearing, orthopyroxene-free (i.e., troctolitic) nature of the Étoile Suite possibly testifies to this: since the Lac Saint-Jean pluton probably reacted with continental crust during its ascent (Emslie et al. 1994; Kerr and Ryan 2000), later

throughgoing magmas would have been less likely to be contaminated due to the refractory nature of the previously-melted country rock. This could result in the formation of troctolitic suites rather than noritic ones when the later-throughgoing magmas cool. Fourny et al. (2019) came to a similar conclusion by showing that in the Nain Plutonic Suite (ca. 1360-1290 Ma; Myers et al. 2008), the first sequence of magmatism (beginning at ca. 1363; Myers et al. 2008) produced noritic intrusions and orthopyroxene-bearing anorthosite massifs, whereas the second phase of magmatism (beginning at ca. 1319 Ma; Myers et al. 2008) produced troctolitic intrusions and olivine-bearing anorthosite massifs.

As mentioned in Chapter 5.6.2, Hébert et al. (2005) observed that, in the Lac Saint-Jean anorthosite suite, Fe-Ti-(V) deposits (comprising magnetite and ilmenite) occur only in rocks containing labradorite-type ( $An_{50}$ - $An_{69}$ ) plagioclase. It was noted in Chapter 5.6.2 that the results from the Étoile Suite (this study) are somewhat inconsistent with the model of Hébert et al. (2005), seeing as plagioclase in the oxide-rich rocks of the Étoile Suite have comparatively lower An values of ~40-50. The model depicted in Figure 5.10 may, however, provide an explanation for the differing anorthite contents of plagioclase in the oxide-rich rocks of the Lac Saint-Jean Anorthosite Suite and the Étoile Suite. In essence, the higher degrees of crustal contamination of the Lac Saint-Jean massif predicted by the model would lead to an increase in the oxygen fugacity ( $fO_2$ ) of the magma (assuming the contaminant is oxidising), promoting early crystallisation of magnetite (i.e., when the magma is still crystallising labradorite-type plagioclase) along with orthopyroxene. Early crystallisation of magnetite in high- $fO_2$  conditions is well-modelled by the FMQ reaction:



The equation equally demonstrates why magnetite crystallises late under low- $fO_2$  conditions. This point was made by Morse (1980), who proposed that the later stages of crystallisation at Kiglapait follow the 'Fenner trend' which is characterised by relatively low- $fO_2$  conditions in which conversion of  $Fe_2SiO_4$  to  $Fe_3O_4$  is suppressed (Equation 3).

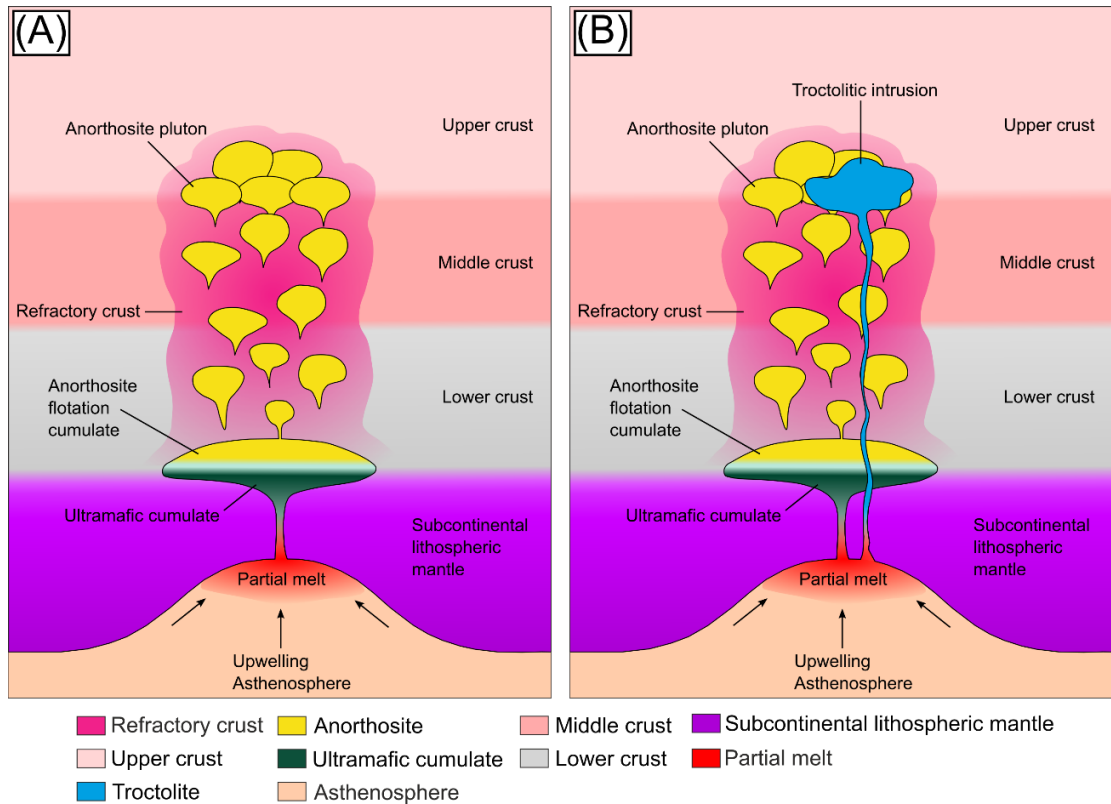


**Figure 5.10:** Model for the formation of troctolitic (i.e., olivine rather than orthopyroxene bearing) intrusions in anorthosite-bearing terranes such as the Grenville Province and Nain Plutonic Suite based on ideas presented in Ashwal (1993), Emslie et al. (1994), Kerr and Ryan (2000), and Fourny et al. (2019). **(A)** Model for petrogenesis of massif-type anorthosite after Ashwal (1993) and Emslie et al. (1994). Ponding and fractionation of mantle-derived melt at the lower crust. Mafic silicates sink to form ultramafic cumulates, while plagioclase crystals float to form flotation cumulates. The positively buoyant plagioclase flotation cumulates, along with residual liquid enriched in Fe, Ti, V, and P, subsequently rise through the crust to their final sites of emplacement. The ponded basaltic melt, as well as the anorthosite plutons, partially melt the country rock, making it less reactive as a result. **(B)** At a later date, magmas parental to troctolitic intrusions are transported to their final sites of emplacement without undergoing significant fractionation in lower crustal staging chambers (Emslie et al. 1994; Kerr and Ryan 2000; Fourny et al. 2019). The magmas pass through crust that has experienced prior melt extraction (due to interaction with earlier anorthositic mushes), and therefore assimilate relatively little crustal material (Emslie et al. 1994; Fourny et al. 2019). As a result, the magmas form troctolitic layered intrusions.

## Chapter 6

### Summary and conclusions

The present thesis represents the first petrographic and geochemical characterisation of the mafic part of the Étoile Suite. The data presented in the preceding chapters indicate that the Étoile Suite is a large (~4 km-thick) mafic-ultramafic layered intrusion in the Grenville Province, Canada.

The main rock-forming minerals are plagioclase, olivine, clinopyroxene, magnetite, and ilmenite. The mafic silicates tend to be associated with the Fe-Ti oxide-enriched portions of samples, resulting in modal layering defined by distinct plagioclase-rich domains and oxide-rich melanocratic domains. The origin of the layering remains poorly constrained, but it is probably related to gravitational sorting.

The minerals display cumulus or intercumulus habit in the stratigraphic succession, allowing the intrusion to be subdivided into three stratigraphic zones: two zones with intercumulus Fe-Ti oxides (Zone A and Zone C) and one zone with cumulus Fe-Ti oxides (Zone B). The stratigraphic distribution of the cumulus minerals can be used to provide an estimate of the crystallisation sequence in the mafic part of the Étoile Suite. The crystallisation sequence is interpreted to be: plagioclase + olivine → plagioclase + olivine + clinopyroxene (+ orthopyroxene where contamination occurred) → plagioclase + olivine + clinopyroxene + magnetite → plagioclase + olivine + clinopyroxene + magnetite + ilmenite → plagioclase + olivine + clinopyroxene + magnetite + ilmenite + sulphides.

The rock-forming minerals also show considerable stratigraphic variation in abundance with height, with magnetite and ilmenite being especially abundant in the lower portion of Zone B. Here, magnetite and ilmenite grains form semi-massive layers, constituting a potentially economic V deposit which is under current investigation by SOQUEM.

The V-mineralized oxide-rich layers in the lower portion of Zone B are proposed to have formed via the crystallisation and subsequent accumulation of magnetite and ilmenite

grains. The absence of apatite in the magnetite and ilmenite layers is inconsistent with crystallisation from immiscible Fe-rich silicate or oxide liquids.

The composition of the main rock forming silicates and oxides records cryptic variation with stratigraphy indicating fractional crystallisation from the base (in the south east) to the top (in the north west), with several magma replenishments causing compositional reversals. The oxides crystallized at approximately the same stage as at Kiglapait, i.e., at around  $An_{\text{plagioclase}} = 50$ .

The Étoile Suite crystallised under  $fO_2$  conditions corresponding roughly to 1.0 log units above the FMQ buffer. This value is close to the  $fO_2$  range in which the most V-rich magnetite typically crystallises (i.e., FMQ +0.25 to FMQ -0.25).

There is an enrichment in sulphides coinciding with the oxide-rich zone, reflected by a peak in Cu contents. Future work should determine whether there are any PGE enrichments associated with this horizon.

The olivines in the intrusion appear to be depleted in Ni relative to olivines with similar forsterite contents at Voisey's Bay, possibly suggesting that the Étoile Suite magma reached initial sulphide saturation prior to final emplacement.

The emplacement and crystallisation age of the Étoile Suite has been determined at  $1148.3 \pm 9.6$  to  $1147.3 \pm 4.4$  Ma, which is consistent with Lac Saint-Jean AMCG magmatism (1160-1135 Ma). This indicates that anorthosite massifs and layered intrusions can be consanguineous.

The similarity in the liquid line of descent of the Étoile Suite magma and those of other 'troctolitic' layered intrusions (particularly in the Nain Plutonic Suite) suggests that they were similar in composition. Isotopic work on troctolitic intrusions in the Nain Plutonic Suite indicate that they record minimal (<5 %) crustal contamination because their parental magmas passed through crust that had previously experienced melt extraction. The uncontaminated nature of troctolitic intrusions is considered important from the standpoint of Fe-Ti-(V) mineralization, because contamination typically increases the  $fO_2$  of the magma, and at relatively low  $fO_2$  (FMQ +0.25 to FMQ -0.25) the partition coefficient of V into magnetite is relatively high ( $D = \sim 30$ ).

## Chapter 7

### Recommendations for further work

Many questions remain unanswered and more detailed work on a range of geological aspects is clearly desirable, particularly once drill cores intersecting the intrusion become available. Some key questions are listed below.

#### 7.1 Characterisation of the country rocks in order to constrain the nature of potential contamination

Modelling the degree of crustal contamination would provide further insight on the petrogenesis of the mafic part of the Étoile Suite and its oxide ores. This requires a good understanding of the composition of the potential contaminants, i.e., the country rocks to the intrusion. As yet, few of these have been characterised. Key analytical methods to be employed include whole-rock analysis for lithophile and chalcophile elements as well as selected isotope systems (e.g., Nd, Hf). A further important component of future modelling work would be to isotopically characterise the Étoile Suite itself, by analysing selected samples from across the body. In view of the relatively unaltered nature of the rocks, *in situ* analysis of Sr isotopes in plagioclase would provide relatively fast and meaningful results. This would also enable comparison to other mafic magmatic units and bodies in the Grenville Province, many of which have been isotopically characterised in terms of Sr and Nd (Ashwal 1993).

#### 7.2 Determination of the PGE contents of the cumulates

The oxide layers in some layered intrusions have been found to be relatively PGE rich, notably Rincon del Tigre in Bolivia (Prendergast 2000), Koitelainen in Finland (Mutanen 1997), and Stella in South Africa (Maier et al. 2003). For example, at Stella, massive magnetite layers may contain up to 13 ppm PGE, making the deposit potentially economic. In addition, PGE

contents of intrusions can be used as proxies to delineate target horizons for potential reef-type deposits, particularly if compared to Cu contents. The principle is illustrated in Figure 7.1. PGE are far more compatible than Cu into any segregating sulphide melt (D values are  $\sim 10^5$  vs.  $10^3$ , respectively, see Barnes and Ripley 2016). Thus, Cu/Pd or Cu/Pt ratios should decrease sharply within a reef, but increase above the reef. If the reef is macroscopically invisible or not sampled due to limited outcrop, a significant change in Cu/Pd or Cu/Pt within the intrusion could pinpoint the most prospective horizon, thereby delineating a target for drilling.

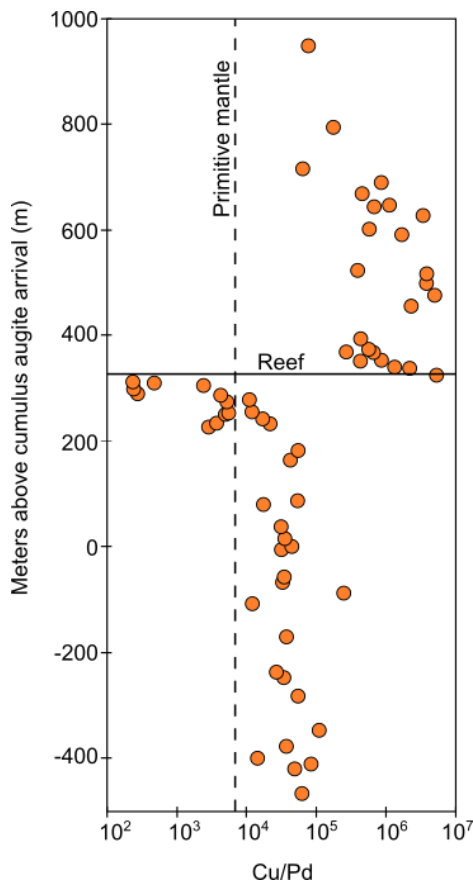


**Figure 7.1:** Variation of Cu/Pd at Sonju Lake (after Miller 1999). The reef is macroscopically invisible and relatively low grade, with up to 400 ppb PGE). Dashed line represents Cu/Pd ratio of primitive mantle.

## List of References

- Allmendinger, R.W., Cardozo, N. and Fisher, D.M., 2011. Structural geology algorithms: Vectors and tensors. Cambridge University Press.
- Amelin, Y., Li, C. and Naldrett, A.J., 1999. Geochronology of the Voisey's Bay intrusion, Labrador, Canada, by precise U–Pb dating of coexisting baddeleyite, zircon, and apatite. *Lithos*, **47**: 33-51.
- Andersen, D.J., Lindsley, D.H. 1985. New (and final!) models for the Ti-magnetite/ilmenite geothermometer and oxygen barometer. Abstract for the AGU 1985 spring meeting, *Eos Transactions, American Geophysical Union*, **66**: 416.
- Andersen, D.J., Lindsley, D.H. and Davidson, P.M., 1993. QUILF: A pascal program to assess equilibria among Fe-Mg-Mn-Ti oxides, pyroxenes, olivine, and quartz. *Computers & Geosciences*, **19**: 1333-1350.
- Arth, J.G., 1976. Behaviour of trace elements during magmatic processes. *US Geological Survey Journal of Research*, **4**: 41-47.
- Ashwal, L.D. (1993): Anorthosites. Springer-Verlag, Berlin, Germany.
- Ashwal, L.D. and Bybee, G.M., 2017. Crustal evolution and the temporality of anorthosites. *Earth-Science Reviews*, **173**: 307-330.
- Barnes, S.J. and Ripley, E.M., 2016. Highly siderophile and strongly chalcophile elements in magmatic ore deposits. *Reviews in Mineralogy and Geochemistry*, **81**: 725-774.
- Barnes, S.J., Maier, W.D. and Ashwal, L.D., 2004. Platinum-group element distribution in the main zone and upper zone of the Bushveld Complex, South Africa. *Chemical Geology*, **208**: 293-317.
- Barnes, S.J., Makovicky, E., Makovicky, M., Rose-Hansen, J. and Karup-Moller, S., 1997. Partition coefficients for Ni, Cu, Pd, Pt, Rh, and Ir between monosulfide solid solution and sulfide liquid and the formation of compositionally zoned Ni–Cu sulfide bodies by

- fractional crystallization of sulfide liquid. *Canadian Journal of Earth Sciences*, **34**: 366-374.
- Barnes, S.J., Mansur, E.T., Pagé, P., Meric, J. and Arguin, J.P., 2020. Major and trace element compositions of chromites from the Stillwater, Bushveld and Great Dyke intrusions compared with chromites from komatiites, boninites and large igneous provinces.
- Bird, P., 1979. Continental delamination and the Colorado Plateau. *Journal of Geophysical Research: Solid Earth*, **84**: 7561-7571.
- Bolsover, L.R., 1986. Petrogenesis of the Sybille iron-titanium oxide deposit. Laramie anorthosite complex, Laramie Mountains, Wyoming [M.Sc. thesis]: Stony Brook, State University of New York.
- Boudreau, A., 2019. Hydromagmatic processes and platinum-group element deposits in layered intrusions. Cambridge University Press.
- Bryan, S.E. and Ernst, R.E., 2008. Revised definition of large igneous provinces (LIPs). *Earth-Science Reviews*, **86**: 75-202.
- Buddington, A.F. and Lindsley, D.H., 1964. Iron-titanium oxide minerals and synthetic equivalents. *Journal of petrology*, **5**: 310-357.
- Bulle, F. and Layne, G.D., 2015. Trace element variations in olivine from the Eastern Deeps intrusion at Voisey's Bay, Labrador, as a monitor of assimilation and sulfide saturation processes. *Economic Geology*, **110**: 713-731.
- Buro, Y.A., 2011. Technical report NI 43-101 on the mineral resources of the La Blache property, Quebec, Canada.
- Cardozo, N. and Allmendinger, R.W., 2013. Spherical projections with OSXStereonet. *Computers & Geosciences*, **51**: 193-205.

- Carr, S.D., Easton, R.M., Jamieson, R.A. and Culshaw, N.G., 2000. Geologic transect across the Grenville orogen of Ontario and New York. *Canadian Journal of Earth Sciences*, **37**: 193-216.
- Charlier, B. and Grove, T.L., 2012. Experiments on liquid immiscibility along tholeiitic liquid lines of descent. *Contributions to Mineralogy and Petrology*, **164**: 27-44.
- Charlier, B., Namur, O., Bolle, O., Latypov, R. and Duchesne, J.C., 2015. Fe–Ti–V–P ore deposits associated with Proterozoic massif-type anorthosites and related rocks. *Earth-Science Reviews*, **141**: 56-81.
- Charlier, B., Namur, O., Duchesne, J.C., Wiszniewska, J., Parecki, A. and Auwera, J.V., 2009. Cumulate origin and polybaric crystallization of Fe-Ti oxide ores in the suwalki anorthosite, northeastern Poland. *Economic Geology*, **104**: 205-221.
- Corrigan, D. and Hanmer, S., 1997. Anorthosites and related granitoids in the Grenville orogen: A product of convective thinning of the lithosphere? *Geology*, **25**: 61-64.
- Corrigan, D., 1995. Mesoproterozoic evolution of the south-central Grenville orogen; structural, metamorphic, and geochronologic constraints from the Mauricie transect (Doctoral dissertation, Carleton University).
- Corriveau, L., Perreault, S., Davidson, A. and Goodfellow, W.D., 2007. Prospective metallogenic settings of the Grenville Province. *Mineral deposits of Canada: a synthesis of major deposit-types, district metallogeny, the evolution of geological provinces, and exploration methods*: Geological Association of Canada, Mineral Deposits Division, Special Publication, **5**: 819-847.
- Dare, S.A., 2019. Pathfinder mineral geochemistry for magmatic oxide and sulfide mineralization: insights from trace elements in Fe-oxides determined by laser ablation ICP-MS. In: 15th SGA Biennial Meeting. Glasgow: Society for Geology Applied to Mineral Deposits.

- Dare, S.A., Barnes, S.J. and Beaudoin, G., 2012. Variation in trace element content of magnetite crystallized from a fractionating sulfide liquid, Sudbury, Canada: Implications for provenance discrimination. *Geochimica et Cosmochimica Acta*, **88**: 27-50.
- Dare, S.A., Barnes, S.J., Beaudoin, G., Méric, J., Boutroy, E. and Potvin-Doucet, C., 2014. Trace elements in magnetite as petrogenetic indicators. *Mineralium Deposita*, **49**: 785-796.
- Duchesne, J.C., 1999. Fe-Ti deposits in Rogaland anorthosites (South Norway): geochemical characteristics and problems of interpretation. *Mineralium Deposita*, **34**: 182-198.
- Emslie, R.F., Hamilton, M.A. and Thériault, R.J., 1994. Petrogenesis of a mid-Proterozoic anorthosite-mangerite-charnockite-granite (AMCG) complex: Isotopic and chemical evidence from the Nain Plutonic Suite. *The Journal of Geology*, **102**: 539-558.
- Ernst, R.E., Liikane, D.A., Jowitt, S.M., Buchan, K.L. and Blanchard, J.A., 2019. A new plumbing system framework for mantle plume-related continental Large Igneous Provinces and their mafic-ultramafic intrusions. *Journal of Volcanology and Geothermal Research*, **384**: 75-84.
- Forien, M., Tremblay, J., Barnes, S.J., Burgisser, A. and Page, P., 2015. The role of viscous particle segregation in forming chromite layers from slumped crystal slurries: insights from analogue experiments. *Journal of Petrology*, **56**: 2425-2444.
- Fourny, A., Weis, D. and Scoates, J.S., 2019. Isotopic and trace element geochemistry of the Kiglapait intrusion, Labrador: Deciphering the mantle source, crustal contributions and processes preserved in mafic layered intrusions. *Journal of Petrology*, **60**: 553-590.
- Francis, D., Scowen, P., Panneton, G. and Doig, R., 2000. Contrasting Si-saturation in troctolite-anorthosite intrusions along the Manicouagan corridor of the Abitibi-Grenville transect. *Canadian Journal of Earth Sciences*, **37**: 271-289.

- Freestone, I.C., 1978. Liquid immiscibility in alkali-rich magmas. *Chemical Geology*, **23**: 115-123.
- Frost, B.R., Lindsley, D.H. and Andersen, D.J., 1988. Fe-Ti oxide-silicate equilibria; assemblages with fayalitic olivine. *American Mineralogist*, **73**: 727-740.
- Ganino, C., Arndt, N.T., Zhou, M.F., Gaillard, F. and Chauvel, C., 2008. Interaction of magma with sedimentary wall rock and magnetite ore genesis in the Panzhihua mafic intrusion, SW China. *Mineralium Deposita*, **43**: 677-694.
- Gower, C.F. and Krogh, T.E., 2002. A U–Pb geochronological review of the Proterozoic history of the eastern Grenville Province. *Canadian Journal of Earth Sciences*, **39**: 795-829.
- Grant, M., 2020. Formation of Magmatic Fe-Ti-V-P Deposits Within the Lac St. Jean Area Saguenay, Québec, Canada: Insights from Trace Element Composition of Fe-Oxides and Apatite (M.Sc thesis, Université d'Ottawa/University of Ottawa).
- Haggerty, S. 2018. Chapter 8. Opaque Mineral Oxides in Terrestrial Igneous Rocks. In: Rumble, D. ed. *Oxide Minerals*. Berlin, Boston: De Gruyter: 303-502
- Hamilton, M.A. and Shirey, S.B., 1992. Nd and Sr isotopic variations in anorthositic rocks of the Nain Plutonic Suite, Labrador. In *American Geophysical Union, Spring Annual General Meeting, Montréal (Transactions of the American Geophysical Union)*, **73**: 355.
- Hébert, C., Cadieux, A.M. and Breemen, O.V., 2005. Temporal evolution and nature of Ti-Fe-P mineralization in the anorthosite mangerite charnockite granite (AMCG) suites of the south-central Grenville Province, Saguenay Lac St. Jean area, Quebec, Canada. *Canadian Journal of Earth Sciences*, **42**: 1865-1880.
- Hébert, C., Van Breemen, O., Cadieux, A.M. and Gosselin, C., 2009. Région du réservoir Pimpuacan (SNRC 22E): synthèse géologique. *Ressources naturelles et faune Québec*.
- Hébert, C., van Breemen, O., Tollo, R.P., Corriveau, L., McLelland, J. and Bartholomew, M., 2004. Mesoproterozoic basement of the Lac St. Jean Anorthosite Suite and younger

- Grenvillian intrusions in the Saguenay region, Québec: structural relationships and U-Pb geochronology. MEMOIRS-GEOLOGICAL SOCIETY OF AMERICA: 65-80.
- Higgins, M.D. and Van Breemen, O., 1996. Three generations of AMCG magmatism, contact metamorphism and tectonism in the Saguenay–Lac St. Jean region, Grenville Province, Canada. *Precambrian Research*, **79**: 327-346.
- Houseman, G.A., McKenzie, D.P. and Molnar, P., 1981. Convective instability of a thickened boundary layer and its relevance for the thermal evolution of continental convergent belts. *Journal of Geophysical Research: Solid Earth*, **86**: 6115-6132.
- Iacono-Marziano, G., Ferraina, C., Gaillard, F., Di Carlo, I. and Arndt, N.T., 2017. Assimilation of sulfate and carbonaceous rocks: Experimental study, thermodynamic modeling and application to the Noril'sk-Talnakh region (Russia). *Ore Geology Reviews*, **90**: 399-413.
- Irvine, T.N., 1982. Terminology for layered intrusions. *Journal of Petrology*, **23**: 127-162.
- Kelley, K.D., Scott, C., Polyak, D.E. and Kimball, B.E., 2017. Vanadium (No. 1802-U). US Geological Survey.
- Kerr, A. and Ryan, B., 2000. Threading the eye of the needle: lessons from the search for another Voisey's Bay in Labrador, Canada. *Economic Geology*, **95**: 725-748.
- Kerr, A., Walsh, J.A., Sparkes, G.W. and Hinchey, J.G., 2013. Vanadium potential in Newfoundland and Labrador: a review and assessment. Newfoundland and Labrador Department of Natural Resources, Geological Survey, **13**: 137-165.
- Klemm, D.D., Henckel, J., Dehm, R.M. and Von Gruenewaldt, G., 1985. The geochemistry of titanomagnetite in magnetite layers and their host rocks of the eastern Bushveld Complex. *Economic Geology*, **80**: 1075-1088.
- Kushiro, I. and Yoder Jr, H.S., 1966. Anorthite—forsterite and anorthite—enstatite reactions and their bearing on the basalt—eclogite transformation. *Journal of Petrology*, **7**: 337-362.

- Li, C. and Naldrett, A.J., 1999. Geology and petrology of the Voisey's Bay intrusion: reaction of olivine with sulfide and silicate liquids. *Lithos*, **47**: 1-31.
- Li, C., Naldrett, A.J. and Ripley, E.M., 2007. Controls on the Fo and Ni contents of olivine in sulfide-bearing mafic/ultramafic intrusions: Principles, modeling, and examples from Voisey's Bay. *Earth Science Frontiers*, **14**: 177-183.
- Lin, L. and Sawyer, E.W., 2019. Microstructure and compositional changes across biotite-rich reaction selvages around mafic schollen in a semipelitic diatexite migmatite. *Journal of Metamorphic Geology*, **37**: 539-566.
- Lindsley, D.H. and Epler, N., 2017. Do Fe-Ti-oxide magmas exist? Probably not!. *American Mineralogist*, **102**: 2157-2169.
- Maier, W.D., Barnes, S.J. and Groves, D.I., 2013. The Bushveld Complex, South Africa: formation of platinum–palladium, chrome-and vanadium-rich layers via hydrodynamic sorting of a mobilized cumulate slurry in a large, relatively slowly cooling, subsiding magma chamber. *Mineralium Deposita*, **48**: 1-56.
- Maier, W.D., Barnes, S.J., Gartz, V. and Andrews, G., 2003. Pt-Pd reefs in magnetitites of the Stella layered intrusion, South Africa: A world of new exploration opportunities for platinum group elements. *Geology*, **31**: 885-888.
- Meurer, W.P., Klüber, S. and Boudreau, A.E., 1997. Discordant bodies from olivine-bearing zones III and IV of the Stillwater Complex, Montana—evidence for postcumulus fluid migration and reaction in layered intrusions. *Contributions to Mineralogy and Petrology*, **130**: 81-92.
- Miller, J.D., 1999. Geochemical evaluation of platinum group element (PGE) mineralization in the Sonju Lake intrusion, Finland, Minnesota. Minnesota Geological Survey, University of Minnesota.

- Morse, S.A., 1969. The Kiglapait layered intrusion, Labrador (Vol. 112). Geological Society of America.
- Morse, S.A., 1980. Kiglapait mineralogy II: Fe-Ti oxide minerals and the activities of oxygen and silica. *Journal of Petrology*, **21**: 685-719.
- Morse, S.A., 2015. Kiglapait intrusion, Labrador. In *Layered intrusions (589-648)*. Springer, Dordrecht.
- Morse, S.A., Brady, J.B. and Sporleder, B.A., 2004. Experimental petrology of the Kiglapait intrusion: Cotectic trace for the Lower Zone at 5 kbar in graphite. *Journal of Petrology*, **45**: 2225-2259.
- Moukhsil, A., Côté, G., 2018. Géologie de la région du lac Borgia, Province de Grenville, nord de La Tuque, régions de la Mauricie et du Saguenay – Lac-Saint-Jean, Québec, Canada. Ministère de l'Énergie et des Ressources naturelles, Québec.
- Mutanen, T., 1997. Geology and ore petrology of the Akanvaara and Koitelainen mafic layered intrusions and the Keivitsa-Satovaara layered complex, northern Finland (Vol. 395). Espoo, Finland: Geological Survey of Finland.
- Myers, J.S., Voordouw, R.J. and Tettelaar, T.A., 2008. Proterozoic anorthosite–granite Nain batholith: structure and intrusion processes in an active lithosphere-scale fault zone, northern Labrador. *Canadian Journal of Earth Sciences*, **45**: 909-934.
- Mysen, B.O., 1979. Nickel partitioning between olivine and silicate melt; Henry's law revisited. *American Mineralogist*, **64**: 1107-1114.
- Nadeau, L. and Brouillette, P., 1994. Carte structurale de la région de La Tuque (SNRC 31P), Province de Grenville, Québec. Commission Géologique du Canada, dossier public, 2938.

- Nadeau, L. and Brouillette, P., 1995. Carte structurale de la région de Shawinigan (SNRC 31I), Province de Grenville, Québec. Commission Géologique du Canada, dossier public, 3012.
- Nadeau, L. and van Breemen, O., 1994. Do the 1.45–1.39 Ga Montauban group and the La Bostonnais complex constitute a Grenvillian accreted terrane. In Geological Association of Canada, Programs with Abstracts (Vol. 19, p. 81A).
- Nadeau, L. and Van Breemen, O., 2001. U-Pb zircon age and regional setting of the Lapeyrère gabbro-norite, Portneuf-Mauricie region, south-central Grenville Province, Quebec. Natural Resources Canada, Geological Survey of Canada.
- Nadeau, L., van Breemen, O., Hébert, C., 1992. Géologie, âge et extension géographique du groupe de Montauban et du complexe de La Bostonnais. Ministère de l'Énergie et des Ressources, Québec, pages 35-39.
- Naldrett, A.J., Keats, H., Sparkes, K. and Moore, R., 1996. Geology of the Voisey's Bay Ni-Cu-Co deposit, Labrador, Canada. *Exploration and Mining Geology*, **2**: 169-179.
- Namur, O., Abily, B., Boudreau, A.E., Blanchette, F., Bush, J.W., Ceuleneer, G., Charlier, B., Donaldson, C.H., Duchesne, J.C., Higgins, M.D. and Morata, D., 2015. Igneous layering in basaltic magma chambers. In *Layered intrusions (75-152)*. Springer, Dordrecht.
- Namur, O., Charlier, B., Toplis, M.J., Higgins, M.D., Liégeois, J.P. and Vander Auwera, J., 2010. Crystallization sequence and magma chamber processes in the ferrobasaltic Sept Îles layered intrusion, Canada. *Journal of Petrology*, **51**: 1203-1236.
- Naslund, H.R., 1983. The effect of oxygen fugacity on liquid immiscibility in iron-bearing silicate melts. *American Journal of Science*, **283**: 1034-1059.
- Ouellet, R., 2018. Rapport des travaux 2017-2018 sur la propriété Lac Fabien 31 P/16 (SNRC).
- Pang, K.N., Li, C., Zhou, M.F. and Ripley, E.M., 2008. Abundant Fe–Ti oxide inclusions in olivine from the Panzihua and Hongge layered intrusions, SW China: evidence for early

- saturation of Fe–Ti oxides in ferrobaltic magma. *Contributions to Mineralogy and Petrology*, **156**: 307-321.
- Parks, H. L., Jenkins, M. C., & Zientek, M. L. (2017). Titanium-vanadium deposits hosted in mafic-ultramafic layered intrusions and massif anorthosite intrusions from around the world [Data set]. U.S. Geological Survey. <https://doi.org/10.5066/F7TD9VHP>.
- Paton, C., Hellstrom, J., Paul, B., Woodhead, J. and Hergt, J., 2011. Iolite: Freeware for the visualisation and processing of mass spectrometric data. *Journal of Analytical Atomic Spectrometry*, **26**: 2508-2518.
- Pearce, J.A., Ernst, R.E., Peate, D.W. and Rogers, C., 2021. LIP printing: Use of immobile element proxies to characterize Large Igneous Provinces in the geologic record. *Lithos*, **392**: 106068.
- Perreault, S., 1992. Géologie du Grand lac Bostonnais. Ministère des Ressources naturelles et de la Faune, 1 carte à l'échelle 1/50 000.
- Philpotts, A.R., 1967. Origin of certain iron-titanium oxide and apatite rocks. *Economic Geology*, **62**: 303-315.
- Platt, J. and England, P., 1994. Convective removal of lithosphere beneath mountain belts- Thermal and mechanical consequences. *American Journal of Science*, **294**.
- Prendergast, M.D., 2000. Layering and precious metals mineralization in the; Rincón del Tigre Complex, Eastern Bolivia. *Economic Geology*, **95**: 113-130.
- Ramdohr, P., 1953. Ulvöspinel and its significance in titaniferous iron ores. *Economic Geology*, **48**: 677-688.
- Ripley, E.M. and Li, C., 2011. A review of conduit-related Ni-Cu-(PGE) sulfide mineralization at the Voisey's Bay Deposit, Labrador, and the Eagle Deposit, northern Michigan. *Reviews in Economic Geology*, **17**: 181-197.

- Rivers, T., 1997. Lithotectonic elements of the Grenville Province: review and tectonic implications. *Precambrian research*, **86**: 117-154.
- Rivers, T., 2008. Assembly and preservation of lower, mid, and upper orogenic crust in the Grenville Province—Implications for the evolution of large hot long-duration orogens. *Precambrian Research*, **167**: 237-259.
- Rivers, T., Culshaw, N., Hynes, A., Indares, A., Jamieson, R., and Martignole, J., 2012. The Grenville Orogen – A post-LITHOPROBE perspective. Chapter 3, in Percival, J.A., Cook, F.A., and Clowes, R.M., eds., *Tectonic Styles in Canada: the LITHOPROBE Perspective: Geological Association of Canada Special Paper*. **49**: 97–236
- Roedder, E., 1978. Silicate liquid immiscibility in magmas and in the system  $K_2O-FeO-Al_2O_3-SiO_2$ : an example of serendipity. *Geochimica et Cosmochimica Acta*, **42**: 1597-1617.
- Rudnick, R.L., Gao, S., Holland, H.D. and Turekian, K.K., 2003. Composition of the continental crust. *The crust*, **3**: 1-64.
- Ryan, B., 1990. Preliminary geological map of the Nain Plutonic Suite and surrounding rocks (Nain-Nutak, NTS 14 SW): Geological Survey, Dept. Mines and Energy, St. John's, NF, Map: 90-44.
- Ryan, B., 2000. The Nain-Churchill boundary and the Nain Plutonic Suite: A regional perspective on the geologic setting of the Voisey's Bay Ni-Cu-Co deposit. *Economic Geology*, **95**: 703-724.
- Ryan, B., Wardle, R.J., Gower, C. and Nunn, G.G., 1995. Nickel–copper sulfide mineralization in Labrador: the Voisey's Bay discovery and its exploration implications, *Current Research, Newfoundland Department of Natural Resources*. Geol. Surv. Rep: 95-1.
- Sappin, A.A., Constantin, M. and Clark, T., 2011. Origin of magmatic sulfides in a Proterozoic island arc—an example from the Portneuf–Mauricie Domain, Grenville Province, Canada. *Mineralium Deposita*, **46**: 211-237.

- Sappin, A.A., Constantin, M., Clark, T. and van Breemen, O., 2009. Geochemistry, geochronology, and geodynamic setting of Ni–Cu±PGE mineral prospects hosted by mafic and ultramafic intrusions in the Portneuf–Mauricie Domain, Grenville Province, Quebec. *Canadian Journal of Earth Sciences*, **46**: 331-353.
- Scoates, J.S. and Mitchell, J.N., 2000. The evolution of troctolitic and high Al basaltic magmas in Proterozoic anorthosite plutonic suites and implications for the Voisey's Bay massive Ni-Cu sulfide deposit. *Economic Geology*, **95**: 677-701.
- Simkin, T. and Smith, J.V., 1970. Minor-element distribution in olivine. *The Journal of Geology*, **78**: 304-325.
- Streckeisen, A., 1976. To each plutonic rock its proper name. *Earth-science reviews*, **12**: 1-33.
- Sun, S.S. and McDonough, W.F., 1989. Chemical and isotopic systematics of oceanic basalts: implications for mantle composition and processes. Geological Society, London, Special Publications, **42**: 313-345.
- Taylor, S.R. and McLennan, S.M., 1985. The continental crust: its composition and evolution.
- Tohver, E., Teixeira, W., van der Pluijm, B., Geraldies, M.C., Bettencourt, J.S. and Rizzotto, G., 2006. Restored transect across the exhumed Grenville orogen of Laurentia and Amazonia, with implications for crustal architecture. *Geology*, **34**: 669-672.
- Toplis, M.J. and Carroll, M.R., 1995. An experimental study of the influence of oxygen fugacity on Fe-Ti oxide stability, phase relations, and mineral—melt equilibria in ferro-basaltic systems. *Journal of Petrology*, **36**: 1137-1170.
- Toplis, M.J. and Carroll, M.R., 1996. Differentiation of ferro-basaltic magmas under conditions open and closed to oxygen: implications for the Skaergaard intrusion and other natural systems. *Journal of Petrology*, **37**: 837-858.

- Toplis, M.J. and Corgne, A., 2002. An experimental study of element partitioning between magnetite, clinopyroxene and iron-bearing silicate liquids with particular emphasis on vanadium. *Contributions to Mineralogy and Petrology*, **144**: 22-37.
- Toplis, M.J., Libourel, G. and Carroll, M.R., 1994. The role of phosphorus in crystallisation processes of basalt: an experimental study. *Geochimica et Cosmochimica Acta*, **58**: 797-810.
- Tremblay, C., 2018. DESCRIPTION PÉTROGRAPHIQUE DE QUATRE LAMES MINCES POLIES (LB-06, PM-6, PM-4, 0817-09).
- Tucker, R.D. and Gower, C.F., 1990. Salient features of the Pinware terrane, Grenville Province, eastern Labrador. In *Geological Association of Canada–Mineralogical Association of Canada, Program with Abstracts (Vol. 15, p. A133)*.
- Valvasori, A.A., Hanchar, J.M., Piercey, S.J. and Fonkwe, M.L., 2020. The origin and evolution of V-rich, magnetite dominated Fe-Ti oxide mineralization; Northwest River Anorthosite, south-central Labrador, Canada. *Mineralium Deposita*, **55**: 555-575.
- Vukmanovic, Z., Holness, M.B., Monks, K. and Andersen, J.C., 2018. The Skaergaard trough layering: sedimentation in a convecting magma chamber. *Contributions to Mineralogy and Petrology*, **173**: 1-18.
- Wager, L.R. and Brown, G.M., 1968. *Layered igneous rocks*. WH Freeman.
- Wang, M., Veksler, I., Zhang, Z., Hou, T. and Keiding, J.K., 2017. The origin of nelsonite constrained by melting experiment and melt inclusions in apatite: The Damiao anorthosite complex, North China Craton. *Gondwana Research*, **42**: 163-176.
- Woodruff, L.G., Bedinger, G.M. and Piatak, N.M., 2017. Titanium (No. 1802-T). *US Geological Survey*.

Woussen, G., Dimroth, E., Corriveau, L. and Archer, P., 1981. Crystallization and emplacement of the Lac St-Jean anorthosite massif (Quebec, Canada). *Contributions to Mineralogy and Petrology*, **76**: 343-350.

Zhou, M.F., Robinson, P.T., Leshner, C.M., Keays, R.R., Zhang, C.J. and Malpas, J., 2005. Geochemistry, petrogenesis and metallogenesis of the Panzhihua gabbroic layered intrusion and associated Fe–Ti–V oxide deposits, Sichuan Province, SW China. *Journal of Petrology*, **46**: 2253-2280.

## Appendices

The Excel file “Maier\_Randolph\_2022\_Appendix\_1\_(A1).xlsx” contains sample list and modal proportions.

The Excel file “Maier\_Randolph\_2022\_Appendix\_2\_(A2).xlsx” contains results for whole-rock analyses and results for analyses of the following reference materials: KPT (qtz diorite), KPT-GSE, LK-NIP (diabase), MIX-KPT-610 (calibrant), OKUM (komatiite), BC-28 (massive magnetite), and NIST-SRM-27f (Iron Ore).

The Excel file “Maier\_Randolph\_2022\_Appendix\_3\_(A3).xlsx” contains the analytical parameters and results for electron microprobe analyses of plagioclase, olivine, clinopyroxene, orthopyroxene, amphibole, biotite, magnetite, ilmenite, hercynite, and apatite.

The Excel file “Maier\_Randolph\_2022\_Appendix\_4\_(A4).xlsx” contains results for LA-ICP-MS analyses of plagioclase, olivine, clinopyroxene, orthopyroxene, magnetite, ilmenite, hercynite, and apatite, as well as results for LA-ICP-MS analyses of the following reference materials: G-NIST616, Gprob6, GSE-1g, NIST610, NIST612, NIST614, BC-28, and GSD-1g.